TU

TECHNISCHE UNIVERSITÄT WIEN

DISSERTATION

# Magnetic Properties of Complex Metallic Alloys $Al_3Mn(Pd,Fe)$

ausgeführt zum Zwecke der Erlangung des akademischen Grades eines Doktors der technischen Wissenschaften unter der Leitung von

Univ. Prof. Dipl.-Ing. Dr. techn. Walter Steiner

(E138)

Institut für Festkörperphysik

eingereicht an der Technischen Universität Wien

Technisch-Naturwissenschaftliche Fakultät

von

KAMRAN ALI

Matr.-Nr 0627501

Brigittenauer Lände 224/6802 1200 Wien, Austria

CB 323 Lalazar Liaqat Road Wah Cantt, Pakistan

Wien August 2010

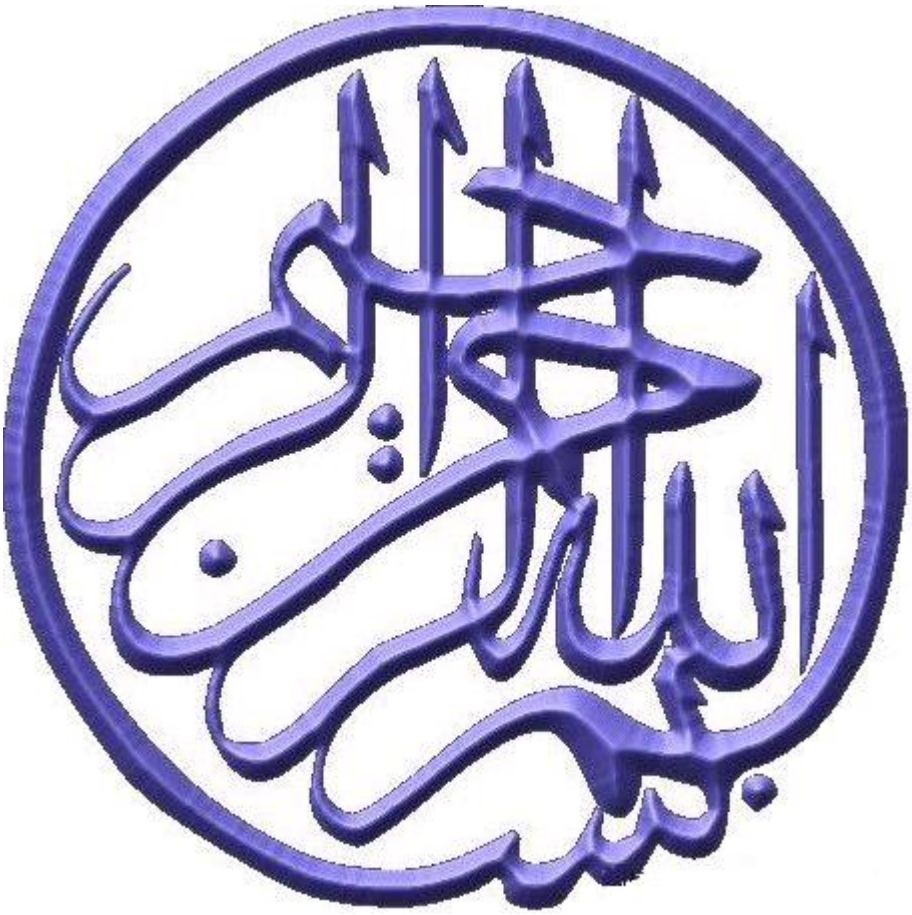

***DEDICATED TO MY PARENTS AND SUPERVISOR***

## ACKNOWLEDGMENTS

The whole praise to ALLAH the extreme powers, which blessed me with knowledge and enable me to accomplish this task. I offer my humblest and sincerest word of thanks to the Holy Prophet MUHAMMAD (Peace be upon him) who has ever blessed humanity with guidance.

I deem it my utmost pleasure to avail myself of this opportunity to express my heartiest gratitude and obligation to my reverend supervisor Walter Steiner of Institute of Solid State Physics, TU WIEN for his dexterous and illuminating guidance, sympathetic and encouraging attitude and erudite supervision that precariously enabled me to get this manuscript perfected. I am sure that will prove valuable source of inspiration through out my life.

Many thanks to Prof. Peter Mohn of the Institute of Applied Physics Vienna University of Technology and Prof. Michael Reissner of Institute of Solid State Physics for the evaluation of my thesis and for his guidance and help when ever needed and Prof. Bauer for the same.

Along with them I want to thank Univ. Prof. Dr. Bühler-Pastchen and all my teachers in Solid State Physics Institute and out side who helped and guide me during my stay in Vienna.

I feel great pleasure in expressing my deepest appreciation and sense of devotion for Dr Martin Müller, Peter Lielacher, Muhammad Atif, Tahir Ali, Rao Tahir, Nasir Mehboob and Saeed Badshah of the Institute of Solid State Physics and from Institute of Applied Synthetic Chemistry Naseem Iqbal Gunjial who helped me at each step during my stay in Vienna and in my research work. Perhaps with out there guidance, cooperation and useful suggestions, it would be too much difficult for me to complete this work in time.

I am obliged to the Higher Education Commission of Pakistan for the financial support during the entire study period in Austria and to the Austrian Exchange Services OÄD team for their sincere services all the way long. I am also thankful to my home department in Pakistan.

I will be missing my duties if I` d not thank my loving brothers Mr. Imran Ali, Mr. Salman Ali and my dearest sister, whose hands always raised in prayers for me.

The last of all no acknowledgement could ever adequately express my obligation to my parents. That success is really the fruit of their devoted prayers. May ALLAH the almighty bless my late mother with all the benefits of next life, and my father with good health and prosperous long life and be a source of prayers for me.

(Kamran ALI)

# Table of Contents

# List of Figures

# List of Tables

## Abstract

The search for new metallic materials with outstanding properties has turned in recent time to compounds with unit cells containing some tens to more than one thousand atoms. The Taylor phase T-$Al_3Mn$ is one example. The orthorhombic unit cell (space group *Pnma*) contains 156 atoms, and the structure persists if Mn is substituted by Pd or Fe. The structure is built up by ten layers perpendicular to the *b*-axis. Most of the atoms are located at vertices formed by pentagonal columnar clusters. Some of the 8d and 4c sites can be occupied by both Al and Mn. Thus inherent chemical and spatial disorder is present in the lattice and is further pronounced by substitution of Fe/Pd for Mn. This leads to random distribution of magnetic and nonmagnetic elements which is an important ingredient for the observed spin glass behaviour. T-$Al_3Mn$ is an approximant of the decagonal quasicrystal which is also formed in this concentration range of the Al-Mn system. The tiling approaches for the decagonal quasicrystal propose either elongated hexagons or a combination of pentagons and rhombi. Following the definition for approximants it can be assumed that the general building blocks in all samples are very similar.

By the present magnetic investigations (performed between 2 K and 300 K and in external fields up to 9 T) spin glass behaviour is obtained at low temperatures. Relative to the mother compound substitution of Pd (Fe) decreases (increases) the freezing temperature. Curie constant, Curie-Weiss temperature, and average magnetic moment per magnetic atom evaluated using Curie-Weiss law fit well into the dependence on Al content reported in literature. The influence of different crystal structure is not essential.

The time dependence of the magnetic moment points to broad activation energy distributions with similar shape but different centre of gravity for Fe and Pd containing alloys. For comparable temperatures the Fe containing compounds exhibit larger height of the barriers than those without and with Pd substitution. For the decagonal quasicrystal the mean effective activation energy is reduced compared to the one for the T-phase compounds.

The aim of the Mössbauer investigations was a comparison of the recorded spectra for the two structure types at different temperatures to proof, if for $^{57}Fe$ embeded in the building blocks resolvable hyperfine interactions are observable. Above freezing temperature at least two spectra are necessary for a reasonable analysis. Quadrupole splitting and center shift are, within measuring accuracy, the same for both structure types, strongly supporting that $^{57}Fe$ is embedded in similar surroundings. It seems that the occupation of the first neighbour shell with the available atom species is dominant and charge density and distribution on the $^{57}Fe$ probe atom are only slightly influenced by changes of the Fe content. The results support the similarities between decagonal compound and the approximant $Al_3Mn$.



The work was performed within the activities of the 6th Framework EU Network of Excellence "Complex Metallic Alloys" and the Pakistan Overseas Scholarship Program for PhD in Selected Fields.

## Kurzfassung

Materialien mit Einheitszellen, die mehrere zehn bis tausend Atome enthalten, erlangten in den letzten Jahren große Bedeutung. Die Taylorphase T-$Al_3Mn$ ist dafür ein Beispiel. Die orthorhombische Einheitszelle (Raumgruppe *Pnma*) enthält 156 Atome und die Struktur bleibt erhalten, wenn Mn durch Pd oder Fe substituiert wird. Die Struktur ist aus zehn Schichten, die senkrecht zur kristallographischen b-Achse liegen, aufgebaut. Der Großteil der Atome besetzt fünfeckige Prismen. Einige der 8d und 4c Plätze können sowohl von Al als auch Mn besetzt sein. Die chemische und räumliche Ordnung ist daher gestört und diese Störung wird durch die Substitution von Fe bzw. Pd verstärkt. Dies führt zu einer statistischen Verteilung von Atomen mit und ohne magnetischen Moment und liefert somit eine wesentliche Voraussetzung für die Ausbildung einer Spinglasordnung. T-$Al_3Mn$ ist ein Approximant für den dekagonalen Quasikristall, der ebenfalls in diesem Konzentrationsbereich des Al-Mn Systems gebildet wird. Die Strukturbeschreibung dieses Quasikristalls mittels tiling geht von verzerrten Sechsecken oder einer Kombination von Fünfecken und Rhomben aus. Entsprechend der Definition für einen Approximant sind die Blöcke aus denen diese Strukturen aufgebaut werden, in den Proben sehr ähnlich.

Bei tiefen Temperaturen zeigen die magnetischen Messungen (ausgeführt im Temperaturbereich zwischen 2 K und 300 K und in externen Feldern bis 9 T) Spinglasverhalten. Relativ zur Ausgangsverbindung fällt (steigt) die Gefriertemperatur mit der Substitution von Pd (Fe). Die aus den Analysen nach dem Curie-Weiss Gestz erhaltenen Curiekonstanten, Curie-Weiss Temperaturen und mittleren magnetischen Momente stimmen mit den in der Literatur angegeben Werten gut überein. Der Einfluss der unterschiedlichen Kristallstrukturen auf diese Größen ist klein.

Die Zeitabhängigkeit des magnetischen Momentes weist auf eine breite Verteilung der Aktivierungsenergie hin, wobei die Form der Verteilung für die Fe und Pd substituierten Proben gleich, der Schwerpunkt jedoch unterschiedlich ist. Die mittlere Aktivierungsenergie der dekagonalen Probe ist kleiner als jene der kristallinen Proben.

Ziel der Mößbaueruntersuchungen war es zu Überprüfen ob der Einbau von $^{57}Fe$ an verschiedenen Plätzen in den die Struktur aufbauenden Blöcken auf Grund der unterschiedlichen Hyperfeinwechselwirkung nachgewiesen werden kann. Oberhalb der Gefriertemparatur waren mindestens zwei Subspektren für die Analyse notwendig. Quadrupolaufspaltung und center-shift sind innerhalb der Messgenauigkeit für beide Strukturtypen gleich. Dies weist darauf hin, dass die lokalen Umgebungen für das $^{57}Fe$ Testatom sehr ähnlich sind. Es scheint, dass die Besetzung der ersten Nachbarschale mit der zur Verfügung stehenden Atomart für die Ladungsverteilung und -dichte bestimmend und die geänderte Fe-Konzentration von geringerer Bedeutung ist. Die Resultate Unterstützen die Ähnlichkeit von dekagonalem Quasikristall und Approximant T-$Al_3Mn$.

Die Arbeiten wurden im Rahmen des 6. Rahmenprogrammes EU-Network of Excellence "Complex Metallic Alloys" und des Pakistan Overseas Scholarship Program for PhD in Selected Fields durchgeführt.

# 1. Introduction

The search for new metallic materials with outstanding properties has turned in recent time to compounds with unit cells containing some tens to more than one thousand atoms. The main reasons for this are on the one side the progress on both the crystal growth techniques and the techniques for physical property measurements and on the other side the increase in computational power allowing theory to tackle problems posed by these complex systems. In an overview Urban and Feuerbacher [1] characterized these "giant unit cell crystals" starting from the crystallographic point of view by the appearance of typical cluster substructures, which defines by their length scales the physical properties. These length scales deviate substantially from the scale defined by the lattice parameters. A further characteristic is the inherent disorder caused by mixed or fractional site occupancy and the occurrence of atomic arrangements in different orientations inside the unit cell. Because of these particular structural features Urban and Feuerbacher proposed to call these metallic materials "structurally complex alloy phases" [1].

Another point of interest appeared with the discovery of an icosahedral (I) Al-Mn phase (Shechtman *et al.* 1984 [2]) and was caused by the structural similarity of the atomic arrangements inside the unit cell of these complex alloy phases with the short-range order structure of quasicrystals. These quasicrystals possess long range aperiodic order and crystallographically forbidden rational symmetries, and were thus fundamentally different from the two other known types of solid structure, crystalline and amorphous. They opened a new branch of crystallography and solid-state physics. The literature devoted to physical properties of quasicrystals has been growing rapidly. There was immediately great interest in determining whether similar phases would form in other alloy systems, too. A number of quasicrystals with icosahedral and decagonal structure, especially Al-based with wide variety of transition metal elements, have now been discovered [3, 4]. Progress in the knowledge of the structure of quasicrystals was made from comparisons of the known cluster structure of related crystalline metallics with the basic elements forming quasicrystals. In principle both crystalline and quasicrystalline structure types can be described with reference to an up to six - dimensional hypercubic lattice using a projection formalism. The difference is that a rational cut of the high - and the three - dimensional space is employed for the crystalline and an irrational one for the quasicrystalline lattice. For this reason in quasicrystal literature the giant unit cell metallics are frequently referred to as rational approximants [5].

To concentrate on particular subsets of the huge group of largely unknown multinary alloys which exhibit a crystal structure along the above given definition the European Network of Excellence *Complex Metallic Alloys* (*CMA*) [6] was founded. All samples investigated in this thesis were prepared and characterized within this network [7]. The focus lay on the less investigated Al-rich side of the Al-Mn alloy system with the extension to the ternary Al-Mn-Fe and Al-Mn-Pd systems, which contain several attractive complex metallic alloy (*CMA*) phases. The samples were produced from constituent elements by levitation induction melting in a water-cooled copper crucible under an argon atmosphere. Parts of the samples were annealed in argon at 900 and

930°C for up to one month and subsequently quenched into water. Metallurgical investigations were performed by scanning electron microscopy. Phase compositions were determined by energy dispersive X-ray analysis EDX and, inductively coupled plasma optical emission spectroscopy. The latter analyses were used for the determination of the oxygen and carbon contents in the samples and for the calibration of the EDX measurements. In addition, the samples were studied by selected-area electron diffraction in transmission electron microscopes and powder X-ray diffraction in transmission mode.

As pointed out the focus of this thesis lay on the Al-rich side of the Al-Mn alloy system with extension to the ternary Al-Mn-Pd and Al-Mn-Fe systems. One of the *CMA* - phases formed in this concentration region is the orthorhombic Taylor - phase T-$Al_3Mn$ (space group *Pnma*). This structure was first studied by Taylor in 1961 [8]. It is built up of ten atomic layers stacked perpendicular to the [010]-direction. By these layers pentagonal columnar clusters are formed along the axis which can be seen as the essential building blocks of these compounds. The unit cell contains 156 atoms with some sites having mixed Al/Mn occupation, so that inherent chemical disorder exists in the lattice [9, 10-12]. The Taylor - phase is known to possess highly interesting magnetic [13-16], electronic [17], and mechanical [18] properties, making it a promising starting material for technological applications like coating. The investigations are further extended in the Al-Mn-Fe system, to the region in which the quasicrystalline decagonal phase is formed as a solid solution.

Following the results of *ab initio* calculations, which were based on a tight-binding linear-muffin-tin-orbital technique using the local-spin-density approximation and were performed for decagonal AlMn compounds [13, 19], hybridization of Al-*p* and Mn-*d* states causes the appearance of a pseudo gap at the Fermi energy, and the fulfillment of local Stoner criteria governs the formation of Mn - moments. Hybridization is reduced by the confinement of the atoms to fixed interatomic spacings and favors an impurity like Mn local density of states. The presence of spatial randomly distributed moments together with the tendency towards antiferromagnetic coupling are prerequisite for the appearance of spin glass behavior.

In a spin glass material, as the system is cooled down from high temperature, spin directions freeze starting from some temperature, as if a phase transition has occurred. At the same time, spin directions remain largely uncorrelated as in the paramagnetic phase [20].

Some samples with T-$Al_3Mn$ and decagonal structure prepared in the above described manner are recently investigated by another group of the *CMA* network [16]. The results show at low temperatures spin glass behavior with its strange time dependence, some scatter of the freezing temperatures in concentration dependence of the constituent elements, and tendency towards antiferromagnetic coupling. Thus by the extension to new samples with somewhat different Al concentration and by magnetic measurements, which include the determination of the time dependence of the magnetization together with the extremely local character of $^{57}Fe$ Mössbauer investigations it should be possible to gain information about moment formation and to obtain knowledge about the difference of near neighbour environments in both crystalline and decagonal compounds.

Spin glass behavior was again observed at low temperatures for all samples irrespective of Pd/Fe content. It could be shown, that the two environments of the $^{57}$Fe probe atom, which are present in the Taylor phase if random substitution is assumed of Fe for Mn only - Fe completely surrounded by Al and Fe surrounded by both Al and Mn in the nearest neighbourhood - are the dominant elements for the magnetic and hyperfine interactions. It seems that in both the crystalline and the quasicrystalline compounds the occupation of the first neighbour shell with the available atom species defines charge density and charge distribution on the $^{57}$Fe probe atom, whereas changes of the Fe content, in the restricted concentration interval in which single phased samples are producible, have only slight influence. For the crystalline compounds the mean hyperfine field and mean effective transition metal moment increase with increasing Fe content. The results support strongly that similar interatomic configurations are present in the decagonal compound and in T-$Al_3Mn$ and that the exchange interaction on the length scales of these configurations dominate the electronic exchange interactions.

## 1.1 References


[1] K. Urban and M. Feuerbacher *J. of Non-Crystalline Solids* **334-335** (2004) 143–150.

[2] D. Shechtman, I. Blech, D. Gratias and J.W. Cahn *Phys. Rev. Lett.* **53** (1984), 1951-1953.

[3] Z.M. Stadnik 1999 *Physical Properties of Quasicrystals* (Springer, Berlin, Germany).

[4] H-R. Trebin 2003 *Quasicrystals Structure and Physical Properties* (Wiley, Morlenbach, Germany).

[5] C. Janot 1994 *Quasicrystals* (2nd Ed., Clarendon, Oxford).

[6] http://www.temas.ch/CMA/CMAProj.nsf/B74ECB2607C46FA4C12571FE0042BA5A/$FILE/Overview_JMD_CMA.pdf?OpenElement&enetarea=50 May (2010).

[7] M. Fuerbacher private communication.

[8] M.A. Taylor *Acta Cryst.***14** (1961), 84 (1pp).

[9] V. Simonet, F. Hippert, M. Audier and G. Trambly de Laissardière *Phys. Rev. B* **58** (1998), R8865-R8868.

[10] H. Klein, M. Boudard, M. Audier, M. De Boissieu, H. Vincent, L. Beraha and M. Duneau *Phil. Mag. Lett.* **75** (1997), 197-208.

[11] V.V. Pavlyuk, T.I. Yanson and O.I. Bodak *Acta Cryst. C* **51** (1995), 792-794.

[12] K. Hiraga, M. Kaneko, Y. Matsuo and S. Hashimoto *Phil. Mag. B,* **67** (1993), 193-205.

[13] J. Hafner and M. Krajči, *Phys Rev B* **57** (1998), 2849-2860.

[14] F. Hippert, V. Simonet, G. Trambly de Laissardière, M. Audier and Y. Calvayrac, *J. Phys, B Cond. Matter* **11** (1999), 10419-10435.

[15] V. Simonet, F. Hippert, M. Audier and Y. Calvayrac *Mater. Sci. Eng.* **294–296** (2000), 625-628.

[16] J. Dolinsek, J. Slanovec, Z. Jaglicic, M. Heggen, S. Balanetskyy, M. Feuerbacher and K. Urban *Phys. Rev. B* **77** (2008), 064430 (18pp).

[17] P. Volkov and S.J. Poon, *Phys. Rev. B* **52** (1995), 12685-12689.

[18] M. Feuerbacher and M. Heggen *Philos. Mag.* **86** (2006), 985-990.

[19] M. Krajci, J. Hafner and M. Mihalkovic *Phys. Rev. B* **55** (1997), 843 (13pp).

[20] J.A. Mydosh 1993 *Spin Glasses: an experimental introduction* (Taylor & Francis London. Washington, DC).

# 2. Structural Considerations

## 2.1 Crystal structure

The crystal structure of a material, which describes the arrangement of atoms in space, can be defined in terms of symmetry considerations together with a unit cell. This unit cell is given by the lattice parameters, the length of the cell edges and the angles between them. The positions of the atoms inside the unit cell are determined by the set of atomic parameters ($x_i$, $y_i$, $z_i$) which were measured from an origin (not inevitably be occupied by an atom) and follow certain symmetry conditions. A perfect crystal is considered to be constructed by a space lattice, i.e. by infinite regular repetition in space of identical structure units. There are 230 basically different repetitive patterns [1, 2].

## 2.2 Quasicrystals

Quasicrystals are structural forms that are both ordered and nonperiodic. Their symmetries can be considered to be between those of crystals and liquids [2, 3]. They can be described by certain atomic arrangements that fill all the space but lack translational symmetry in three dimensions. Classical theory of crystals allows only 2, 3, 4, and 6-fold rotational symmetries, but quasicrystals display symmetry of order (fold) 8, 10, and 12. Just like crystals, they produce sharp (X-ray, electron) diffraction patterns with defined structure [2].

The first of what later came to be known as quasicrystals was reported by Shechtman *et al.* in 1984 [4]. They showed electron diffraction patterns of an Al-Mn alloy with sharp reflections and 10-fold symmetry. The whole set of diffraction patterns revealed an icosahedral structure. Since then many stable and meta-stable quasicrystals were found. These are often binary or ternary metallic alloys with aluminum as one of the constituents. Summaries of recent investigations are e.g. given in [5, 6].

### 2.2.1 Types of Quasicrystals

Regarding thermal stability, three types of quasicrystals are distinguished [7]:

- stable quasicrystals grown by slow cooling or casting with subsequent annealing,
- metastable quasicrystals prepared by melt-spinning, and
- metastable quasicrystals formed by the crystallization from the amorphous phase.

In two dimensions, present if one direction is periodic and perpendicular to quasiperiodic layers, polygonal quasicrytals of the following types are distinguished [2]:

- octagonal quasicrystals with local 8-fold symmetry [primitive & body-centered lattices],
- decagonal quasicrystals with local 10-fold symmetry [primitive lattice], e.g. figure 2.1,
- dodecagonal quasicrystals with local 12-fold symmetry [primitive lattice]

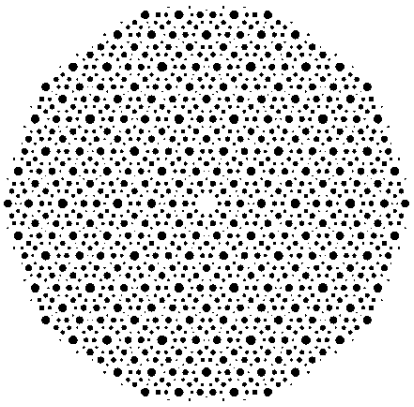

**Figure 2.1: Diffraction pattern of a decagonal quasicrystal with 10-fold symmetry. Taken from [2].**

In three dimensions, with no periodicity in any of these directions, the following types are observed [2]:

- icosahedral quasicrystals (axes:12x5-fold, 20x3-fold, 30x2-fold) [primitive, body-centered & face-centered lattices], and
- icosahedral quasicrystal with broken symmetry.

### 2.2.2 Tiling

Characteristic for quasicrystals are their diffraction patterns consisting of sharp diffraction spots/peaks which cannot be indexed by three Miller indices and reciprocal vectors. Mathematicians like Wang [8] described covering of planes using tiles in early 1960s. This idea was followed by the British mathematician Penrose, who suggested a way to cover a plane in a nonperiodic fashion using different types of tiles. The arrangement of these tiles (e.g. rhombi in figure 2.2) follows certain matching rules as in the present case that in every vertex all angles are either $2\pi/5$ and $4\pi/5$ or $\pi/5$ and $3\pi/5$ (see e.g. [9]). As important property self similarity is obtained, which means that the order of the tails is reproduced within a certain periodicity. Figure 2.2 (left) shows an example for this tiling. An equivalent tiling can be found for a three dimensional (3D) -arrangement. This is called 3D-Penrose tiling/pattern, and is made up of rhombohedra instead of the rhombi [2]. The resemblance noted between the icosahedral quasicrystal and the 3D-Penrose pattern produced a paradigm shift in some fields of crystallography and solid state physics approximately ten years later [2]. The main relevance for structural considerations is the possibility to put atoms (they should be rather seen as atom clusters) at the vertices of a derived tiling pattern and to perform the Fourier Transform, to end up with a "calculated" diffraction pattern. Comparison with the measured one indicates the successfulness of the tiling approach and allows conclusions on the structure [10].

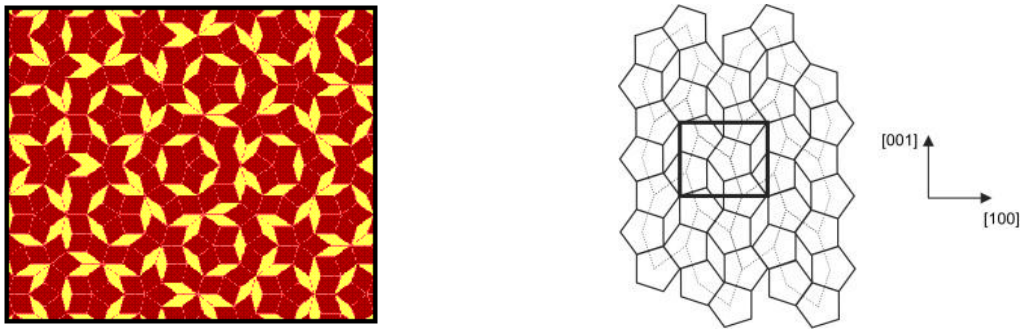


**Figure 2.2: Left: Penrose tiling performed with rhombi, taken from [2]. Right: Tiling description of (010) planes of the T-phase, different lines depict alternative tiling, taken from [11].**

### 2.2.3 Concept of higher dimensional space

The three integer Miller indices label the observable reflections of an ordinary crystal with translational symmetry. Ordering is called non-periodic if it lacks translational symmetry, what means that a shifted copy will never match exactly with its original. The more precise mathematical definition is that there is never translational symmetry in more than $n - 1$ linearly independent directions, where n is the dimension of the space filled. To assign integer indices to the diffraction spots/peaks of a polygonal (icosahedral) quasicrystal 5 (6) indices (called generalized Miller indices) are necessary. [12, 13]. The respective reciprocal vectors span a 5 (6) dimensional reciprocal space, which must have his equivalent in an n-D real space (n = 5, 6). In this space the structure is built up with its full periodicity. The location of the diffraction spots/peaks observed for the quasicrystal structure results as a section of this n-dimensional supercrystal with the 3-D physical space. The intensity is obtained from the respective Fourier Transform of the electron density of the supercrystal. A detailed description of this method is e.g. given by [12, 13].

The space groups for polygonal and icosahedral quasicrystals are calculated (see e.g.[12]). There are 90 for octagonal, 34 for decagonal, 33 for dodecagonal, and 11 for icosahedral quasicrystals.

## 2.3 Decagonal quasicrystals and approximants in the Al-Mn(Pd) system

In addition to the decagonal quasicrystal and the orthorhombic Taylor-phase T-$Al_3Mn$ a large number of other thermodynamically stable phases are formed on the Al-rich side of the Al-Mn(Fe/Pd) alloy system as discussed by [14]. The T-$Al_3Mn$ phase is considered to be an approximant of the decagonal (D) Al-Mn phase The structure is built up of atomic layers stacked perpendicular to the [010]-direction. By these layers pentagonal columnar clusters are formed along the axis which can be seen as the essential building blocks [15]. The unit cell contains 156 atoms with some sites having mixed Al/Mn(Fe/Pd) occupation, so that inherent chemical disorder exists in the lattice [11, 15-17], as will be discussed in detail in the following chapter.

### 2.3.1 Taylor Phase T- $Al_3Mn$

One of the first who studied the structure of the high temperature phase T-$Al_3Mn$ was Taylor in 1961 [18]. He proposed an orthorhombic unit cell with dimensions a = 1.488 nm, b = 1.242 nm and c = 1.259 nm and the space group Pnma. Hiraga *et al.* (1993) [17]

found the same space group (number 62) and dimensions a = 1.483 nm, b = 1.243 nm and c = 1.251 nm. Shi *et al.* (1994) [19] pointed out that the space group $Pn2_1a$ was a better description for a sample of nominal composition $Al_{3.54}Mn$. They obtained dimensions a = 1.4837 nm, b = 1.2457 nm, and c = 1.2505 nm. The structure consists of layers perpendicular to the b direction. One almost flat layer is embedded between two puckered ones. Altogether there are six layers in one unit cell. From an ingot of nominal composition $Li_{10}Mn_{40}Al_{50}$ single crystals with $Al_{3.31}Mn$ are extracted by Pavlyuk *et al.* (1995) [16]. The space group was again Pnma, the lattice parameters a = 1.4883 nm, b = 1.2447 nm, c = 1.256 nm. Klein *et al.* (1997) [15] reported on investigations on a single crystal with composition $Al_{72.3}Mn_{24.5}Pd_{3,2}$ having the same space group as T-$Al_3Mn$ and dimensions a = 1.4717 nm, b = 1.251 nm and c = 1.2594 nm, but as discussed below, different Al/Mn order on the respective lattice sites. A transition to another ternary orthorhombic phase was proposed. Reinvestigation of the ternary Al-Mn-Pd system by Balanetskyy *et al.* (2008) [11] confirm, however, the results of Gödeke and Lück (1995) [20] regarding the extension of the homogeneity range and the non-existence of this new ternary T-phase. For the lattice spacings of $Al_{76}Mn_{24}$ Balanetskyy *et al.* (2008) found a = 1.479 nm, b = 1.242 nm and c = 1.259 nm.
Diffraction patterns of the $Al_3Mn$ phase are shown in figure 2.3, together with those of the Al-Pd-Mn decagonal quasicrystal. In the pattern the strong spots distribution of $Al_3Mn$ phase is similar to that of decagonal quasicrystal, as indicated by arrowheads.

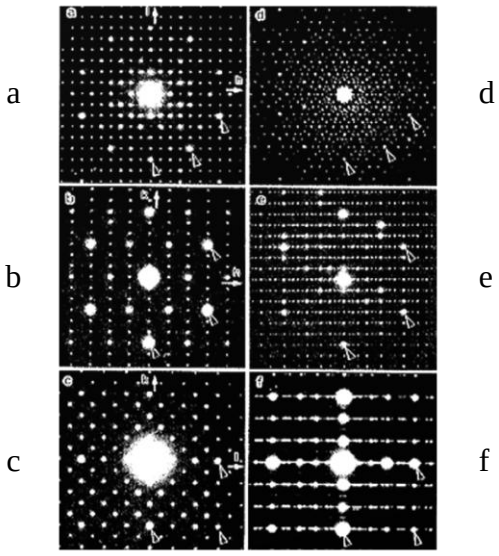


**Figure 2.3: Electron diffraction pattern of crystalline $Al_3Mn$ (a-c) and of decagonal Al-Pd-Mn phases (d-f). The distribution of strong spots is indicated by arrowheads. Taken from Hiraga *et al.* 1998 [17].**

Hiraga *et al*. (1993) [17], Pavlyuk *et al*. (1995) [16], and Klein *et al*. (1997) [15] determined atomic positions for T-$Al_3Mn$. They are reproduced in table 2.1 in such a way, that equivalent positions which are named in different way by the groups are arranged together. All authors reported that most of the sites are occupied only by either aluminum or manganese but some of the sites show mixed occupancy.

According to Hiraga *et al.*[17] Mn(5), Mn(6), Mn(8), and Mn(9) show mixed occupancy with some aluminum and Al(6) show that with some manganese. With the exception of the last mentioned Al(6) site this is also found by Pavlyuk *et al.* only the sites are named different. TM(1-5)(Mn/Al) of Klein *et al*. stands for Mn(8), Mn(9) and Al(6-8) of Hiraga *et al*. and Mn(3), Mn(1), Al(1), Al(8), and Al(4) of Pavlyuk *et al*, respectively. The Al/Mn occupations of these sites are quite similar. Klein *et al*. proposed that (site names after Hiraga *et al*.) Mn(1) to Mn(4) are half filled by Mn and Mn(5), Mn(6) are half filled by Al and called the last two sites Al(13) and Al(14), respectively. These sites are fully occupied by Hiraga *et al* and Pavlyuk *et al*. Al(16) of Hiraga *et al*. corresponds to Al(10) of Pavlyuk *et al* and TM(6) of Klein *et al*., who assumed that all of the Pd is embedded at this site if the structural model of T-$Al_3Mn$ is applied (table 2.1). In examining the intensity of the (020) reflex in X-ray diffraction patterns Balanetskyy *et al.* (2008) [11] concluded that this assumption is too crude for a correct description of the structure.

All groups report very similar values for the positions of the respective sites. Concerning the Mn/Al occupation Hiraga *et al*. (table 2.1, red) found in total 4(4)+2.8+3.2+8+4+4.8 +0.8/1.2+0.8+4+3.2+4(5)+7.2+8(10) = 39.6/116.4. This leads to $Al_{2.94}Mn$, very close to $Al_3Mn$. Taking the Pd content as Mn, Klein *et al*. (table 2.1, blue) ends up with the total Mn/Al occupation 2(4)+8+4+4+2.4+2.4+1.2+5/2(2)+4+4+ 2(5)+5.6+5.6+6.8+7(8)+3 = 35/99. From this atom count follows $Al_{2.83}Mn$. The Al content is smaller than the one of the stoichiometric composition $Al_3Mn$, however not all of the 156 sites are fully occupied. Pavlyuk *et al*. (table 2.1, green) end up with the total Mn/Al occupation 4(4)+2.12+2.56+8+3.2+4/1.88+1.44+4.8+4(6)+8(11) = 35.88/120.12. From this atomic count one gets $Al_{3.348}Mn$. The Al content is now above the stoichiometric one, in agreement with the starting composition. In this consideration all of the sites are occupied by atoms.

**Table 2.1: Atomic coordinates and occupation probabilities of Taylor phase T-$Al_3Mn$ as reported by Hiraga *et al.* (1993) [17] (*red*) and Klein *et al.* (1997) [15] (blue), and Pavlyuk *et al.* (1995) (green) [16].**

| Atoms | Site | x | y | z | Occupation factor | Total No Mn/Al atoms |
|---|---|---|---|---|---|---|
| *Mn(1)* | *4c* | *0.0420* | *0.25000* | *-0.1462* | *1(Mn)* | *4/0* |
| Mn(1) | | 0.03998 | 0.25000 | 0.85546 | 0.5(Mn) | 2/0 |
| Mn(9) | | 0.0417 | 0.25000 | 0.8530 | 1(Mn) | 4/0 |
| *Mn(2)* | *4c* | *0.2333* | *0.25000* | *0.1783* | *1(Mn)* | *4/0* |
| Mn(2) | | 0.23357 | 0.25000 | 0.17158 | 0.5(Mn) | 2/0 |
| Mn(7) | | 0.2348 | 0.25000 | 0.1749 | 1(Mn) | 4/0 |
| *Mn(3)* | *4c* | *0.0535* | *0.25000* | *0.4543* | *1(Mn)* | *4/0* |
| Mn(3) | | 0.0533 | 0.25000 | 0.4543 | 0.5(Mn) | 2/0 |
| Mn(4) | | 0.052 | 0.25000 | 0.453 | 1(Mn) | 4/0 |
| *Mn(4)* | *4c* | *0.2261* | *0.25000* | *0.5217* | *1(Mn)* | *4/0* |
| Mn(4) | | 0.22730 | 0.25000 | 0.52050 | 0.5(Mn) | 2/0 |
| Mn(6) | | 0.2249 | 0.25000 | 0.5236 | 1(Mn) | 4/0 |
| *Mn(5)* | *4c* | *0.0565* | *0.25000* | *0.2429* | *0.7(Mn)/0.3(Al)* | *2.8/1.2* |
| Al(13) | | 0.05142 | 0.25000 | 0.23361 | 0.5(Al) | 0/2 |
| Mn(5) | | 0.058 | 0.25000 | 0.242 | 0.53(Mn)/0.47(Al) | 2.12/1.88 |
| *Mn(6)* | *4c* | *-0.1669* | *0.25000* | *0.1530* | *0.8(Mn)/0.2 (Al)* | *3.2/0.8* |
| Al(14) | | 0.84274 | 0.25000 | 0.15263 | 0.5(Al) | 0/2 |
| Mn(8) | | 0.8343 | 0.25000 | 0.1540 | 0.64(Mn)/0.36(Al) | 2.56/1.44 |
| *Mn(7)* | *8d* | *-0.1790* | *0.4429* | *0.6519* | *1(Mn)* | *8/0* |
| Mn(5) | | 0.81942 | 0.44376 | 0.65449 | 1(Mn) | 8/0 |

| | | | | | | |
|---|---|---|---|---|---|---|
| Mn(2) | | 0.8202 | 0.4425 | 0.6534 | 1(Mn) | 8/0 |
| *Mn(8)* | *8d* | *-0.1831* | *0.4393* | *0.0379* | *0.5(Mn)/0.5 (Al)* | *4/4* |
| TM(1)(Mn/Al) | | 0.81685 | 0.43746 | 0.03581 | 0.5(Mn)/0.5(Al) | 4/4 |
| Mn(3) | | 0.8167 | 0.439 | 0.0393 | 0.4 (Mn)/0.6 (Al) | 3.2/4.8 |
| *Mn(9)* | *8d* | *0.1268* | *0.4383* | *0.1580* | *0.6(Mn)/0.4 (Al)* | *4.8/3.2* |
| TM(2)(Mn/Al) | | 0.13220 | 0.43691 | 0.15809 | 0.5(Mn)/0.5(Al) | 4/4 |
| Mn(1) | | 0.1281 | 0.0628 | 0.1592 | 0.5(Mn)/0.5(Al) | 4/4 |
| *Al(1)* | *4c* | *0.0937* | *0.25000* | *0.6607* | *1(Al)* | *0/4* |
| Al(1) | | 0.09408 | 0.25000 | 0.66077 | 0.5 | 0/2 |
| Al(12) | | 0.094 | 0.25000 | 0.659 | 1(Al) | 0/4 |
| *Al(2)* | *4c* | *-0.1000* | *0.25000* | *-0.0399* | *1(Al)* | *0/4* |
| Al(2) | | 0.89212 | 0.25000 | 0.94199 | 0.5 | 0/2 |
| Al(15) | | 0.899 | 0.25000 | 0.96 | 1(Al) | 0/4 |
| *Al(3)* | *4c* | *0.1042* | *0.25000* | *0.0403* | *1(Al)* | *0/4* |
| Al(3) | | 0.11555 | 0.25000 | 0.02993 | 0.5 | 0/2 |
| Al(13) | | 0.105 | 0.25000 | 0.039 | 1(Al) | 0/4 |
| *Al(4)* | *4c* | *0.4031* | *0.25000* | *0.1493* | *1(Al)* | *0/4* |
| Al(4) | | 0.39940 | 0.25000 | 0.13536 | 0.5 | 0/2 |
| Al(16) | | 0.403 | 0.25000 | 0.148 | 1(Al) | 0/4 |
| *Al(5)* | *4c* | *0.3196* | *0.25000* | *-0.1559* | *1(Al)* | *0/4* |
| Al(5) | | 0.31703 | 0.25000 | 0.84278 | 0.5 | 0/2 |
| Al(14) | | 0.318 | 0.25000 | 0.845 | 1(Al) | 0/4 |
| *Al(6)* | *8d* | *0.0158* | *0.4357* | *0.3498* | *0.9(Al)/0.1(Mn)* | *0.8/7.2* |
| TM(3)(Mn/Al) | | 0.01204 | 0.43579 | 0.3519 | 0.3(Mn) /0.7(Al) | 2.4/5.6 |
| Al(1) | | 0.0162 | 0.066 | 0.350 | 1(Al) | 0/8 |
| *Al(7)* | *8d* | *-0.1906* | *0.4338* | *0.2701* | *1(Al)* | *0/8* |
| TM(4)(Mn/Al) | | 0.81666 | 0.43358 | 0.27479 | 0.3(Mn) /0.7(Al) | 2.4/5.6 |
| Al(8) | | 0.8097 | 0.434 | 0.2702 | 1(Al) | 0/8 |
| *Al(8)* | *8d* | *0.1296* | *0.4351* | *0.5351* | *1(Al)* | *0/8* |
| TM(5)(Mn/Al) | | 0.12823 | 0.43438 | 0.53195 | 0.15 (Mn)/0.85(Al) | 1.2/6.8 |
| Al(4) | | 0.1299 | 0.435 | 0.535 | 1(Al) | 0/8 |
| *Al(9)* | *8d* | *-0.4797* | *0.4217* | *0.5495* | *1(Al)* | *0/8* |
| Al(6) | | 0.51119 | 0.41030 | 0.53689 | 1(Al) | 0/8 |
| Al(11) | | 0.5193 | 0.421 | 0.549 | 1(Al) | 0/8 |
| *Al(10)* | *8d* | *0.1812* | *0.3525* | *0.3489* | *1(Al)* | *0/8* |
| Al(7) | | 0.18067 | 0.35284 | 0.34743 | 1(Al) | 0/8 |
| Al(5) | | 0.180 | 0.3525 | 0.350 | 1(Al) | 0/8 |
| *Al(11)* | *8d* | *-0.2258* | *0.3785* | *-0.1619* | *1(Al)* | *0/8* |
| Al(8) | | 0.76863 | 0.37970 | 0.83666 | 1(Al) | 0/8 |
| Al(6) | | 0.7736 | 0.3779 | 0.8380 | 1(Al) | 0/8 |
| *Al(12)* | *8d* | *-0.0511* | *0.3736* | *0.5417* | *1(Al)* | *0/8* |
| Al(9) | | 0.95003 | 0.37515 | 0.54539 | 1(Al) | 0/8 |
| Al(2) | | 0.949 | 0.374 | 0.5400 | 1(Al) | 0/8 |
| *Al(13)* | *8d* | *-0.2357* | *0.3763* | *0.4743* | *1(Al)* | *0/8* |
| Al(10) | | 0.76708 | 0.37939 | 0.47575 | 1(Al) | 0/8 |
| Al(7) | | 0.765 | 0.3760 | 0.4740 | 1(Al) | 0/8 |
| *Al(14)* | *8d* | *-0.0491* | *0.3783* | *-0.2380* | *1(Al)* | *0/8* |
| Al(11) | | 0.95384 | 0.38373 | 0.76158 | 1(Al) | 0/8 |
| Al(3) | | 0.9500 | 0.3780 | 0.7600 | 1(Al) | 0/8 |
| *Al(15)* | *8d* | *0.1623* | *0.3764* | *-0.1635* | *1(Al)* | *0/8* |
| Al(12) | | 0.15657 | 0.38402 | 0.83649 | 1(Al) | 0/8 |
| Al(9) | | 0.16291 | 0.3776 | 0.837 | 1(Al) | 0/8 |
| *Al(16)* | *8d* | *-0.0414* | *0.3882* | *0.1490* | *1(Al)* | *0/8* |
| TM(6)(Pd/Al) | | 0.95698 | 0.41779 | 0.15723 | 0.625(Pd) /0.375(Al) | 5/3 |
| Al(10) | | 0.9587 | 0.3919 | 0.1510 | 1(Al) | 0/8 |

Since the atomic positions found by all groups are very similar, we reconstructed the crystal structure with the values of Hiraga *et al*. (1993) [17]. The results for successive layers perpendicular to the b- axis are shown in figure 2.4 and figure 2.5. Most of the

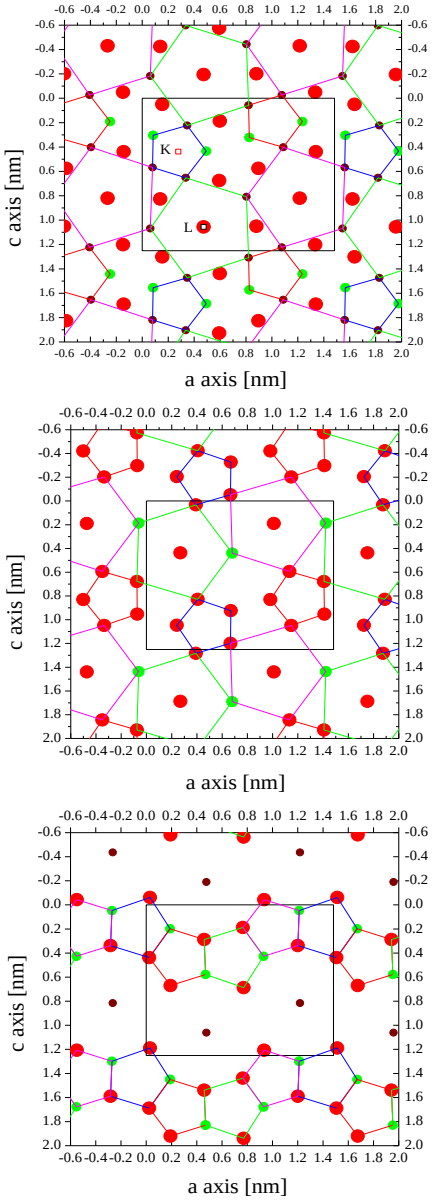


**Figure 2.4: Layers 8d1, 8d2 and 4c1 bottom to top. Brown, green small, green large, and red correspond to positions occupied by Mn, Mn/Al, Al/Mn, and Al. Black line: unit cell. Positions for points K, L are shown in graph of layer 4c1. Small differences in b appearing in layers 8d1, 8d2 are neglected.**

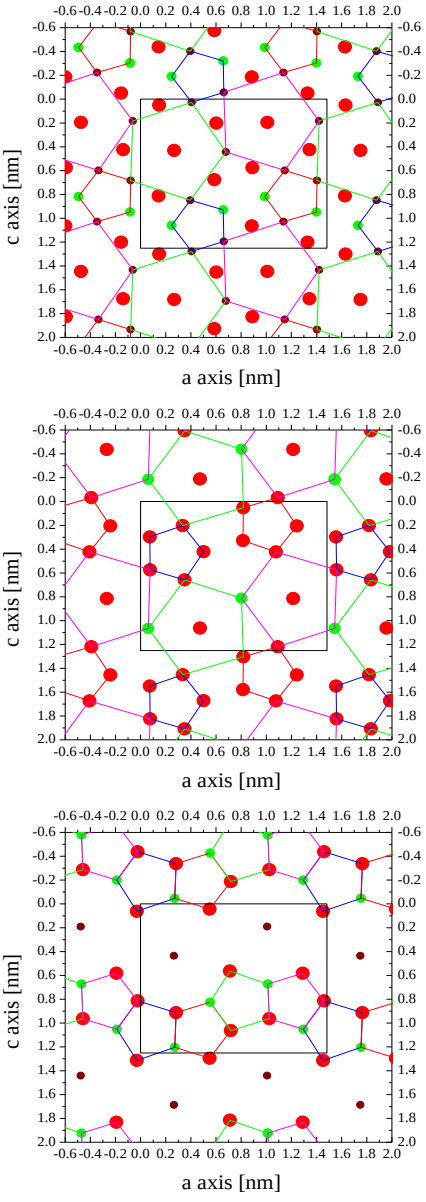


**Figure 2.5: Layers 8d3, 8d4 and 4c2 bottom to top. Symbol colours are as in figure 2.4. Small differences in b appearing in layers 8d3, 8d4 are neglected.**

atoms are located at the vertices of small and large pentagons with edge lengths associated with the golden ratio i.e. $(1+\sqrt{5})/2$ ~ 1.618 [21], and at the centre of large pentagons. The 10 layers forming the unit cell are stacked in the sequence (from bottom to top) 8d1, 8d2, 4c1, 8d2, 8d1, 8d3, 8d4, 4c2, 8d4, 8d3 as schematically shown in figure 2.6. The alternate presence of small pentagons and central atoms leads to pentagonal columns along the *b* axis (as e.g. shown for the K and L positions), which are surrounded by large pentagons and decagons, if surrounding Al atoms are also included.

A possible tiling performed with large pentagons and rhombi is indicated by the lines connecting respective atom sites in figure 2.4 and 2.5. It should, however, be noted that atoms in the layers 8d1, 8d2, 8d3, and 8d4 are slightly shifted along the *b* axis (see figure 2.6).

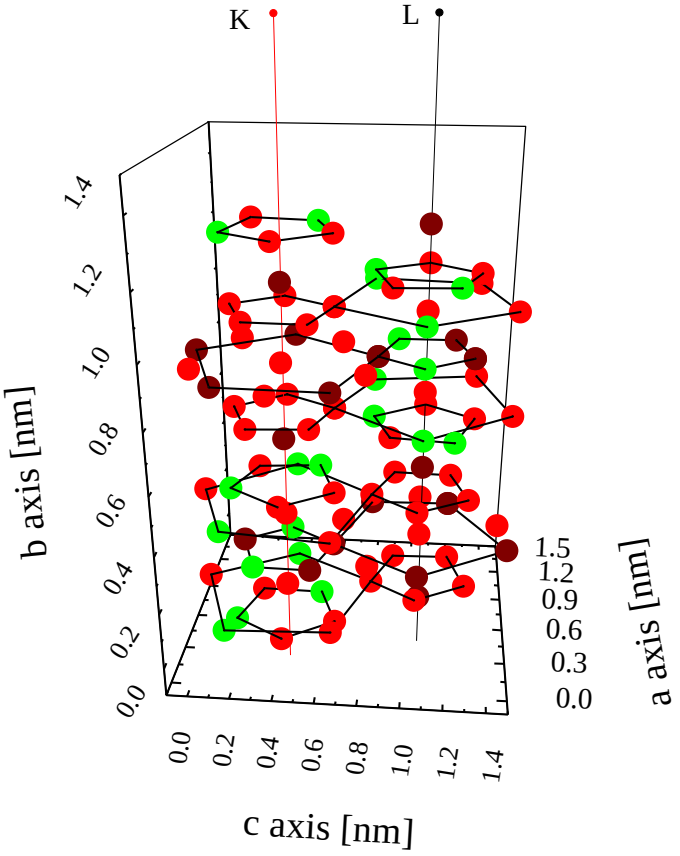


**Figure 2.6: Stacking of similar region of the layers shown in figure 2.4 and 2.5 in the sequence (from bottom to top) 8d1, 8d2, 4c1, 8d2, 8d1, 8d3, 8d4, 4c2, 8d4, 8d3, and 8d1. Lines in red and black correspond to the projections to a-c plane of the points K and L shown in the graph for layer 4c1 in figure 2.4.**

The Taylor phase samples of our interest about which we discussed in the later chapters are $Al_{75}Mn$, $Al_{75}Mn_{20}Pd_5$, $Al_{69}Mn_{23}Fe_8$ and $Al_{68}Mn_{20}Fe_{12}$, which are abbreviated as AM, AMP, AMF8 and AMF12, respectively. AM contains 75% Al and 25% Mn which gives precisely $Al_3Mn$. In the structure model of Klein *et al*. (1997) [15] the amount of 3.2% Pd is embedded only on one Al site and occupation of the other lattice sites is changed compared to the one of pure T- $Al_3Mn$. Assumptions that this preferential substitution holds also for larger Pd content are highly speculative. For the Fe containing alloys the Al content is 69% and 68% for AMF8 and AMF12, respectively. In this case for both structural models the occupation numbers of the atomic sites changes with respect to the one proposed for pure $Al_3Mn$.

### 2.3.2 Pentagonal cluster concept

The pentagonal cluster concept, introduced by Boström and Hovmöller [22], was mainly proposed to make analyses of high resolution electron microscopy investigations

easier. It assumes a fundamental cluster, which is formed in both, the approximant and the quasicrystal. This cluster is similar to a "wheel" with an "axis" and a "tire". Two icosahedra form the axis. They are connected in such a way that the central atom of one icosahedron is the apex atom of the other (figure 2.7, a). This axis, built up like the 19 atom cluster proposed by Romeu [23], is circumscribed by a tire formed from five icosahedra (one of them is shown by wires in figure 2.7, b) which are coupled to each other in the same manner as the axis. One edge of each circumscribing icosahedron is made up by the two central atoms in the icosahedra of the axis. The building up of the complete wheel cluster together with one of the 10 possible triangular faces (marked chequered), which could be shared with another cluster, is shown in figure 2.7, c. In total, the cluster contains 34 atoms.

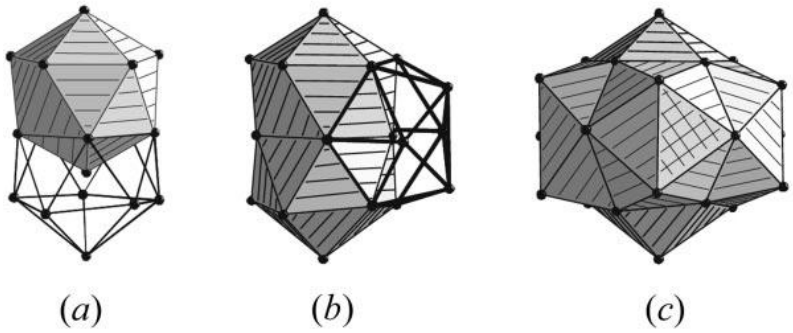


**Figure 2.7: Wheel cluster building up sequence (figure adapted from [22]).**

One-dimensional strands or two-dimensional nets can form by connecting the wheel clusters by the triangular faces to each other. A strand formed by connecting to two other wheel clusters, a net by the connection to three. Two of the possible types of strands, which were already found in approximants, are shown in figure 2.8.

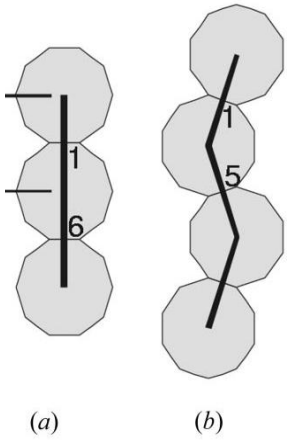


**Figure 2.8: Part of the hypothetical strands (figure adapted from [22]).**

The undulating 1-5 strand (figure 2.8, b) is found in $Al_3Mn$. Two of these strands are in one unit cell and contain with the exception of eight all of the 156 atoms.

### 2.3.3 Decagonal quasicrystals

Restricting to the binary Al-Mn and the ternary Al-Mn-Pd system around the Al concentration of the samples investigated in this thesis, two quasicrystalline compounds are observed, a metastable one around $Al_{3.545}Mn$ and a stable one in Al-(Mn,Pd) alloys with Al content around 70 at%. These compounds exhibiting one-dimensional translational symmetry and long range order were named by Bendersky [14] decagoal phases. Typical is the formation of quasiperiodic columnar clusters with decagonal or pentagonal symmetry arranged parallel to the tenfold screw axis. The long correlation length of these aggregations leads to the observed sharp diffraction spots in high resolution electron microscopy (figure 2.3). The known periodicity ranges from approximately 0.4 nm up to 3.6 nm, which corresponds to 2 up to 18 layers, stacked over each other [24, 25].

Mainly two approaches are used to obtain models for the structure. One is based on the section of a high dimensional (5D) periodic structure with the 3D superplane representing real space. The other (the unit cell approach) is based on the assumption that the crystalline approximants possess the same local atomic arrangement and that this arrangement is packed aperiodically in the quasicrystal (e.g. [10]).

The metastable quasicrystal grows at low Mn concentration on the surface of already formed icosahedral dendrites and nucleates directly from the melt by a first order phase transition at Mn concentration around 22 at% [14]. Electron diffraction exhibits symmetry 10/mmm and systematic extinctions of Bragg reflections which indicate 5D space group symmetry $P10_5/mmc$ [14, 26, and e.g. 27 and references cited herein]. 2D Penrose patterns based on structure factor calculations and 5D symmetry considerations by [28, 10] lead to structure models with six layers along the tenfold axis with periodicity 1.244 nm.

Analysis of single crystal X-ray diffraction investigations lead to full periodicity in 5D space [13, 29, 30]. The structural model (superspace group $P10_5/mmc$) derived in this investigations is also built up by six non-equidistant slightly puckered layers. Two of them are generated by the four 5D atoms in the asymmetric unit. Keeping the occupation probability for Al of superatom 2 fixed to 0.9 occupation factors for Al of 0.84, 0.8, and 0.3 are obtained from the refinement for the remaining three superatoms 1, 3, and 4, respectively. From a comparison of calculated and measured electron density it was estimated that the four superatoms represent only 85% of the electron density of the quasicrystal. The missing 15% are included in the highly disordered part, giving rise to the observed diffuse scattering and indicating a high degree of disorder. The proposed model is in qualitative agreement with the one of Yamamoto and Ishihara [28, 31]. The density derived with three superatoms, however, was too low and splitting of two layers was introduced, finally leading again two four superatoms.

Resemblance of the local atomic arrangement is found to crystalline compounds with different space groups and discussed by [26, 30, 32]. This resemblance was the starting element for the different tiling approaches and the resulting structure models.

Based on comparison with crystalline $\pi$-$Al_4Mn$ structural subunits (hexagon, star, decagon) are arranged on aperiodic flat and puckered layers to form the structure and to lead to electron diffraction patterns comparable to the observed ones [33]. The derived structure model was in general agreement with the one obtained by [30].

Tiling by three types of elements (crown, star and hexagon) was proposed by [34]. Structural subunits were derived under the assumption that the aggregation of the

clusters should exhibit five fold rotational symmetry. The atomic arrangement (also obtained in a subsequent paper by the projection method [35]) within the subunits form flat (F) and pucker (P) layers stacked in the sequence PFp*PFp* to obtain the 1.2 nm periodicity. Layer p (*p*) is related to layer P (*P*) by the mirror plane at layer F (*F*). Layer P consists of two almost flat layers, the one near F contains only Al the other Al and Mn. The same is valid for layer *P* with respect to layer *F*. In spite of some remaining differences in the calculated diffraction patterns the overall agreement with the model proposed by Steurer 1991 [30] was pointed out to be satisfactory. The resulting composition was $Al_{3.897}Mn$ very close to the one reported by [14].

A stable decagonal quasicrystal with composition $Al_{70.5}Mn_{16.5}Pd_{13}$ coexisting with an icosahedral one with slightly higher Pd concentration $Al_{70.5}Mn_{8.5}Pd_{21}$ and an $Al_3Pd_2$ crystalline phase was found by Beeli et al. [36] in samples heat treated around 800°C and finally quenched (first in water and subsequently in liquid nitrogen). Upon annealing at 800°C the orthorhombic $Al_{11}Mn_4$ phase was converted into the decagonal quasicrystal. Four tiles (regular pentagons, 36° rhombi, 72° rhombi, and crowns) allow random tiling with the prominent spots of the electron microscope pattern located at the vertices. Patterns with higher resolution obey highly ordered decagons with bright spots at the centre.

Steurer *et al.*[25] performed X-ray single crystal investigations and applied for the analysis higher dimensional (5D) structure solution, Patterson and Fourier synthesis and least square structure refinement. They restricted the structure analysis to Bragg reflections only and neglected the diffuse scattering. Thus the obtained structure can only be seen as an average of the real disordered structure. They assumed $P10_5/mmc$ for the 5D superspace group and take not into account superatom 3 during the refinement. With these constraints for superatom 1 two pentagons with total occupation factors $p_k$ = 1 and 0.80 were obtained. The partial occupation factors for these components are $p_{Al}$ = 0 (0.79), $p_{Mn}$ = 0 (0.09), and $p_{Pd}$ = 1 (0.12). For atom 2 a pentagram (total occupation factors $p_k$ = 1 and 0.53) with partial occupation factors $p_{Al}$ = 0.5 (0.9), $p_{Mn}$ = 0.5 (0.1), and $p_{Pd}$ = 0 (0), for atom 4 one pentagon (total occupation factor $p_k$ = 1) with partial occupation factors $p_{Al}$ = 1, $p_{Mn}$ = 0, and $p_{Pd}$ = 0, and for atom 5 a pentagram (total occupation factors $p_k$ = 1 and 0.61) with partial occupation factors $p_{Al}$ = 0 (0), $p_{Mn}$ = 0.60 (0.69), and $p_{Pd}$ = 0.40 (0.31) are found. The intensity of the diffuse scattering was of the same order as that of the Bragg scattering pointing to high degree of disorder in the planes. This kind of scattering is not observed in metastable decagonal $Al_{78}Mn_{22}$. Along the periodic direction, however, ordering is perfect, because no diffuse intensities appear in the diffraction pattern. Again the metastable compound is different. There the diffuse intensities indicate a doubling of the period [25]. From the electron density map the cross sections of the columnar clusters were derived (figure 2.9).

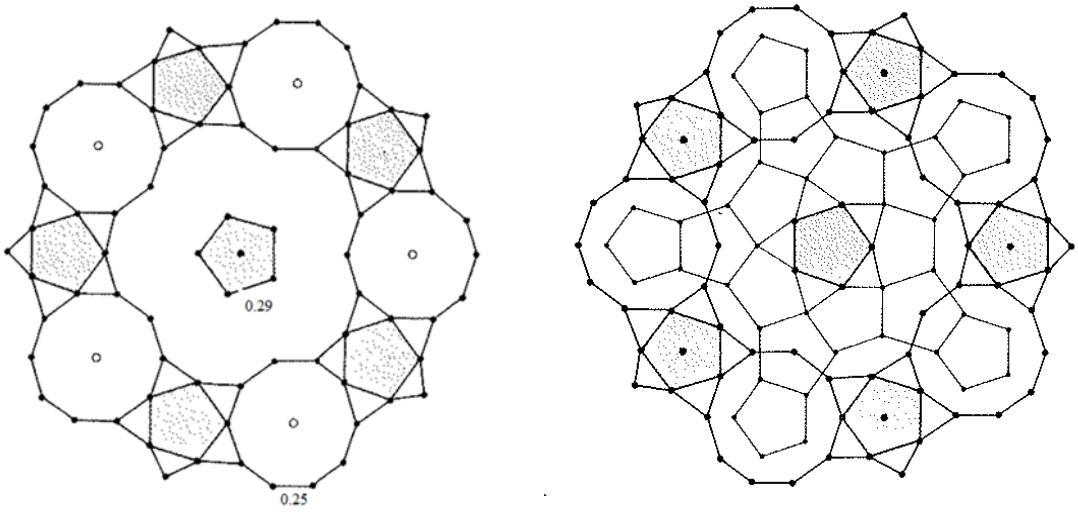


**Figure 2.9: Sections of columns with diameter of 3 nm of $Al_{70.5}Mn_{16.5}Pd_{13}$ for the flat layer at x = 0.25 (left) and the puckered layer between x = 0.065 and 0.115 (right). Taken from [26].**

The structure motifs are interconnected pentagons, trapezoids and decagons. These motifs form the decoration of basic Penrose tiling with rhombi of edge length 0.2518 nm. The in-plane atomic distances (0.2581 nm and 0.296 nm for radius and edge length of small pentagons, respectively) are larger than the shortest interplanar bond lengths (0.232 nm). For comparison, they are in the order of 0.24 to 0.28 for crystalline $Al_3Mn$ [17 and discussion in chapter 6]. The units of pentagonal antiprismatic columns (one at the centre and ten around it) appear to be those structure motifs, which stabilizes the columnar clusters as independent structural building blocks. The crystalline orthorhombic $Al_3Mn$ structure shows similar stacking along the b axis (which is related to the tenfold screw axis of the decagonal phase) as is shown in figure 2.10 for the projection along the b axis of the two puckered 8d1, 8d2 layers and the flat layer 4c1.
This close relationship was also mentioned by Yamamoto 1996 [10] and used by Hiraga and Sun 1993 [37] to propose a structural model for the compound of composition $Al_{70}Pd_{13}Mn_{17}$ with periodicity 1.2 nm, which was also stabilized at 800°C. The structural considerations were based on high-resolution electron microscopy investigations and computer simulations. Structure image indicated the presence of ring contrasts formed by decagons, star shaped pentagons, and squashed hexagons which completely fill the observed area. Using the structure derived for crystalline $Al_3Mn$ [17] and the one for the metastable $Al_{78}Mn_{22}$ [30] and placing a Pd/Mn atom at the centre of the decagons, a structural model was proposed in which two mirror planes are situated at z = 0.25 and 0.75. The other layers necessary to obtain the observed periodicity are located at z = 0.06, 0.12, 0.38, 0.44 and 0.56, 0.62, 0.88, 0.94. The projection of these layers along the periodic axis shows the mentioned decagons, hexagons, and stars indicating that most of the space is filled by atomic columns interconnected to each other. To solve the conflict in composition, the model leads $Al_4$(Mn,Pd), a distribution of the excess Al atom on Mn/Pd positions was proposed. Constructing a Penrose tiling by projecting the 5D-superlattice on the 2D plane in addition to the three above

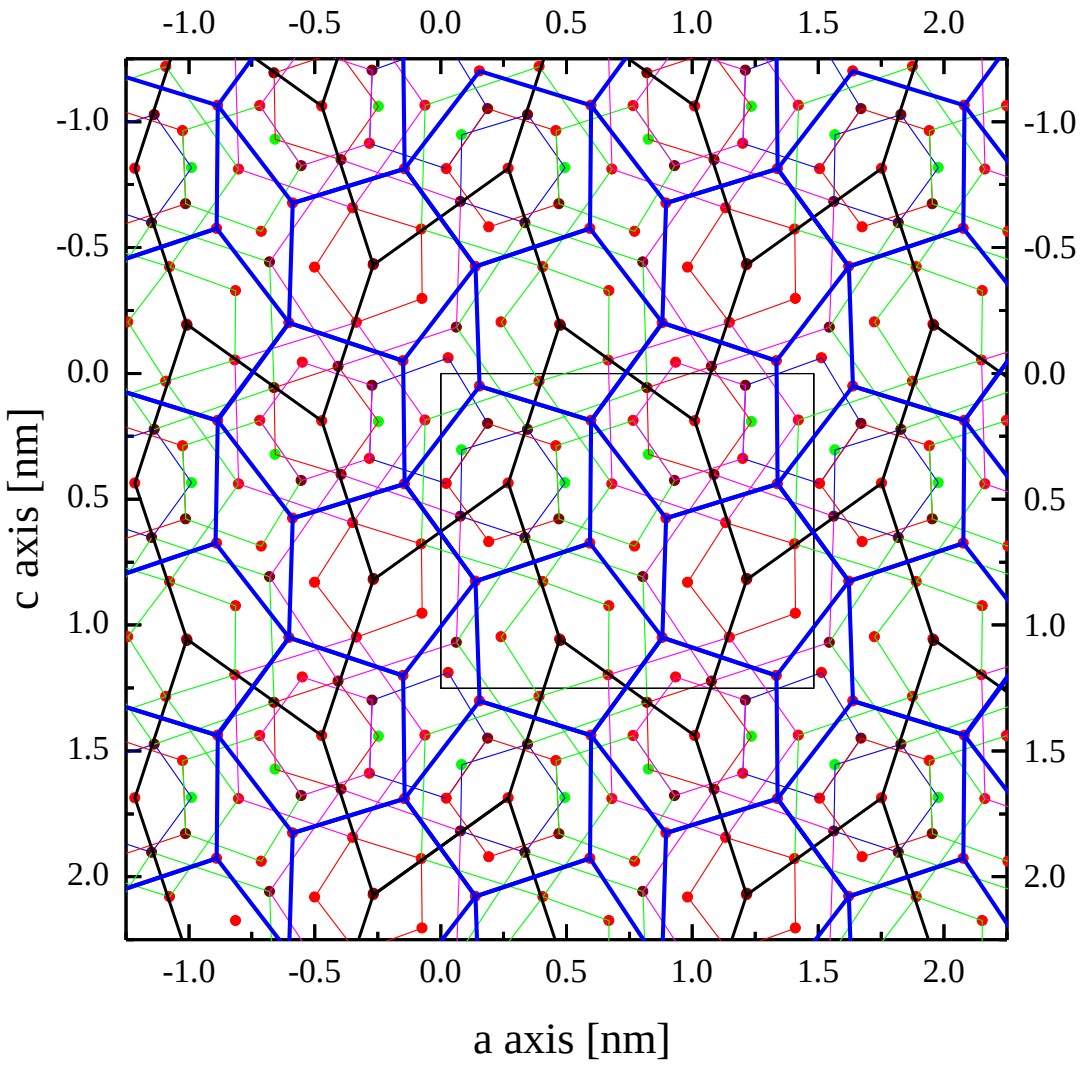


**Figure 2.10: Projection of the two puckered layers 8d1, 8d2 and the flat layer 4c1 along the b-axis for Taylor phase $Al_3Mn$. The building elements formed by pentagons and decagons are shown by coloured lines. Colour of the symbols is the same as in figure 2.4. Tiling as shown in figure 2.2 right is indicated in blue, a possible Penrose tiling in black.**

mentioned tiles a ship-shaped octagon is observed. Since this kind of tile was only observed experimentally in samples annealed for relatively short time, but disappears in the one annealed for longer time, it seems not to be characteristic for stable decagonal quasicrystals. Neglecting the inner part of the decagons (where three pentagons, two rhombi and a crown shaped polygon are arranged), decagons, star shaped pentagons, and squashed hexagons form the main tiles covering the 2D space.

The same structural subunits are derived from comparisons with the approximants $T_3$ AlMnZn [32]. The atomic arrangement results again in a flat and a puckered layer. From these studies it is assumed that the subunits of the stable phase are much larger than the ones representing the metastable phase, since from comparison of the diffraction patterns it follows that the quality of the former crystals is much higher. Agreement with the electron density maps obtained by [25] is in some positions only barely.

To summarize the structural consideration concerning the quasicrystalline compounds, which is based on a certainly arbitrary and incomplete literature survey, $Al_{70.5}Mn_{16.5}Pd_{13}$ can be seen as Pd stabilized isotype of the metastable $Al_{78}Mn_{22}$ phase [25]. The periodicity for both is approximately 1.2 nm according to which two quasi periodic layers A (puckered) and B (planar) are observed. The stacking along the periodic axis is ABAaba (small letters denote rotation of the layer by 36° against the one with large letters). The 5D space group is centrosymmetric, $P10_5/mmc$ [25]. Building elements are columnar clusters with typical diameters of 2 nm. The edge lengths for decagons and pentagons forming these clusters are 0.25 nm and 0.29 nm, respectively, which are larger than the short inter-planar bond lengths of 0.232 nm [25, 26].

In both the quasicrystalline and the crystalline phase a strong tendency for the formation of pentagonal and decagonal clusters is found. Whereas some of these decagons gets irregular in the crystalline phase, in the corresponding quasicrystalline layer they get regular and appear isolated or in pentagonal clusters. The formation of undistorted regular pentagons and decagons may thus be favourable energetically [25].

The decagonal sample on which we did our measurements has a composition of $Al_{71}Mn_{19}Fe_{10}$ which is abbreviated as AMF10. The structural characterization was performed by Feuerbacher [38].

## 2.4 References


[1] http://en.wikipedia.org/wiki/Crystal_structure Oct (2009).

[2] http://jcrystal.com/steffenweber/qc.html Oct (2009).

[3] C. Kittel 1996 *Introduction to solid state physics*, (7ed. Wiley, New York).

[4] D. Shechtman, I. Blech, D. Gratias and J.W. Cahn *Phys. Rev. Lett.* **53** (1984), 1951-1953.

[5] H-R. Trebin 2003 *Quasicrystals Structure and Physical Properties* (Wiley, Morlenbach, Germany).

[6] J.B. Suck 2002 *Quasicrystals an Introduction to Structure, Physical Properties and Applications* (Springer, New York).

[7] A.P. Tsai *Sci. Technol. Adv. Mater.* **9** (2008), 013008 (20pp).

[8] H. Wang *Bell Systems Tech. J.* **40** (1961), 1-41.

[9] S.E. Burkov *Phys.Rev.Lett.* **67** (1991), 614-617.

[10] A. Yamamoto *Acta Cryst. A* **52** (1996), 509-560.

[11] S. Balanetskyy, G. Meisterernst, M. Heggen and M. Feuerbacher *Intermetallics* **16** (2008), 71-87.

[12] A. Yamamoto *Sci. Technol. Adv. Mater.* **9** (2008), 013008 (14pp).

[13] W. Steurer *Acta Cryst. B* **45** (1989), 534-542.

[14] L. Bendersky *Phys. Rev. Lett.* **55** (1985), 1461-1463.

[15] H. Klein, M. Boudard, M. Audier, M. De Boissieu, H. Vincent, L. Beraha and M. Duneau *Phil. Mag. Lett.*, **75** (1997), 197-208.

[16] V.V. Pavlyuk, T.I. Yanson and O.I. Bodak *Acta Cryst. C* **51** (1995), 792-794.

[17] K. Hiraga, M. Kaneko, Y. Matsuo and S. Hashimoto *Phil. Mag. B*, **67** (1993), 193-205.

[18] M.A. Taylor *Acta Cryst.***14** (1961), 84 (1pp).

[19] N.C. Shi, X.Z. Li, Z.S. Ma and K.H. Kuo, *Acta Cryst. B* **50** (1994), 22-30.

[20] T. Gödecke and R. Lück, *Z Metallkunde* **86** (1995), 109-121.

[21] F. Hippert, V. Simonet, G. Trambly de Laissardière, M. Audier and Y. Calvayrac *J. Phys. B Cond. Matter* **11** (1999), 10419-10435.

[22] M. Boström and S. Hovmöller *Acta. Cryst. B*, **57** (2001) 646-651.

[23] D. Romeu, *Phil. Mag. B* 67 (1993), 77-96.

[24] K. Hiraga *J. of Non-Cryst. Solids* **153-154** (1993), 28-32.

[25] W. Steurer, T. Haibach, B. Zhang, C. Beeli, and H.U. Nissen *J Phys.: Cond. Matter* **6** (1994), 613-632.

[26] W. Steuer *J. of Non-Cryst. Solids* **153-154** (1993), 92-97.

[27] S. Ranganathan, K. Chattopadhyay, A. Singh and K. F. Kelton *Progress in Mat. Sci.* **41** (1997), 195-240.

[28] A. Yamamoto and K.N. Ishihara *Acta Cryst. A* **44** (1988), 707-714.

[29] W. Steurer and J . Mayer *Acta Cryst. B* **45** (1989), 355-359.

[30] W. Steurer *J. Phys.: Cond. Matter* **3** (1991), 3397-3410.

[31] K.N. Ishihara and A. Yamamoto *Acta Cryst. A* **44** (1988), 508-516.

[32] X.Z. Li and J.M. Dubois *J Phys.: Cond. Matter* **6** (1994), 1653-1662.

[33] X.Z. Li and K.H. Kuo *Phil. Mag. B* **65** (1992), 525-533.

[34] X.Z. Li *Acta Cryst. B* **51** (1995), 265-270.

[35] X.Z. Li and F. Frey *Acta Cryst. B* **51** (1995), 271-275.
[36] C. Beeli, H.U. Nissen and J. Robadey *Phil. Mag. Letters* **63** (1991), 87-95.
[37] K. Hiraga and W. Sun *Phil. Mag. Letters* **67** (1993), 117-123.
[38] M. Feuerbacher private communication.

# 3. Spin Glass

The following should only be seen as a short and very comprehensive overview without any intention to summarize the extended literature. A spin glass is a magnet with frustrated interactions, augmented by stochastic disorder, where usually ferromagnetic and antiferromagnetic (AF) bonds are randomly distributed [1]. For this state, two ingredients are necessary: There must be competition among the different magnetic exchange interactions between the moments, in the sense that no single configuration of the spins is uniquely favored by all the interactions (this is commonly called 'frustration'), and these interactions must be at least partially random. These facts suggest that the spin glass state is intrinsically different from conventional forms of order and requires own formal concepts to be described [2].
In the last years spin glass systems have been investigated to a large extent, but in spite of the huge number of papers, many characteristic properties remain not fully understood [1, 3-6].

## 3.1 Frustration

In a square lattice with nearest-neighbor AF interaction as shown in figure 3.1(*a*) no magnetic frustration is present, since all spins on this square lattice are antiparallel and satisfy nearest-neighbor AF interactions. However, in a triangular lattice as shown in figure 3.1(b) geometrical frustration occurs, since it is not possible to orient the spin on the third site to satisfy the requirement of AF nearest-neighbor interactions with the other two spins [7].

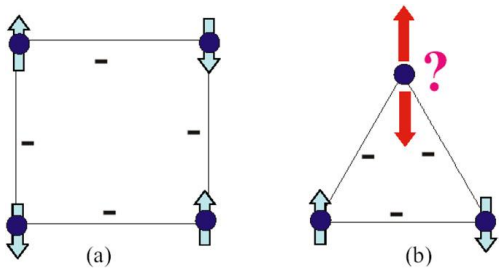


**Figure 3.1: (a) depicts no magnetic frustration in square lattice but (b) depicts frustration in triangular lattice. Taken from [7].**

## 3.2 Disorder

Due to some frozen-in structural disorder the interactions between the magnetic moments may get "in conflict" with each other. Thus no conventional long-range order (of ferromagnetic or antiferromagnetic type) can be established. Nevertheless these systems exhibit with decreasing temperature a "freezing transition" at $T_f$ to a state with a new kind of "order" in which the spins are aligned on random directions. The nature of this new kind of order as well as the character of the freezing transition is still not fully

explained. The concepts range from a new type of phase transition [8] to fail for establishing complete thermal equilibrium during observation time [7, 3].

## 3.3 Zero field cooling (ZFC) and field cooling (FC)

Among the exceptional properties of spin glasses compared to other magnetic materials is the temperature behavior of their magnetic susceptibility, which reveals a kink at the temperature $T_f$ whose shape and position depend on magnitude and frequency of the probing field [3].

There are two distinct ways to measure the susceptibility with a small dc field. The first is to apply the field far above $T_f$ and cool the sample in this field to $T < T_f$ all the while recording the magnetization $M$, this method is called field cooling (FC). Secondly, we can cool the sample in zero field far below $T_f$ and apply the field at this low temperature. Then, we heat the sample while measuring $M$ to $T > T_f$. Here we use the term zero field cooling (ZFC). Figure 3.2 illustrates the different temperature dependencies obtained for the susceptibility $\chi$ measured with a field of 0.6 mT with FC and ZFC conditions for CuMn (1 and 2 at % Mn [9, 10]). The FC susceptibility becomes constant in value and to a great extent independent of time if we stop and wait at a given $T < T_f$. (Only at extreme sensitivities and very long waiting times is there a drift in $\chi$). On the other hand the ZFC susceptibility is zero until the field is applied then with the field on and $T$ constant, the ZFC susceptibility jumps to a value comparable with that found from $\chi_{ac}$. However, now there is a slow, clear drift upwards which continues over many decades in times.

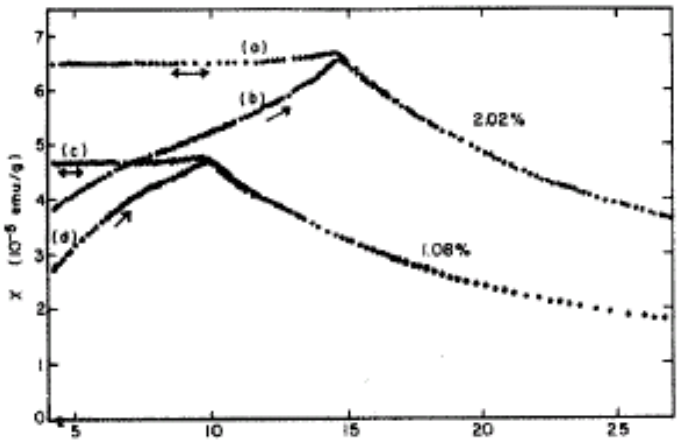


**Figure 3.2: Field cooled (a), (c) and zero field cooled (b), (d) for CuMn (1 and 2 at. %Mn) as a function of temperature; taken from [9, 10].**

The first kind of system to be studied widely consisted of dilute solutions of magnetic transition metal impurities in noble metal hosts, like AuFe, AgMn and CuMn [11]. The impurity moments produce a magnetic polarization of the host metal conduction electrons around them which is positive at some distances and negative at others [1].

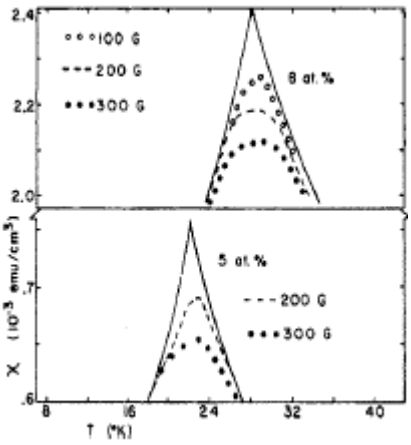


**Figure 3.3: AC-susceptibility data for AuFe with 5 and 8 at %Fe for zero external fields (full lines) and for various applied static fields; from Canella and Mydosh [11].**

It was in the early 1970s that sharp cusps were discovered in the ac susceptibility of the so called 'canonical' spin glasses AuFe and CuMn [11]. $T_f$ was defined by the (frequency dependent) maximum in $\chi_{ac}$. Figure 3.3 shows how an applied dc-field rounds off the peak. Notice that the peak decreases in magnitude and shifts to lower temperatures as the external field increases. Already in applied fields of 20-30 mT the peak is smeared out and a broad maximum remains. This field effect is surprising, since we have a $T_f$ of ~ 25 K being strongly affected by an external field of ~ 10 mT, although $k_B T_f >> \mu_{eff} B_a$. (Assuming $\mu_{eff}$ = 10 $\mu_B$, then 10 mT corresponds to a temperature of 0.067 K.) Such distinct temperature effects were totally unexpected from early speculation based upon a random molecular field model and the previously measured high field susceptibilities. This means that spin glass state has a peculiar sensitivity even to a small external field.

## 3.4 Magnetic interactions

The different types of magnetic interactions, which can be important in allowing the magnetic moments in a solid to interact with each other and may lead to magnetic order, can be Dipole–Dipole, Tunnelling Exchange, Superexchange, Direct Exchange, and Ruderman-Kittel-Kasuya-Yosida (RKKY) interaction. The last two are of special importance with respect to the values of the obtained freezing temperatures.

The (indirect) RKKY exchange is usually considered in metals. The local magnetic moments interact co-operatively with each other via the conduction electrons [12]. Theoretical and experimental work on (weakly) disordered metals with elastic mean free path $l > 1/k_F$ and $< R$ (the intermoment spacing) shows that the interaction is not exponentially damped, but its sign is alternating and depend on $R$ e.g. [13-17]. Combined with the spatial disorder this provides conditions for a spin-glass state [18]. Investigations of the characteristics of conduction electrons by electrical transport experiments follow immediately the first works on spin glasses [19-23]. The results point to clustering and magnetic correlations far above $T_f$, but are too complex to be described by present scattering theories [1].

Direct Exchange interaction, especially between *d* electrons, may lead to the formation of magnetically correlated regions, the size of which is strongly dependent on the local

spatial atomic order. Special care has to be taken to distinguish this state from the superparamagnetic one [1, 24].
Other interactions, for instance the dipole interaction of the magnetic moments (which also introduce anisotropy into the considerations), have been considered (e.g. [25, 1]). The resulting exchange energies are, however, low as compared with the freezing temperatures.

## 3.5 Dynamics

Spin glasses differ from most magnetic materials in having dynamics on many time scales. The magnitude of magnetization created by an external magnetic field below $T_f$ depends on the pre-history of the system. For example, if one measures the susceptibility in fields oscillating with different frequencies one may get different results at all measuring frequencies, indicating that the system has characteristic excitation and relaxation times (figure 3.4). These characteristic times can at low temperatures by far exceed the duration of the experiment.

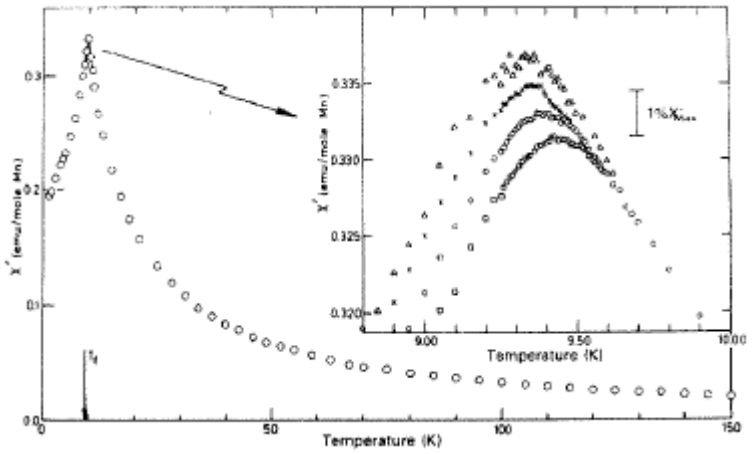


**Figure 3.4: Zero field susceptibility as a function of temperature and various measuring frequencies; from Mulder *et al.* [1, 26].**

If the time dependence is described in the simplest way as a thermally activated process with one characteristic barrier, an exponential decrease according to a simple Debye process

$$M(t) = M(0)\exp(-t/\tau) \tag{3.1}$$

is expected, where the characteristic relaxation time $\tau$ is given by the Arrhenius equation

$$\tau = \tau_0 \exp(E/kT) \tag{3.2}$$

$E$ is the effective barrier height, which has to be overcome by thermal activation. A logarithmic instead of the before mentioned exponential time dependence is an indication that not one energy barrier but a broad distribution of barrier energies is present. In that case the centre of gravity of the distribution leads to the mean activation energy $E$. The logarithmic behavior allows the determination of a creep rate

$$\Gamma = dM/d\ln t \tag{3.3}$$

which is related to the effective barrier height by

$$E = kT\,(dM/d\theta)/\Gamma \tag{3.4}$$

where $\theta = T/T_f$ [27].

A second method of analysis is taken from the investigations on real glasses. The empirical law to describe the viscosity of supercooled liquids is called Vogel-Fulcher law [28]. Written for use in describing $T_f$ shifts with measuring frequency this becomes

$$\omega = \omega_0 \exp\left[-E_a/k_B\left(T_f - T_0\right)\right] \tag{3.5}$$

$T_0$ is a new parameter, without precise physical meaning, for which some attempts have been made to relate it to the interaction strength by assuming the presence of clusters in a spin glass [1].

A third approach draws on the standard theory for dynamical scaling near a phase transition at $T_c$ [5, 6]. The conventional results for dynamical scaling relates the critical relaxation time $\tau$ to the correlation length $\xi$ as $\tau \sim \xi^z$ . Since $\xi$ diverges with temperature as $\xi \sim [T/(T\text{-}T_c)]^{\nu}$, we can write for spin glasses on approaching $T_f$ from above [29, 30]

$$\tau = \tau_0 \left(\frac{T-T_f}{T_f}\right)^{-z\nu} \tag{3.6}$$

Fitting with this equation leads to reasonable and perhaps not unphysical values. The problem which remains is that for $z\nu$ values around 10 were obtained from magnetic measurements whereas values around 2 follow from high field Mössbauer and Muon Depolarization (μSR) measurements as well as Monte Carlo simulations [31].

Dynamics of magnetic correlations have been observed in spin glasses up to temperatures ten times the freezing temperature. Examples for detailed investigations performed by Mössbauer measurements are given in [32], μSR (Uemura *et al.* [33], Keren *et al.* [34]), neutron spin echo (Murani [35, 36] and Mezei [37]) and for high field Mössbauer measurements (Pösinger *et al.* [38-44] and Bogner *et al.* [45-48]).

## 3.6 Spin Glass Models and Theories

In 1975 Edwards and Anderson (EA) proposed the picture for the sudden random freezing of a spin glass [8]. Based on this approach Sherrington and Kirkpatrick (SK) developed a mean field theory (MFT) for Ising spin glasses within an infinite-range EA model where every spin couples equally with every other spin. The exchange coupling on two different moment-pairs *i* and *j* is assumed to be Gaussian. The variance and the mean of this distribution is determined by the demand of infinite range. Using the "replica trick" (the replicas, reflecting the spin configuration, are treated as undistinguishable) they ended up with an order parameter (linear in *T*) from which both the observed phase diagram with transitions from the paramagnetic to the spin glass state and the temperature dependence of the susceptibility exhibiting the experimentally observed cusp are obtained. The most important problem which remains, however, is the negative value of the entropy at low temperature. Detailed analysis of the SK model

showed that its solution is unstable at these temperatures both in the spin glass and in the ferromagnetic regime [48]. In the presence of an external field the instability follows the AT-line given by

$$T_f(B_a) = T_f(0) - aB_a^{2/3} \tag{3.7}$$

($a$ is a constant which can be exactly determined for an Ising spin glass) [1].
To overcome the problems of the SK model, Parisi in 1979 [50] introduced a replica symmetry breaking scheme by which the restriction of indistinguishableness of the replicas is removed by an iterative procedure. In the limit of infinite number of iterations the size for the subdividing blocks of the order parameter matrix gets continuous, thus the information for all order parameters in the different sub-blocks is condensed in the function $q(x)$ (Parisi order parameter) and $0 \leq x \leq 1$ correspond the unit interval [4]. From this it follows that below $T_f$ the susceptibility is independent of temperature, strongly resembling the results obtained from FC measurements, and that the entropy at $T = 0$ is zero. By defining an "overlap" and a "distance" for two spin states the picture of a "multi-valley landscape" for the free energy can be derived where beside the pure equilibrium states many metastable minima at higher energies are present, which can be populated on cooling the spin glass below $T_f$ [1, 4]. The time necessary to go from one valley to an other depends on the height of the lowest saddle point in the barrier between these valleys indicating the presence of many relaxation times.

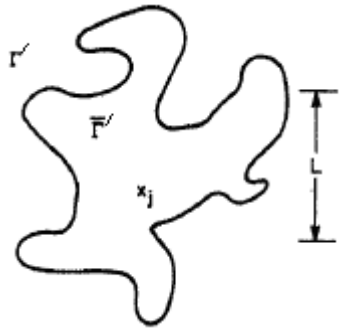


**Figure 3.5: Schematic picture of the droplet model. A droplet of length scale L has all its spins reversed, creating ground state Γ´; from Fisher and Huse [55-57].**

Remaining in mean field theory and avoiding the replica method Thouless *et al.* [51, 1, 4] derived an order parameter quadratic in temperature for the low temperature regime and linear in $T$ near $T_f$ by subtracting a "reaction field" from the Weiss molecular field. The susceptibility and the entropy go to zero, for zero temperature.
A completely different approach was performed by McMillan [53, 53] and Bray and Moore [54] in a series of numerical studies of domain walls and their scaling properties. Fisher and Huse [55-57] broadened these intention and presented the "droplet model" as a phenomenological scaling theory of droplet excitations in short-range Ising spin glass phases. The phenomenological approach is based on the existence of a distribution of droplets or dynamical domains [58] of correlated reversed spins and account fairly well

for some experimentally derived properties [59]. The basic idea is to define a 'droplet' in the ground-state as the lowest energy excitation of length scale $L$ around a particular point $x_j$. Within this droplet all spins are placed in the opposite direction with respect to those in the ground state (figure 3.5). A broad distribution of free energies $F_L \alpha Y(T)L^{\Theta}$, where $Y$ is the stiffness constant and $\Theta$ a new exponent, characterizes the droplets. If $\Theta > 0$, as is expected for $d = 2$, then the low-lying excitations can be created on longer and longer length scales, thereby destroying the frozen spin glass phase. Computer simulations indicate that $\Theta$ becomes positive just below $d = 3$, so a marginal phase transition is anticipated for 3D spin glass. A distribution of droplet free energies $\rho(F_L)$ can be determined, and then correlations between the droplet free energies are calculated . This leads to non-linear susceptibility $\chi$ which is infinite when $d > (1+\varphi)\Theta$ ($\varphi$ is an exponent governing the dependence of $\rho$ and $F_L$). Hence, a true phase transition is expected when this condition is satisfied [28]. Annihilation and creation of droplet excitations determine the equilibrium low-frequency dynamics of the ordered phase. Thermal activation over energy barriers is assumed for those droplets which are thermally active. The characteristic time for the droplet to form or grow to scale $L$ is that necessary to surmount this energy barrier. Thus a droplet of scale $L$ will last for

$$\tau = \tau_0 \exp\left(\frac{E_B}{k_B T}\right) \tag{3.8}$$

where the free energy barrier $E_B$ can be scaled by $E_B \approx L^{\psi}$ with $\psi$ being a new independent exponent $\Theta \leq \psi \leq d-1$. This scaling equation leads to an extremely slow logarithmic decay of temporal correlations.

Malozemoff and Barbara [60] proposed the fractal cluster model, a scaling theory of spin glasses by considering clusters of correlation length $\xi$ diverging as $[(T-T_f)/T_f]^{-\nu}$. Markovian, Two Level Jump Processes (MTJP) can be used to describe the existence of short-range correlations up to temperatures several times $T_f$ as was proved by a number of experiments e.g. [38 - 48]. The growth in size with decreasing temperature, as well as rotations in external fields, of the net magnetization of these correlated regions is used as an explanation for the experiments [31].

## 3.7 References


[1] J.A. Mydosh 1993 *Spin Glasses: an experimental introduction* (Taylor & Francis London. Washington, DC).

[2] A. Alloul 1983 *In Heidelberg colloquium on spin glasses* (Ed. J.L. van Hemmen and L. Morgenstrn, Springer, Berlin) **192** page 18-37.

[3] K. Binder and A.P. Young, *Rev. Mod. Phys.* **58** (1986), 801-976.

[4] K.H. Fischer and J.A. Hertz 1991 *Spin Glasses* (Cambridge University Press, Cambridge).

[5] M. Mezard, G. Parisi and M.A.Virasoro 1987 *Spin Glass Theory and Beyond* (World Scientific, Singapore).

[6] D. Chowdhury 1986 *Spin glasses and other frustrated systems* (World Scientific, Singapore).

[7] S. Bedanta and W. Kleemann *J. Phys. D: Appl. Phys.* **42** (2009), 013001 (28pp).

[8] S.F. Edward and P.W. Anderson *J. Phys. F* **5** (1975), 965-974.

[9] P. Nordblad, P. Svedlindh, L. Lundgren and L. Sandlund *Phys. Rev. B* **33** (1986), 645-648.

[10] L. Sandlund, P. Svedlindh, P. Granberg, P. Nordblad and L. Lundgren *J. Appl. Phys.* **64** (1988), 5616-5618.

[11] V. Canella and J.A Mydosh *Phys. Rev. B* **6** (1972), 4220-4237.

[12] A.J. Freeman 1972 *In Magnetic Properties of Rare Earth Metals* (Ed. R. J. Elliott Plenum, London. page 245-333).

[13] F. Hellman, D.R. Queen, R.M. Potok, and B.L. Zink *Phy. Rev. Lett.* **84** (2000), 5411-5414.

[14] P.F. de Chatel *J. Magn. Magn. Mater.* **23** (1981), 28-34.

[15] K.M. Wong and S. J. Poon *J. Magn. Magn. Mater.* **42** (1984), 130-138.

[16] D.C. Vier and S. Schultz *Phys. Rev. Lett.* **54** (1985), 150-153.

[17] A. Jagannathan, E. Abrahams and M.J. Stephen *Phys. Rev. B* **37** (1988), 436-441.

[18] B. Gorshunov, A.S. Prokhorov, S. Kaiser, D. Faltermeier, S. Yasin, M. Dumm, N. Drichko, E.S. Zhukova, I.E. Spektor, S. Vongtragool, M.B.S. Hesselberth, J. Aarts, G.J. Nieuwenhuys and M. Dressel *Europhys. Lett.* **76** (2006), 938-944.

[19] J.W. Loram, T.E. Whall and P.J. Ford *Phys. Rev. B* **2** (1970), 857-874.

[20] P.J. Ford, T.E. Whall and J.W. Loram *Phys. Rev. B* **2** (1970), 1547-1553.

[21] J.A. Mydosh, P.J. Ford, M.P. Kawatra and T.E. Whall *Phys. Rev. B* **10** (1974), 2845-2856.

[22] P.J. Ford and J.A. Mydosh *Phys. Rev. B* **14** (1976), 2057-2070.

[23] I.A. Campbell, P.J. Ford and A. Hamzic *Phys. Rev. B* **26** (1982), 5195-5206.

[24] K.H. Fischer and J.A. Hertz 1991 *Spin Glasses* (Cambridge University Press, Cambridge).

[25] D.A. Smite *J. Phys. F* **5** (1975), 2148-2167.

[26] C.A.M. Mudler, A.J van Duyneveldt and J.A. Mydosh Phys. Rev. 25 (1982), 515-518.

[27] J. Souletie *J. Physique* **41** (1983), 1095-1116.

[28] N.W. Ashcroft and N.D. Mermin 1976 *Solid State Physics* (Saunders College Publishing, New York).

[29] I.S. Suzuki and M. Suzuki *Phys. Rev. B* **68** (2003), 094424 (13pp).
[30] A.T. Ogielski *Phys. Rev. B* **32** (1985), 7384-7398.
[31] J. Bogner 2002 *Dissertation* (TU Wien).
[32] R.J. Borg and C.E. Violet *J. Phys. Chem. Solids* **48** (1987), 1239-1244.
[33] Y.J. Uemura, T. Yamazaki, D.R. Harshman, M. Senba and E.J. Ansaldo *Phys. Rev. B* **31** (1985), 546-563.
[34] A. Keren, P. Mendels I.A. Campbell and J. Lord *Phys. Rev. Lett.* **77** (1996), 1386-1389.
[35] A.P Murani *J. Phys.* **39** (1978), C6-1517-1526.
[36] A.P Murani, *J. Magn. Magn. Mat.* **22** (1981), 271-281.
[37] F. Mezei *J. Magn. Magn. Mat.* **31-34** (1983), 1327-1330.
[38] A. Pösinger 1992 *Dissertation* (TU Wien).
[39] A. Pösinger, M. Reissner and W. Steiner *Physica B* **155** (1989), 211-214.
[40] A. Pösinger, H. Winkler, W. Steiner, A.X. Trautwein and M. Reissner *J. Phys. Condens. Matter* **5** (1990), 3653-3662.
[41] A. Pösinger, M. Reissner, W. Steiner, H. Winkler and A.X. Trautwein *Hyperfine Interact.* **67** (1991), 621-626.
[42] A. Pösinger, H. Winkler, W. Steiner, A.X. Trautwein and M. Reissner *J. Phys. Condens. Matter* **3** (1991), 2713-2719.
[43] A. Pösinger, W. Steiner, H. Winkler, A.X. Trautwein and Y. Yoshida *J. Magn. Magn. Mat.* **104-7** (1992), 1597-1598.
[44] A. Pösinger, W. Steiner, H. Winkler, A.X. Trautwein and Y. Yoshida *Hyperfine Interact.* **70** (1992), 1117-1120.
[45] J. Bogner, H. Schachner, M. Reissner and W. Steiner *J. Phys.* **51** (1998), 349-362.
[46] J. Bogner, M. Reissner, W. Steiner and S.M. Dubiel *J. Phys. Condens. Matter* **10** (1998), 9849-9858.
[47] J. Bogner, M. Reissner and W. Steiner *J. Magn. Magn. Mat.* **196-197** (1999), 641-643.
[48] J. Bogner, M. Reissner, W. Steiner M.T.F Telling and R. Cywinski, *J. Magn. Magn. Mat.* **226** (2001), 1319-1320.
[49] J.R.L. de Almeida and D.J. Thouless *J. Phys. A: Math. Gen.* **11** (1978), 983-990.
[50] G. Parisi *Phys. Rev. Lett.* **23** (1979), 1754-1756.
[51] D.J. Thouless, Anderson and R.G. Palmer *Phil. Mag.* **35** (1977), 593-601.
[52] W.L. McMillan *Phys. Rev. B* **30** (1980), 476-477.
[53] W.L. McMillan *J. Phys. C* **17** (1984), 3179-3187.
[54] A.J. Bray and M.A. Moore *J. Phys. C* **17** (1984), L463-468 and L613-619.
[55] D.S. Fisher and D.A. Huse *Phys. Rev. Lett.* **56** (1986), 1601-1604.
[56] D.S. Fisher and D.A. Huse *Phys. Rev. B* **38** (1988), 373-385.
[57] D.S. Fisher and D.A. Huse *Phys. Rev. B* **38** (1988), 386-411.
[58] G . Koper and H. Hilhorst *J. Phys. (Paris),* **49** (1988), 429-444.
[59] H. Yoshino, A. Lemaitre, and J.-P. Bouchaud *Eur. Phys. J. B* **20** (2001), 367-395.
[60] B. Barbara, A.P. Malozemoff and Y. Imry *Phys. Rev. Lett.* **47** (1981), 1852-1855.
[61] I.A. Campbell, A. Amata, F.N. Gygax, D. Herlach, A. Schenck, R. Cywinski and S.H. Kilcoyne *Phys. Rev. Lett.* **72** (1994), 1291-1294.

# 4. Sample Characterization

An icosahedral phase I (Icosahedral *Pm35*) and a decagonal phase D (Decagonal $P10_5/mmc$) with parameter b = 1.240 nm are stable in the Al-Mn-Pd system [1]. Two other ternary phases T and R of orthorhombic symmetry are also known. The Taylor phase, variously called T-$Al_3Mn$, $Al_4Mn_{11}$ (HT) or H (space group *Pnma*), has a homogeneity range in the binary Al-Mn system as indicated in figure 4.1, which gets enlarged in the ternary Al-Mn-Pd system. Typical lattice parameters are a = 1.4873-1.4726 nm, b = 1.2420-1.2514 nm and c = 1.2547-1.2605 nm [1]. The orthorhombic R phase (space group *Bbmm*, Pearson symbol *oS*156, structure type $Al_{31}Mn_6Ni_2$) has lattice parameters of a = 2.388 nm, b = 1.243 nm and c = 0.778 nm and occurs around the composition $Al_{80}Mn_{15}Pd_5$. The literature data on the ternary phases of this system were reviewed by [1, 2]. It was shown that the orthorhombic T-phase is a high temperature phase in both the binary Al-Mn system and the Pd-poor ternary Al-Mn-Pd system. During solidification this phase is involved in several reactions which lead to the formation of seven three-phase isothermal surfaces in the solidus (figure 4.1). The homogeneity region is extended into the ternary region of Al-Mn-Pd as a solid solution (gray area in figure 4.1) and no indication for the existence of different orthorhombic T-phases as reported by [3] were found.

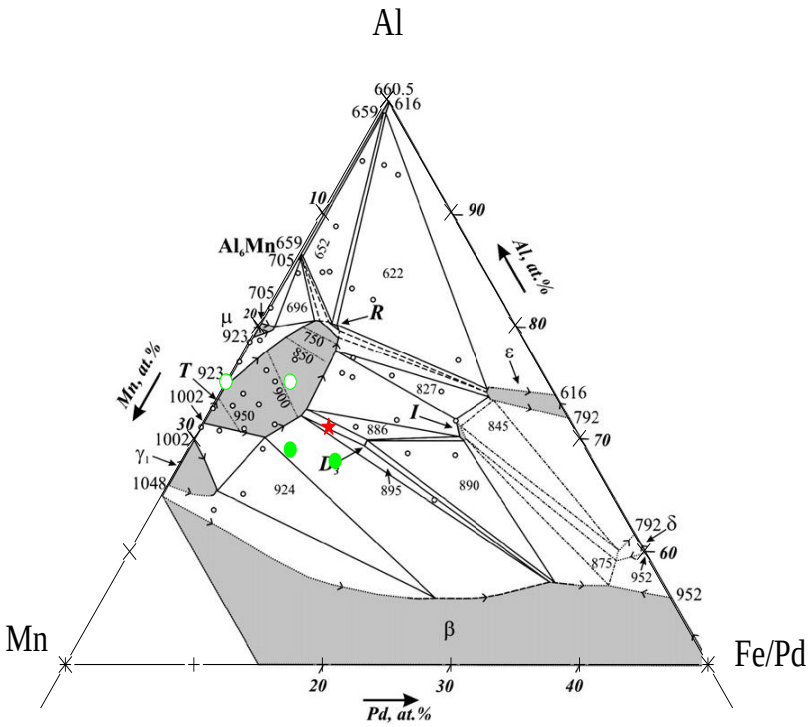


**Figure 4.3: Positions of the investigated samples in the phase diagram showing the projection of the solidus surface as determined by Balanetskyy *et al.* [1]. Single phase areas are marked in gray, numbers denote temperature in °C. AM and AMP open green dots, AMF8 and AMF12 full green dots, and decagonal AMF10 red star.**

The Taylor phase samples of our interest about which we discussed in the later chapters are $Al_{75}Mn_{25}$, $Al_{75}Mn_{20}Pd_5$ (green open symbols in figure 4.1) $Al_{69}Mn_{23}Fe_8$ and $Al_{68}Mn_{20}Fe_{12}$ (green full symbols), which are abbreviated as AM, AMP, AMF8 and

AMF12 respectively. Preparation and structural investigations were performed by Feuerbacher [4]. AM contains 75% Al and 25% Mn which gives precisely $Al_3Mn$. In the structure model of Klein *et al*. (1997) [3] for a sample containing 3.2 at% Pd all of these Pd-atoms are embedded only on one Al site and occupation of the other lattice sites is changed compared to the one of pure T- $Al_3Mn$ proposed by [5, 6]. Assumptions that this preferential substitution holds also for larger Pd content are highly speculative. For the Fe containing alloys the Al content is 69% and 68% for AMF8 and AMF12, respectively. Since these samples are single phase, the homogeneity region is in the case of Al-Mn-Fe more extended into the ternary region than for the Al-Mn-Pd system (shown in figure 4.1). In the structural model of Hiraga *et al.* [5] it is assumed that the sites Mn 5, 6, 8, 9 and Al 6 are occupied by both Al and Mn (see table 2.1 and discussion in chapter 2). It seems to be reasonable that only these occupation numbers are simultaneously changed (by 0.919 and 0.906 for AMF8 and AMF12, respectively) to take into account the varying Al content and that the occupation of the other sites remains unchanged. In accepting this, one can further assume that Fe is embedded only on Mn sites which will help to understand the Mössbauer results (chapter 6).

The decagonal sample on which we did our measurements was $Al_{71}Mn_{19}Fe_{10}$ (red star in figure 4.1). In this alloy the Al content is 71 at%. The sample is abbreviated as AMF10. Preparation and structural characterization was again done by [4]. Some of the sites are not fully occupied by both Al and Mn (see discussion in chapter 2). So Fe can in principle be embedded on both the Al or the Mn places. However, taking into account the Mössbauer results, it is highly probable that in the decagonal compound too Fe substitutes only Mn.

## 4.1 References

[1] S. Balanetskyy, G. Meisterernst, M. Heggen and M. Feuerbacher *Intermetallics* **16** (2008), 71-87.
[2] V. Raghavan *Journal of Phase Equilibria and Diffusion* **30** (2009), 71-76.
[3] H. Klein, M. Boudard, M. Audier, M. De Boissieu, H. Vincent, L. Beraha and M. Duneau *Phil. Mag. Lett.* **75** (1997), 197-208.
[4] M. Feuerbacher private communication.
[5] K. Hiraga, M. Kaneko, Y. Matsuo and S. Hashimoto *Phil. Mag. B*, **67** (1993), 193-205.
[6] V.V. Pavlyuk, T.I. Yanson and O.I. Bodak *Acta Cryst. C* **51** (1995), 792-794.

# 5. Magnetic measurements

## 5.1 Experimental

All DC magnetic measurements were performed by means of a 9 T vibrating sample magnetometer (VSM) of Quantum Design Physical Property Measurement System (PPMS) with vibrating frequency 40 Hz and amplitude 2 mm.

The basic principle of operation for a VSM is that a changing magnetic flux induces a voltage in a pickup coil. The time-dependent induced voltage is given by.

$$V_{coil} \propto \frac{d\Phi}{dt} \tag{5.1}$$

$$V_{coil} = \left(\frac{d\Phi}{dz}\right)\left(\frac{dz}{dt}\right) \tag{5.2}$$

In above equation Φ is the magnetic flux enclosed by the pickup coil, *z* is the vertical position of the sample with respect to the coil centre, and *t* is time. For a (dot shaped) sample sinusoidally oscillating along the centre of the pickup coil, the voltage is based on the following equation

$$V_{coil} = 2\pi f C m A \sin(2\pi f t) \tag{5.3}$$

with *C* the coupling constant, *m* the magnetic moment of the sample, *A* the amplitude of oscillation, and *f* the frequency of oscillation.

The sample is attached to the end of the sample rod that is driven sinusoidally. The centre of the oscillation is positioned at the vertical centre of the gradiometer pickup coils. The precise position and amplitude of oscillation is controlled from the VSM motor module using an optical linear encoder signal feedback from the VSM motor. The voltage induced in the pickup coils is amplified and lock-in detected in the VSM detection module. The position encoder signal is used as reference for the synchronous detection and the in-phase and the quadrature signals are recorded. These signals are averaged and sent over the CAN bus to the VSM application running on the PC [1].

### 5.1.1 Determination of freezing temperature

To determine the freezing temperature ($T_f$), the specimens were mounted in a standard brass sample holder and fixed with two quartz cylinders. After installing the sample was cooled from room temperature to 2 K in zero magnetic field. No wait time for thermal equilibration was passed before the respective magnetic field was applied and recording of the data starts immediately after reaching both the respective field value and 2 K. The zero field cooled measurements (ZFC) were performed point wise up to room temperature, with a temperature sweep rate of ~1 K/min and an increment of 0.5 K below $T_f$. Above $T_f$ the sweep rate was ~3 K/min and the increment 10 K. The temperature was then decreased under the same conditions to record the field cooled (FC) curve. The temperature $T_f$ was determined from the cusp in ZFC measurement.

### 5.1.2 Magnetic measurements

The samples were brought to the measuring temperature from above $T_f$ in zero magnetic field. Magnetic susceptibility was determined from temperature scans in fixed external fields (persistent mode).

The time dependence of the magnetic moment was recorded in the interval between 2 K and temperatures close to $T_f$ in external fields of 0.5 T, 1 T, and 2 T after zero field cooling from temperatures $T_0$ above the freezing temperature. The wait time before applying the respective field was 10 min to allow thermal equilibration. Immediately after reaching the respective field the measurement was started. Relaxation was recorded for 1 hour. Temperature stability for this time interval was usually better than ± 0.1 K for 2 K and ± 0.6 K for higher temperatures. To stabilize temperatures below 8 K in total waiting times of approximately one half hour were necessary during which the sample temperature changes in undefined manner. To determine the creep rate from the slope of moment versus ln(t) representations the typical time to be omitted at the beginning was ln(t/1s) = 5 (i.e. $t_0$ = 148.1 s). At this time the magnetization used for normalization ($M_0$) was taken. Within measuring accuracy no influence of the choice of $T_0$ (60 to 300 K) could be found, as long as $T_0 > 2\ T_f$.

## 5.2. Effective moments

As discussed in chapter 4 five different samples were prepared for this investigation. With the exception of AMF10 all samples show the T-$Al_3Mn$ structure, where Pd and Fe occupy 8d and 4c sites. AMF10 crystallizes as decagonal quasicrystal.

For calculating Curie constant $C$ (emu K/mole), Curie-Weiss temperature $\theta_c$ (K), and average magnetic moment per magnetic atom $\mu_{eff}$ ($\mu_B$) we should consider the susceptibility measurements as shown in figure 5.1 and 5.2 for Mn and Mn-Pd samples AM and AMP, and in figure 5.3 for Mn-Fe compounds AMF8, AMF10 and AMF12.

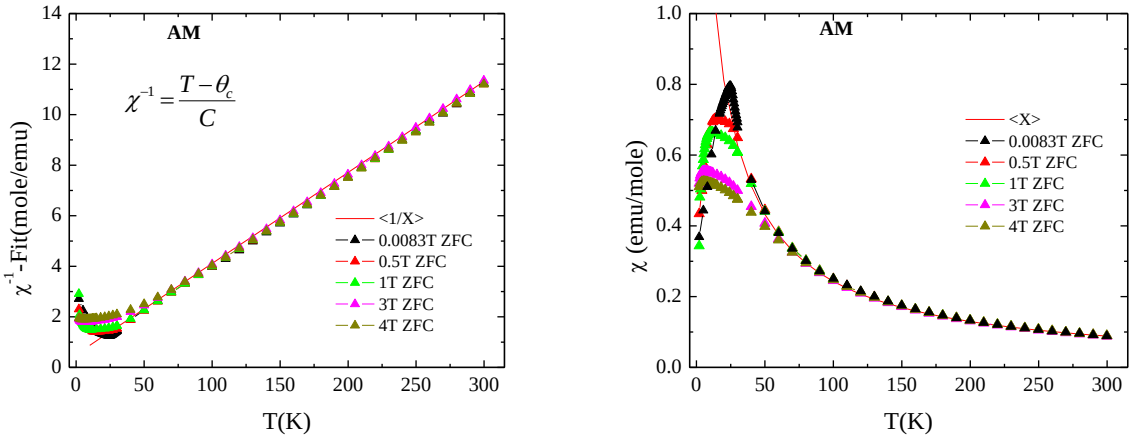


**Figure 5.1: Inverse susceptibility and susceptibility for $Al_{75}Mn_{25}$. Red line: mean of fits of measurements at the mentioned different external fields according to a Curie-Weiss law.**

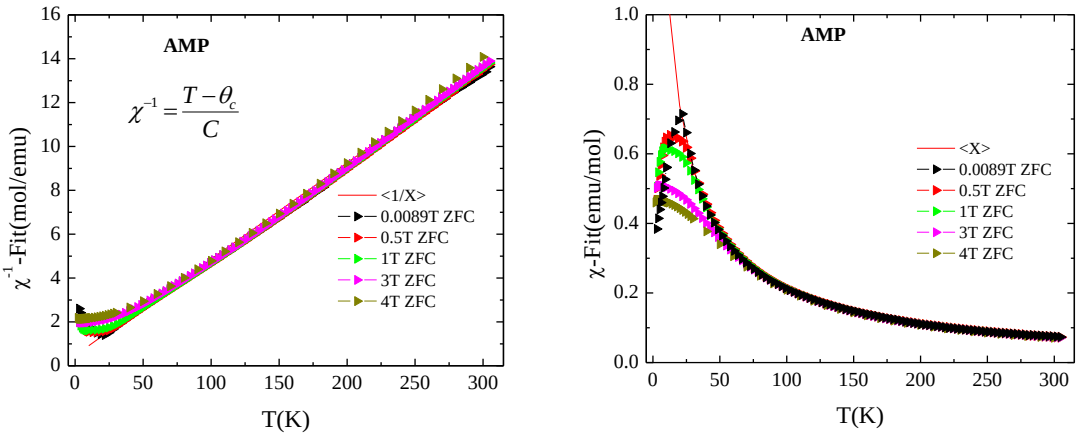


**Figure 5.2: Inverse susceptibility and susceptibility for the Pd containing sample AMP. Red line: mean of fits of measurements at the mentioned different external fields according to a Curie-Weiss law.**

We selected 5 different external fields between approximately 0.001 T and 4 T to make the measurements reliable. The entities discussed in the following are the means obtained from the measurements in these fields. For AM and AMP samples $C$ and $\theta_c$ values were calculated by using the Curie Weiss law.

$$\chi^{-1} = \frac{T-\theta_c}{C} \tag{5.4}$$

The values are given in and table 5.1. Since in the temperature interval 150 K to 250 K for all compounds some very small (perhaps systematic) deviations are present between fitting and measurements which were sometimes better visible in χ(T) representations the latter diagrams are also shown in figures 5.1, 5.2 and 5.3. For the iron containing samples the extended Curie-Weiss law was used to take into account the larger curvature of χ(T) compared to the un-substituted and the Pd containing compound.

$$\chi = \chi_0 + \frac{C}{T-\theta_c} \tag{5.5}$$

The resulting values for $\chi_0$, given in figure 5.3, are in the order of 3 $10^{-3}$ emu/mole (when we take the formula unit for the calculation of mole as done by [2]). In comparison -2.3 $10^{-3}$ emu/mole was reported for icosahedral $Al_{70}Mn_9Pd_{21}$ [3] and 6 $10^{-2}$ to 1 $10^{-4}$ emu/mole were obtained for binary Al-Mn quasicrystals with Mn content around 20 at% using the above definition for mole. This large spread in $\chi_0$ can be taken as an indication for a strong influence of sample preparation on this quantity.

Curie-Weiss temperatures for the un-substituted and the Pd containing sample are negative indicating a predominant antiferromagnetic coupling between atoms carrying a moment (figure 5.4). Whereas for the two un-substituted samples (one investigated by Dolinsek et al. [2], the other in the present investigation) with slightly different Al content approximately the same $\theta_c$ values were obtained, rather large differences appear for the Pd substituted compounds although all samples were prepared in similar way (table 2.1). In spite of the scatter in $\theta_c$ present for samples with low Fe content (table5.1, figure 5.4) generally $\theta_c$ increases with increasing Fe content and gets positive for

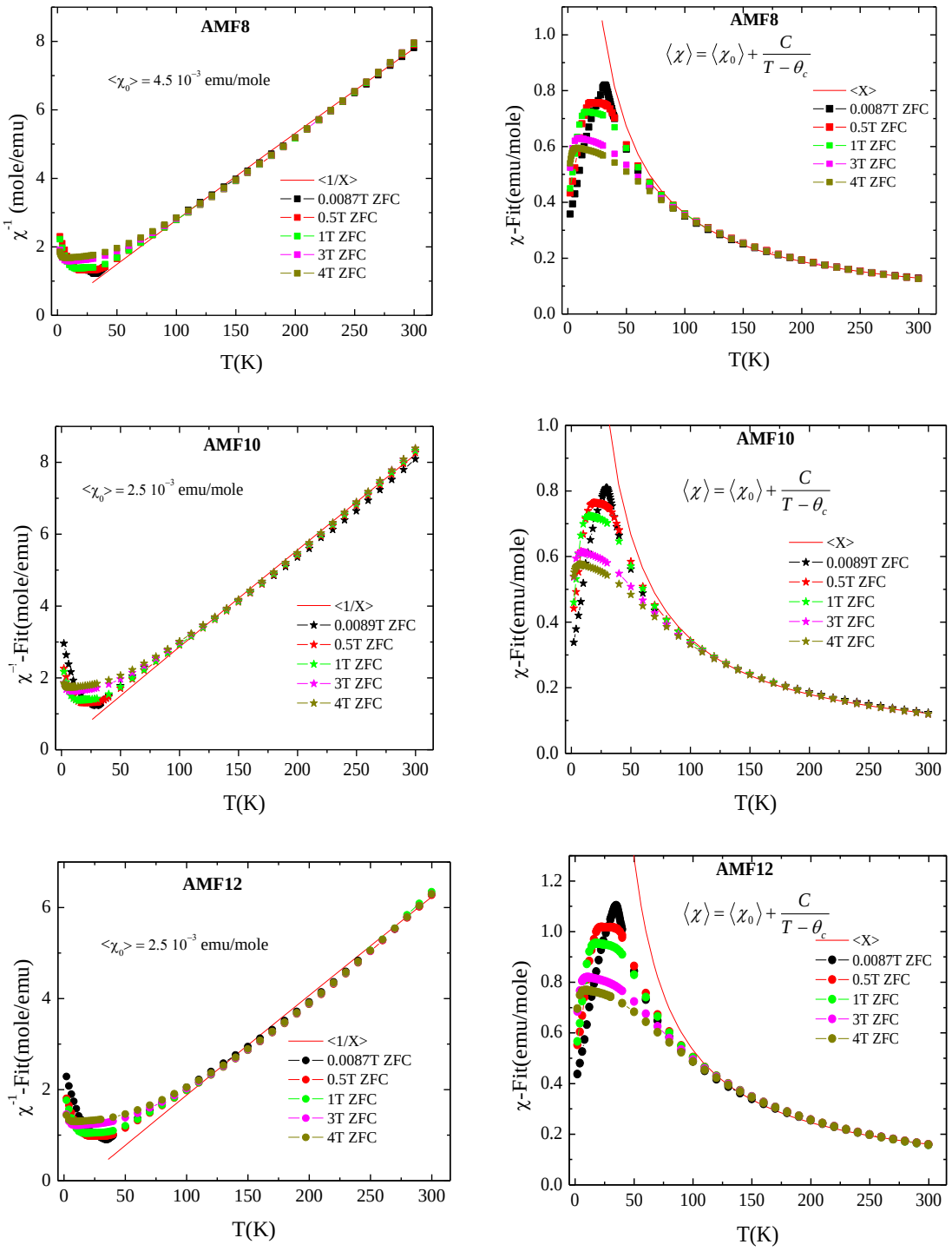


**Figure 5.3: Inverse susceptibility and susceptibility for the Fe containing samples AMF8, 10 and 12. Red line: mean of fits of measurements at the different mentioned external fields according to an extended Curie-Weiss law.**

AMF12, indicating a strong contribution of Fe to the magnetic exchange interaction. The effective moments were calculated from the Curie constants (figure 5.5, table 5.1) using.

$$\mu_{eff} = 2.83\sqrt{\frac{C}{x(Mn,Fe)}} \qquad (5.6)$$

**Table 5.1: Freezing temperature $T_f$, Curie constant $C$, Curie-Weiss temperature $\theta_c$, and average magnetic moment per magnetic atom $\mu_{eff}$ in comparison to the one reported by Dolinsek *et al.* [2] for samples prepared in the same way. In "sample column" black color show our samples and blue measured by [2]. Final values of magnetic moment for our samples are shown in green.**

| Sample/Abbriviation | $T_f$ | $C$ | $\theta_c$ | $\mu_{eff}$ Dolinsek *et al.* [2] | $\mu_{eff}$ moment on Mn, no moment on Pd/Fe | $\mu_{eff}$ moment on Mn and Pd/Fe |
|---|---|---|---|---|---|---|
| | (K) | (emuK/ mole) | (K) | ($\mu_B$) | ($\mu_B$) | ($\mu_B$) |
| **T-$Al_{75}Mn_{25}$ /T-AM** | 24.5 | 27.77 | -14.2 | | 2.98 | |
| **T-$Al_{73}Mn_{27}$ /T-AM** | 22.0 | 25.90 | -11.0 | 2.80 | 2.77 [a] | |
| **T-$Al_{73}Mn_{25}Pd_2$ /T-AMP2** | 24.7 | 22.00 | -32.0 | 2.70 | 2.65 [a] | 2.55 [a] |
| **T-$Al_{73}Mn_{23}Pd_4$ /T-AMP4** | 21.1 | 20.20 | -10.0 | 2.70 | 2.65 [a] | 2.45 [a] |
| **T-$Al_{75}Mn_{20}Pd_5$ /T-AMP5** | 22.0 | 22.79 | -10.9 | | 3.02 | 2.70 |
| **T-$Al_{73}Mn_{21}Pd_6$ /T-AMP6** | 16.2 | 18.10 | -23.0 | 2.60 | 2.63 [a] | 2.32 [a] |
| **T-$Al_{73}Mn_{25}Fe_2$ /T-AMF2** | 22.9 | 22.20 | -33.0 | 2.60 | 2.67 [a] | 2.57 [a] |
| **T-$Al_{73}Mn_{23}Fe_4$ /T-AMF4** | 23.3 | 22.60 | -37.0 | 2.70 | 2.81 [a] | 2.59 [a] |
| **D-$Al_{73}Mn_{21}Fe_6$ /D-AMF6** | 22.3 | 22.60 | -23.0 | 2.60 | 2.94 [a] | 2.59 [a] |
| **T-$Al_{69}Mn_{23}Fe_8$ /T-AMF8** | 32.0 | 38.00 | -7.0 | | 3.64 | 3.13 |
| **D-$Al_{71}Mn_{19}Fe_{10}$ /D-AMF10** | 29.5 | 36.30 | - 4.7 | | 3.91 | 3.17 |
| **T-$Al_{68}Mn_{20}Fe_{12}$ /T-AMF12** | 35.0 | 45.00 | 15.0 | | 4.25 | 3.36 |

[a] Calculated from C values reported by [2]

In agreement with literature on alloys with this Al content [4] we assumed that Pd carry no moment and take this into account in the calculations of $\mu_{eff}$. In contrast Fe was assumed to carry a moment. As first approximation the content of Mn and Fe was added and a mean $\mu_{eff}$ per transition metal atom, TM, was calculated (figure 5.6). For the two

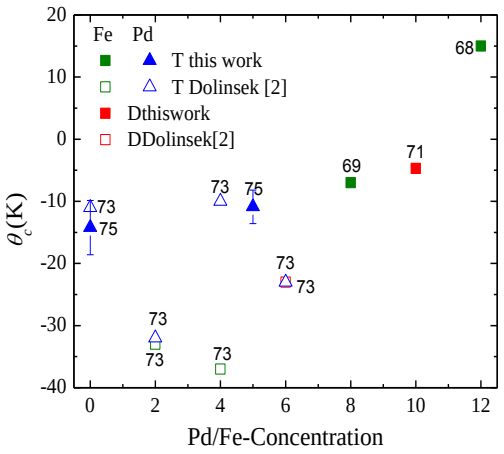


**Figure 5.4: Dependence of Curie-Weiss temperature $\theta_c$ for samples with different Al content (numbers close to symbols) and different structure (T…Taylor, D… decagonal) on the concentration of Pd/Fe.**

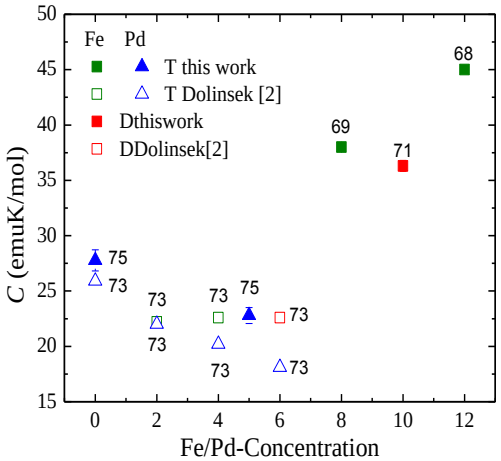


**Figure 5.5: Dependence of Curie constant $C$ for samples with different Al content (numbers close to symbols) and different structure (T… Taylor, D… decagonal) on the concentration of Pd/Fe.**

un-substituted compounds of the T-phase the one with the smaller Mn content has an approximately 7% higher effective moment. Generally an increase of $\mu_{eff}$ with Mn content is observed, which above 14 at% Mn does not depend very much on sample structure and preparation conditions (figure 5.7). For ternary alloys the dependence on Pd content seems to be more complicated.

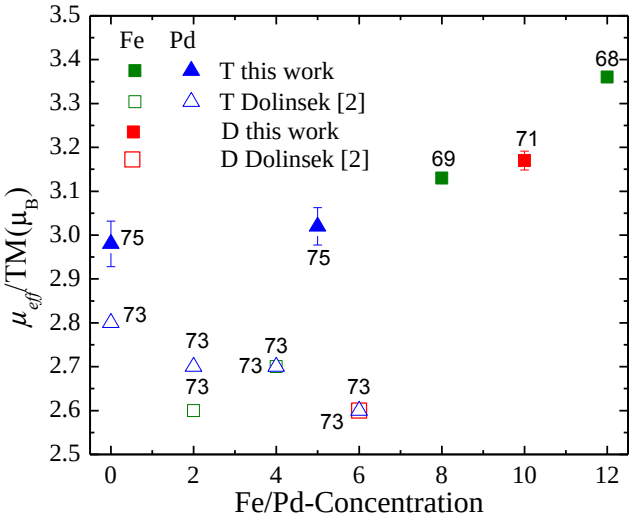


**Figure 5.6: Dependence of average magnetic moment per magnetic atom (TM) $\mu_{eff}(\mu_B)$ for Al-Mn-(Pd/Fe) samples with different Al content (numbers close to symbols) and different structure (T…Taylor, D… decagonal) on the concentration of Pd/Fe. Pd was assumed to carry no moment.**

Large scatter in $\mu_{eff}$ are observed e.g. for icosahedral quasicrystals prepared under different conditions (figure 5.8). In this context sample AMP also exhibits higher $\mu_{eff}$ compared to the similarly prepared samples investigated by [2]. For the Fe containing

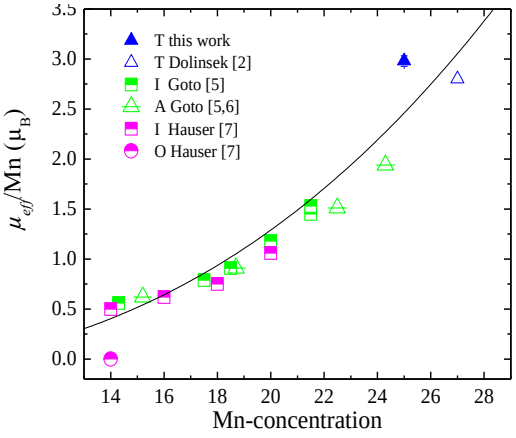


**Figure 5.7: Dependence of effective moment on Mn concentration derived from Curie Weiss fits for Al-Mn samples with different structures (T…Taylor, I…icosahedral, A… amorphous, O…orthorhombic) and prepared under different conditions. Line is only a guide for the eye.**

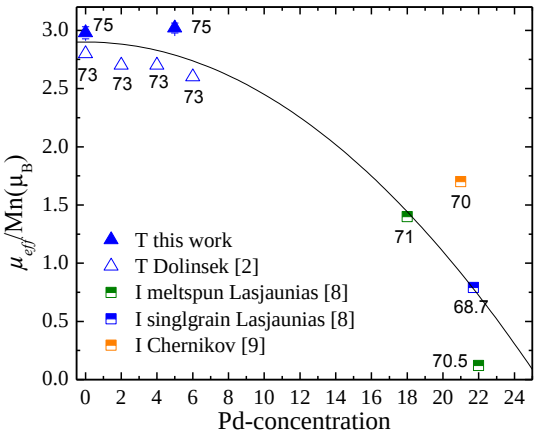


**Figure 5.8: Concentration dependence of effective moment per Mn atom derived under the assumption of zero moment on Pd for Al-Mn-Pd compounds with different structure (T… Taylor, I…icosahedral) and prepared under different conditions. Line is only a guide for the eye.**

compounds in agreement with [2] an increase of the effective moment per TM atom is observed with increase of Fe. For the decagonal compounds lower $\mu_{eff}$ values compared to the samples with T-phase are obtained.
The formation of magnetic moments on the Mn sites was investigated by *ab initio* calculations of the electronic and magnetic structure using a tight-binding linear-muffin-tin-orbital technique based on the local-spin-density approximation [9, 10]. Hybridization of Al-*p* and Mn-*d* states causes the appearance of a pseudo gap at the Fermi energy which suppresses the magnetic instability on a large number of the lattice sites. The fulfillment of local Stoner criteria ($n(E_F)I > 1$, with $n$ the local density of states and $I$ the intra-atomic exchange integral) which is supported by a high Mn-Mn coordination (present on some lattice positions, see Table 2.1, chapter 2) governs the appearance of the moment. In substitutionally disordered solutions the confinement of the atoms to fixed interatomic spacings reduces the hybridization and leads to an impurity like Mn local density of states (DOS). The pinning of the peak in the DOS at the Fermi level enhances the formation of a moment because of the half-filled Mn-band. In the idealized structural model for the Taylor phase the composition $Al_{79.5}Mn_{20.5}$ is realized, which is higher in Al content compared to the one used in the present study ($Al_{75}Mn_{25}$). In addition only seven different Mn sites are mentioned whereas according to the structural model of Hiraga [11] nine different Mn sites are present if the site Al(6) (see table 2.1, chapter 2) is neglected at which only 10% of the possible eight atoms are substituted by Mn. Hafner and Krajci [10] obtained from the self-consistent calculations moments for two of the seven sites of 1.0 $\mu_B$ and 0.66 $\mu_B$, and for the remaining other five values of 0.1 $\mu_B$ and below. Equally spread over the seven sites this would in mean result in a moment around 0.3 $\mu_B$, which would lead to $\mu_{eff} \sim 0.8\ \mu_B$ assuming g = 2. Experimentally $\mu_{eff} \sim 1.1\ \mu_B$ is found according to figure 5.7 for Mn content of 20.5 at% neglecting in the extrapolation all influences of the different chemical environments. Although slightly underestimating the value of the Mn moment these calculations give strong evidence for the presence of electronically different Mn sites which is in agreement with the results of Mössbauer investigations discussed in chapter 6.

## 5.3 Freezing temperatures

The temperature dependence of the susceptibility for the mentioned samples measured in an external field of approximately 10 mT is summarized for low temperatures in figure 5.9. Below approximately 50 K magnetic exchange interactions become dominant as indicated by the different values of the susceptibility derived from measurements in various fields (figure 5.10). For all samples irreversibility appear between ZFC and FC measurements below approximately 30 K. The peak in the ZFC curves gets rounded and shifts to lower temperature with increasing field (figure 5.10). Both dependencies are strong indications for spin glass behaviour.
Field dependence of the freezing temperature (defined as the maximum appearing in the ZFC magnetization) is summarized in figure 5.11. In the present investigations we only considered $T_f(B_a)$ for sample AM determined in fields up to 5 T, for AMP up to 4 T, and

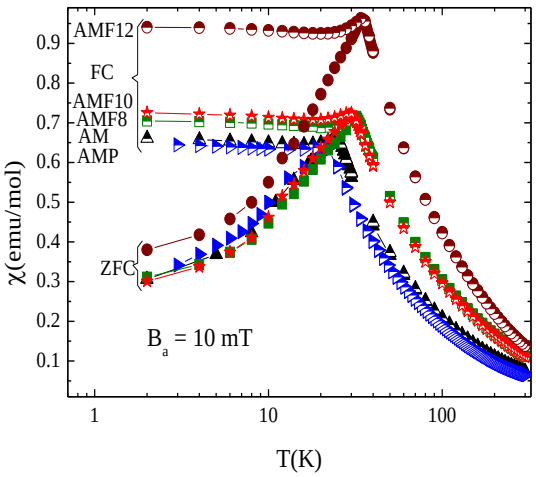


**Figure 5.9: Temperature dependence of ZFC (full) and FC (half open symbols) susceptibility for the five samples determined in external field of approximately 10 mT**.

for AMF8, 9 and 10 up to 8 T because these are the highest fields for which a maximum in the ZFC branch was ascertainable without fail. For higher fields the base temperature of the present investigations does not allow a determination of $T_f$. A fit for the field dependence of $T_f$ ($B_a$) for the different samples (figure 5.11) according to

$$T_f(B_a) = T_f(0) + b(B_a)^c \qquad (5.7)$$

leads to values for $c$ between 0.10 and 0.15 (figure 5.12). For Ising spins this parameter is calculated to be 0.66 (Thouless – d'Almeida line [12, 13]). For vector spin glasses it amounts 2 (Gabay - Toulouse line [14]) and taking into account anisotropy one ends up with values between 0.33 and 0.66 depending on the ratio of anisotropy to magnetic exchange energy [14]. All values are higher than the ones obtained from the present investigations. These discrepancies are often observed experimentally (e.g. [13]), but have, to the authors knowledge, not been explained satisfactorily up to now.

The typical shift of $T_f$ to higher temperatures with increasing measuring frequency was observed in ac-susceptibility investigations of [2, 14] for samples with composition $Al_{73}Mn_{27}$, $Al_{73}Mn_{23}Pd_4$ and $Al_{73}Mn_{21}Pd_6$. Although we could not repeat these measurements with our samples because of lack of experimental possibilities it is highly probable that similar frequency dependencies would appear. Thus together with the observed time dependence, which will be discussed below, spin glass behaviour characterizes the magnetic properties at low temperatures. Figure 5.13 gives an overview of the influence of the different Fe/Pd substitutions on $T_f$ in comparison with results obtained for other samples with Al content around 70 at% reported in literature. Taking into account the difference in the Al concentration (numbers close to the symbols) of the two sets of samples investigated by [2] and in the present work there are scatters in $T_f$ which are not in agreement with the Mn concentration dependence found for other samples of this area of the Al-Mn system (figure 5.14) and which are not explainable at present, e.g. for the border compounds the sample with larger Al content has a higher $T_f$, and similarly the sample with 2% Pd exhibit a higher $T_f$ compared to

that with 2% Fe. In general, however, $T_f$ decreases with substitution of nonmagnetic Pd, whereas the freezing temperature increases by substitution of magnetic Fe atoms.

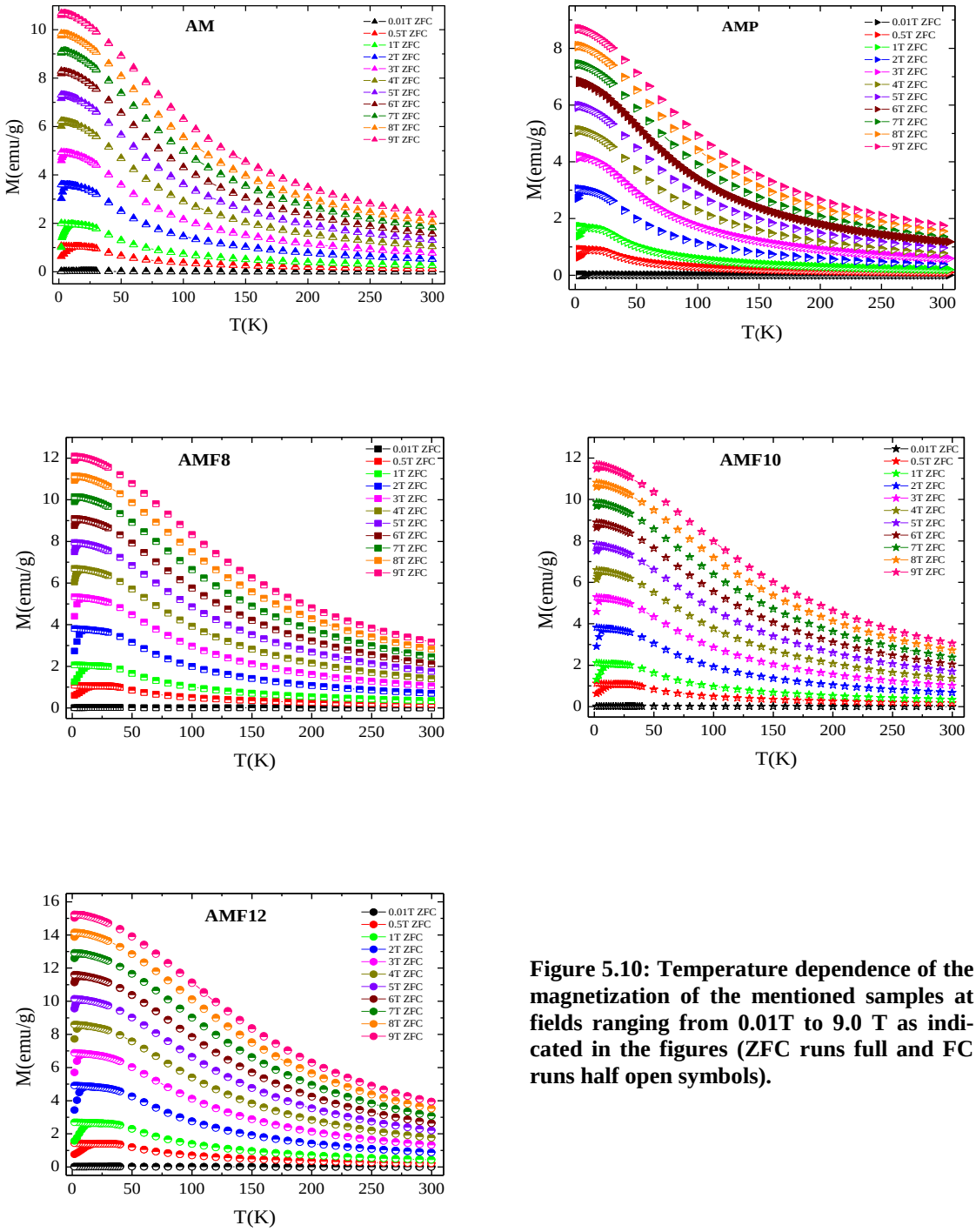


**Figure 5.10: Temperature dependence of the magnetization of the mentioned samples at fields ranging from 0.01T to 9.0 T as indicated in the figures (ZFC runs full and FC runs half open symbols).**

The samples showing the Taylor phase (2, 4, 8, and 12 at% Fe) have slightly higher $T_f$ values than the compounds forming as decagonal quasicrystal (6 and 10 at% Fe) [19].

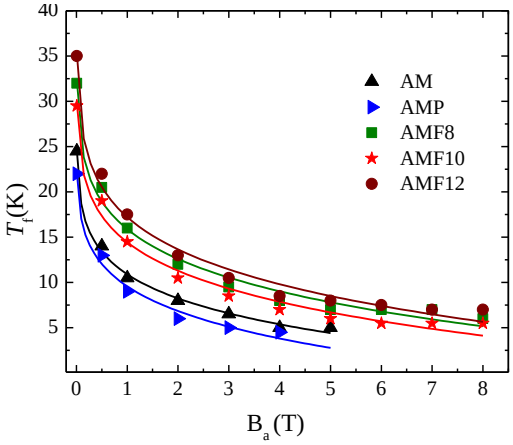


**Figure 5.11: Field dependence of the freezing temperature $T_f$ for the five measured samples. Lines are fits as described in the text.**

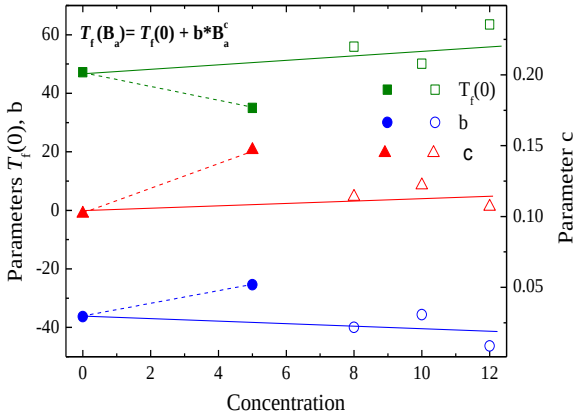


**Figure 5.12: $T_f(0)$, $b$ and $c$ obtained from fittings made for field dependence of freezing temperature $T_f$ of AM, AMP, AMF8, AMF10 and AMF12 samples. Dotted line connects data for Pd containing sample.**

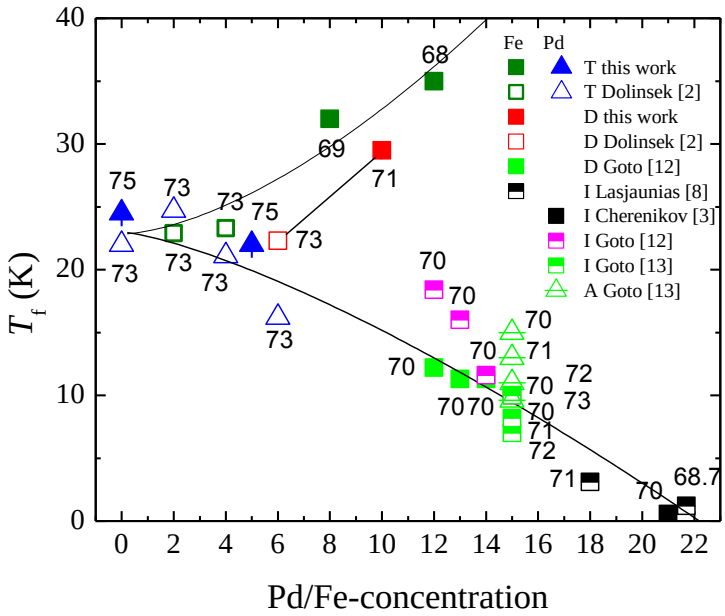


**Figure 5.13: Dependence of freezing temperatures of samples with Al content around 70 at% (numbers close to symbols) on the concentration of Pd/Fe. T…Taylor, D…decagonal, I… icosahedral, A…amorphous. Lines are only guide for the eye.**

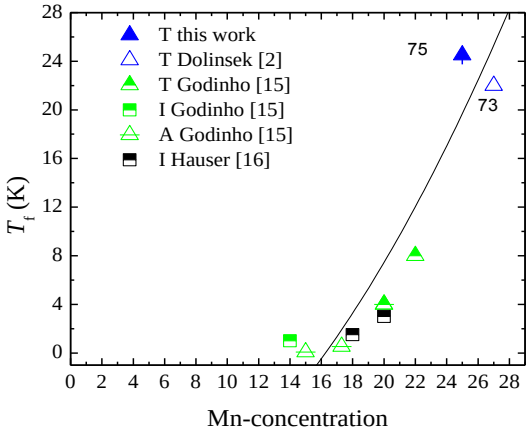


**Figure 5.14: Dependence of freezing temperatures $T_f$ derived for Al-Mn compounds with different structures (T…Taylor, I… icosahedral, A…amorphous) on Mn content. Line is only a guide for the eye.**

## 5.4 Time dependence of magnetisation

The time dependence of the magnetization was measured in the way mentioned in chapter 5.1.2 and exhibits for all samples within the chosen time interval a logarithmic

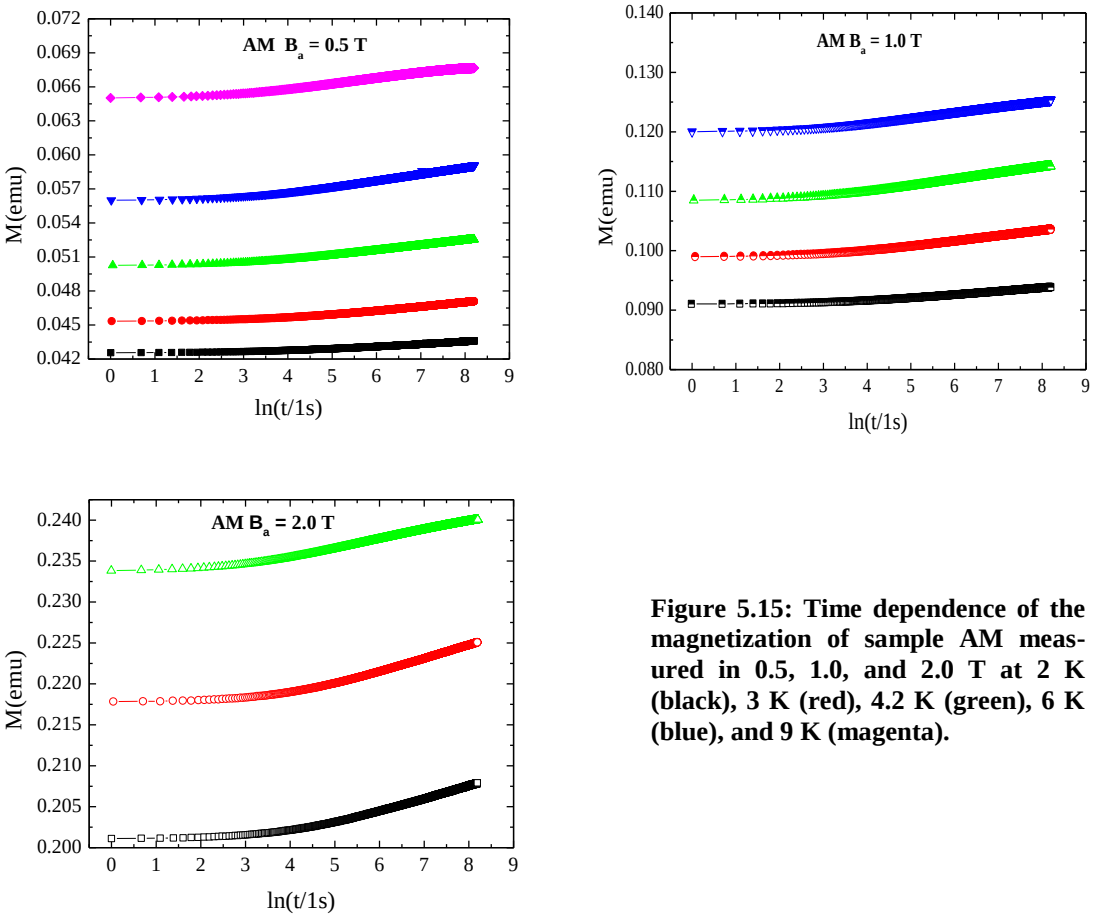


**Figure 5.15: Time dependence of the magnetization of sample AM measured in 0.5, 1.0, and 2.0 T at 2 K (black), 3 K (red), 4.2 K (green), 6 K (blue), and 9 K (magenta).**

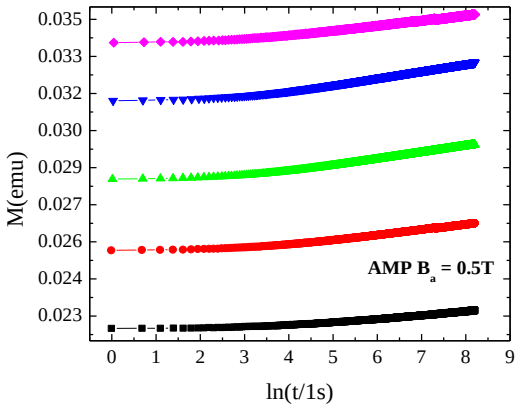


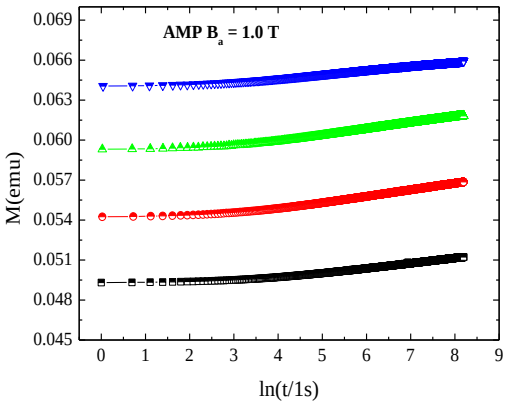


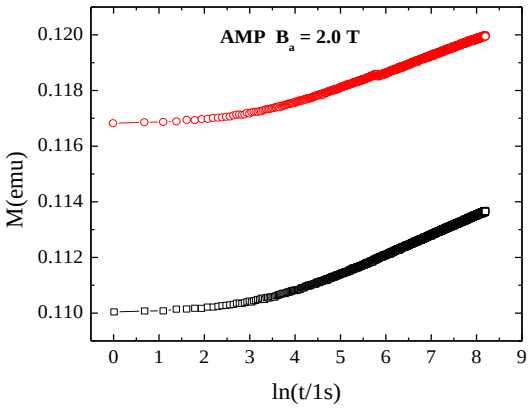


**Figure 5.16: Time dependence of the magnetization of sample AMP measured in 0.5, 1.0, and 2.0 T at 2 K (black), 3 K (red), 4.2 K (green), 6 K (blue), and 9 K (magenta).**

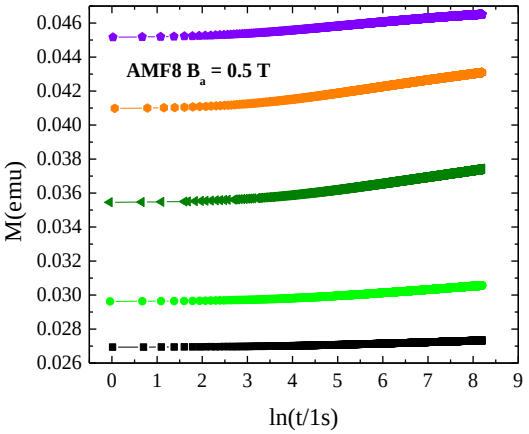


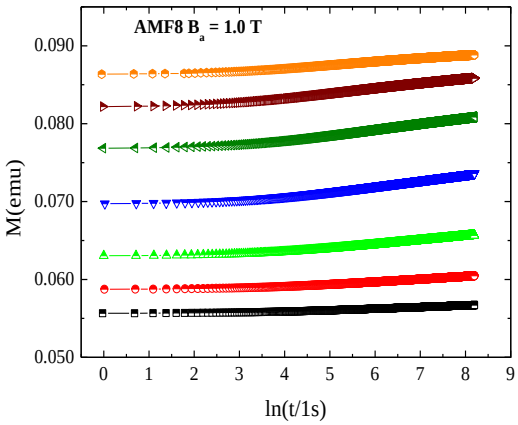


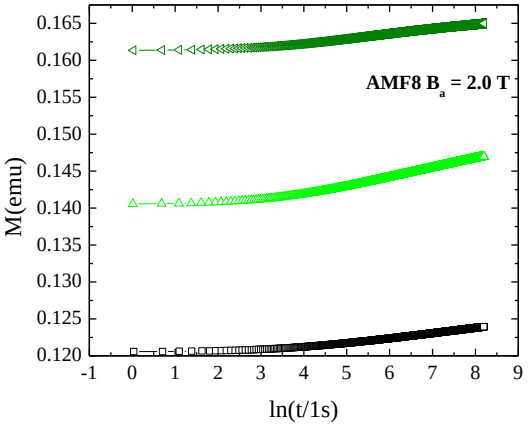


**Figure 5.17: Time dependence of the magnetization of sample AMF8 measured in 0.5, 1.0, and 2.0 T at 2 K (black), 3 K (red), 4.2 K (green), 6 K (blue), and 8 K (dark green), 10 K (dark brown), 12 K (orange), and 16 K (purple).**

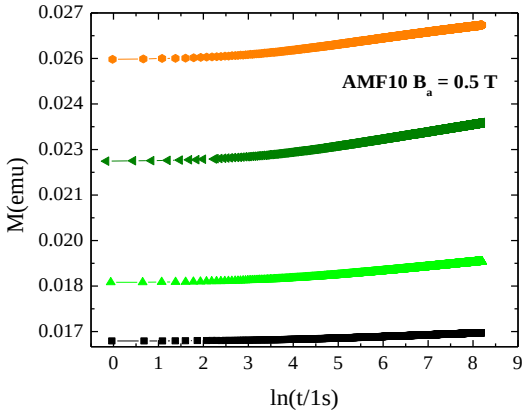


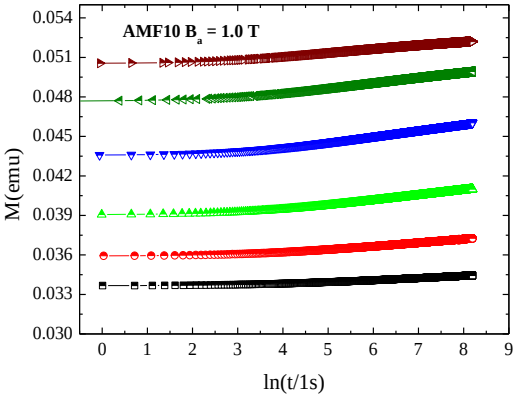


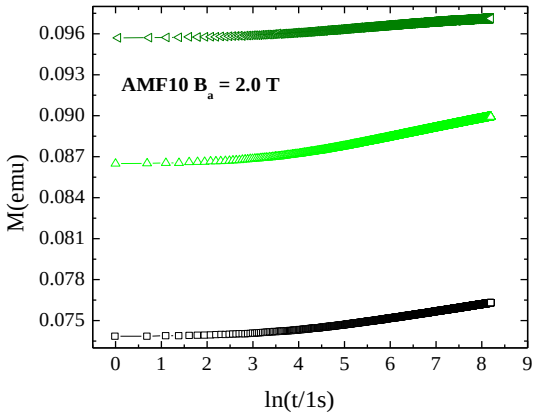


**Figure 5.18: Time dependence of the magnetization of sample AMF10 measured in 0.5, 1.0, and 2.0 T at 2 K (black), 3 K (red), 4.2 K (green), 6 K (blue), and 8 K (dark green), 10 K (dark brown), and 12 K (orange).**

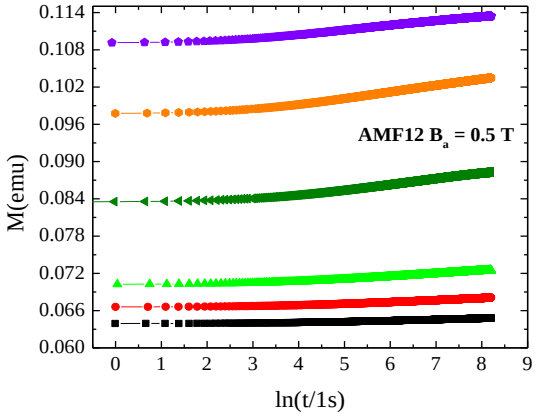


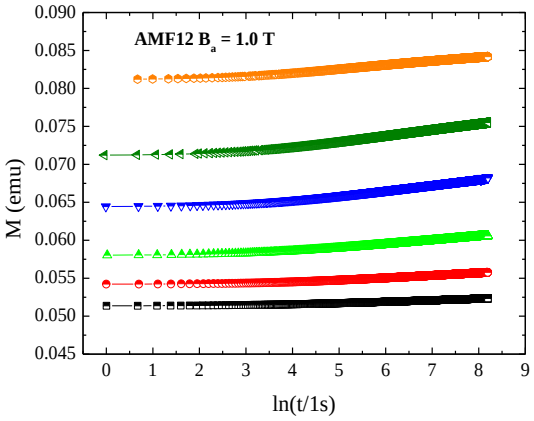


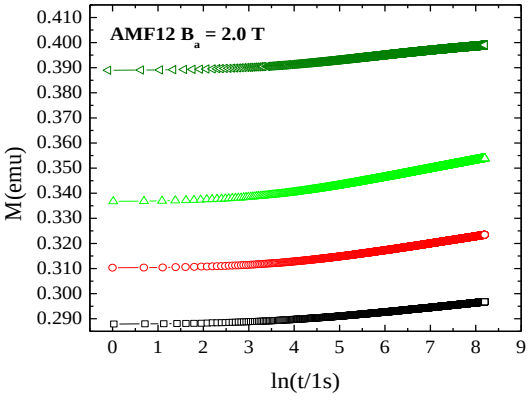


**Figure 5.19: Time dependence of the magnetization of sample AMF12 measured in 0.5, 1.0, and 2.0 T at 2 K (black), 3 K (red), 4.2 K (green), 6 K (blue), and 8 K (dark green), 10 K (dark brown), and 12 K (orange).**

behaviour (figures 5.15 to 5.19). Part of the results are already published in [19]. With increasing temperatures small deviations from this logarithmic behaviour are obtained. (e.g. data recorded at 9 K and 0.5 T in figure 5.15). Above $T_f$ no relaxation was observed within experimental resolution.

From the logarithmic behaviour the creep rate normalized to the magnetization at the starting time $t_0$ was determined (figure 5.20). Uncertainties due to aging are small, as the aging effects in this type of samples are found to be below 5% ([2] and discussion below). For all investigated samples $S$ shows strong temperature dependence with a maximum appearing at approximately $T_f/4$ for 0.5 T and much lower values for 2.0 T.

With increasing temperature the mean effective activation energy increases for all external fields 0.5 T, 1.0 T, and 2.0 T (figure 5.21). This is in contradiction to what is expected, as both the barriers which evolve with decreasing temperature should decrease and the time dependence of the magnetization should become stronger with increasing $T$. Interpreting, however, $E$ as the centre of gravity of an energy distribution this increase can be understood. For a given temperature, part of the relaxations on the low energy side of the distribution function does not contribute to the time dependence of the magnetization, because already having reached thermal equilibrium within the experimental time scale. This can be expressed by introducing a cut-off energy which shifts to higher values for higher temperatures, shifting also the centre of gravity to higher energies. The steepness of the increase of $E(T)$ is a measure of the width of the energy distribution. Increase of the applied field reduces the effective barrier height,

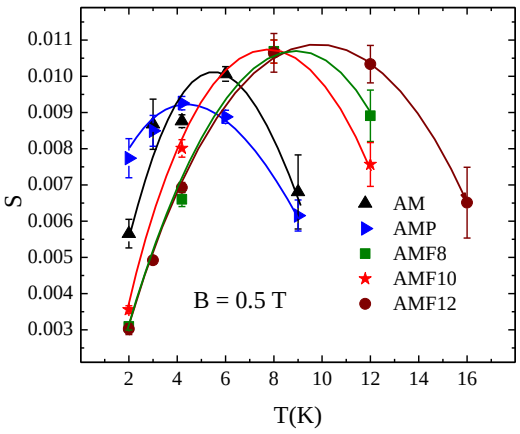


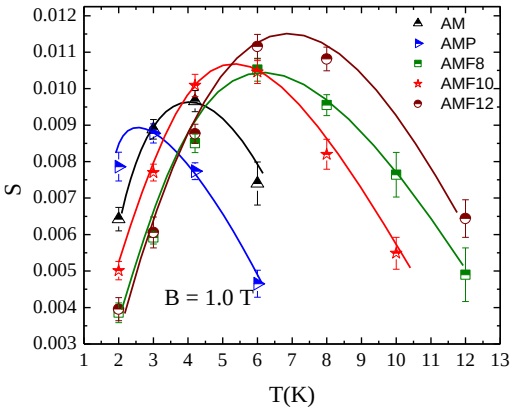


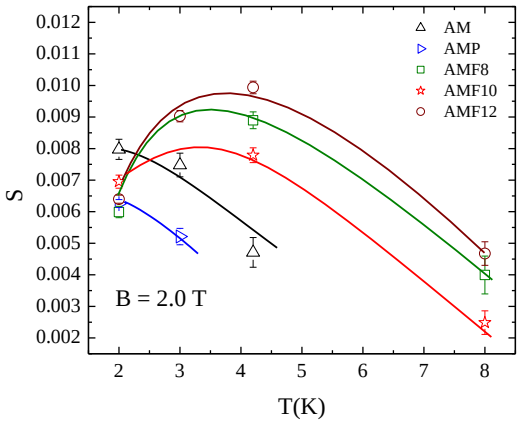


**Figure 5.20: Temperature dependence of creep rate $S$ of the mentioned different samples measured at 0.5 T, 1.0 T, and 2.0 T. Lines are only guide for the eye.**

leading to smaller $E$ values. The appearance of similar temperature dependences of $E$ (the results for 0.5 T are once again summarized in figure 5.22) points to similar shapes of the barrier distributions for the different samples, although differences of the absolute values are present. Small values are found for samples AM and AMP which amongst themselves show no difference within the measuring accuracy. Higher values are found for the Fe-substituted samples, with negligible differences for 8 and 12% Fe, but lower values for the decagonal quasicrystal AMF10. An interpretation of the time dependence within a classical droplet model allows an interpretation of $E$ in terms of magnetic

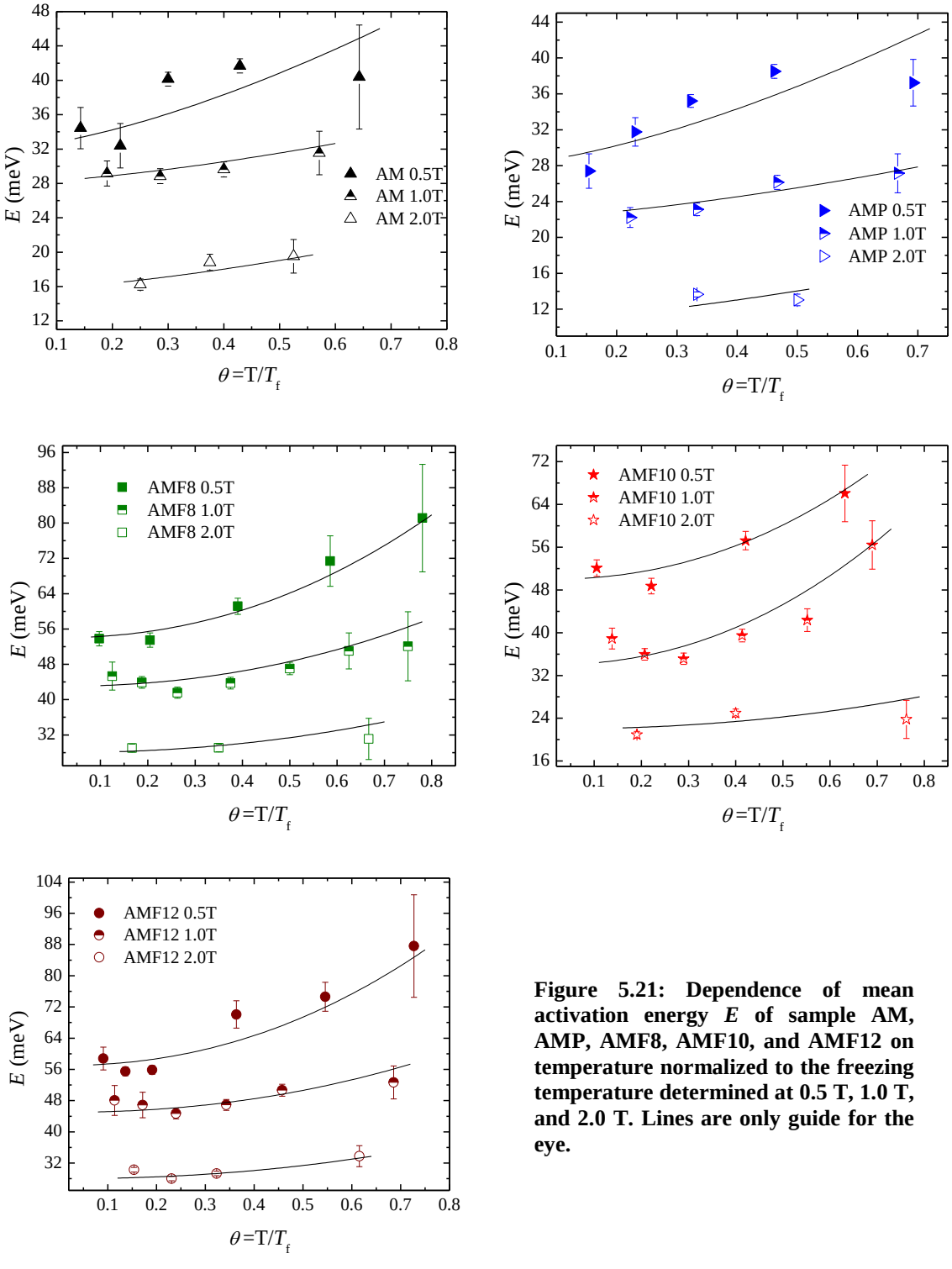


**Figure 5.21: Dependence of mean activation energy $E$ of sample AM, AMP, AMF8, AMF10, and AMF12 on temperature normalized to the freezing temperature determined at 0.5 T, 1.0 T, and 2.0 T. Lines are only guide for the eye.**

cluster sizes. In that sense the magnetic entities rotating in the external field are larger in the Fe-substituted than in the Pd- and the unsubstituted sample, which is not unexpected as Fe increases magnetic coupling. Although the T-phase is an approximant of the decagonal quasicrystal – that means that the structural building blocks are very similar – the intrinsic energy landscape is clearly different. It is surprising that the barriers are higher in the T-phase, although the over-all symmetry is lower in the decagonal phase.

In summary, the relaxation measurements point to broad distributions of activation energies. Although the shape of these distributions is very similar for the investigated samples, the centre of gravity is different. Higher values are obtained for the Fe containing compounds, indicating, that magnetic correlations are stronger.

For further information on the dynamics below $T_f$ the influence of different waiting times at zero field (the residual field present in the superconducting coil after a certain field-run is in the order of 0.1 mT in the used equipment) on the subsequently determined ZFC (measuring field 10 mT) magnetization was investigated (figure 5.23).

Similar, but much more extended experiments were also performed on $Al_{73}Mn_{27}$, $Al_{73}Mn_{23}Pd_4$ and D $Al_{73}Mn_{21}Fe_6$ by Dolinsek *et al.* [2]. To remind these samples are prepared under the same conditions but have slightly different Al content. In the present measurements the following (compared to [2] slightly modified) one stop protocols are used: The sample was cooled in zero field from 300 K to 15 K (below the spin glass transition temperature) and kept at this temperature for a certain time (1 min up to 3 hours) without changing the field conditions in the equipment. Afterwards, cool down was continued to 8 K still in zero field (lower temperature were not possible because of experimental conditions for cool-down). In contrast to all other experiments the usual waiting time for thermal equilibration was skipped and the measuring field of 10 mT was applied instantaneously. Warm-up was started immediately after reaching the field keeping the value of the field constant (as in usual ZFC measurements). No influence of waiting time is visible in magnetization at this temperature (cooling the sample further has led to rejuvenation, that means after the negative temperature step the system behaves as if it had been quenched from above $T_f$ without any interrupt). Around the

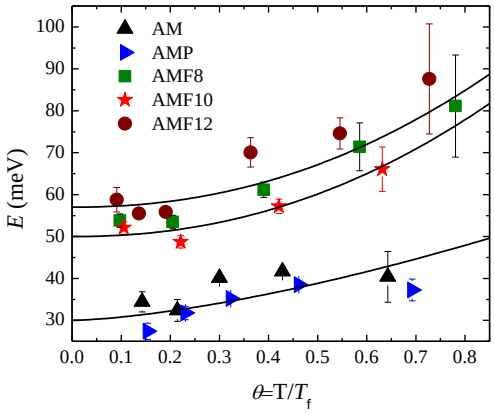


**Figure 5.22: Temperature dependence of the mean barrier height *E* obtained at 0.5 T for the investigated samples. The lines are guide for the eye.**

temperature of the waiting time in zero field (in this experiments 15 K) deviations of the magnetization from the values recorded without any waiting time in the cooling process appeared (the sample exhibits memory of the wait) and disappeared again at higher temperatures (figure 5.23). In agreement with Dolinsek *et al.* [2] it is observed that (although the deviations increase with waiting time) the largest amount of the drop in magnetization appears at short times (figure 5.23 right bottom). To examine the influence of cooling rate, sample AM was re-measured with the same conditions as described above and with a cooling rate decreased by a factor of 100 keeping the other conditions unchanged (inset figure 5.24). The resulting differences between the measurements ME Ref1 (measured within the first run of experiments) and ME Ref2 (measured within the second run) reflects the repeatability of the experiments. Adding the difference in magnetization between these two measurements at 40 K (influences of cooling conditions should be of minor importance at this temperature above $T_f$) to the one of ME Ref1 the data called "ME Ref1 corrected" were obtained, which for all temperatures agree well with those of ME Ref2 (figure 5.24). Thus, although close to the accuracy of the present experiments, the observed influence of cooling rate on magnetization is reliable and indicate the non-equilibrium states passed through by varying the temperature.

In a series of experiments Dolinsek *et al.* [2] were able to show further that this memory effect on pre-treatment conditions in zero field (i) is present at various waiting temperatures below $T_f$, (ii) diminishes (appears) after positive (negative) temperature steps (in the order of 2 K) within the spin glass phase around the waiting temperature, and (iii) is restricted to the spin glass phase itself. They explained this behaviour by gradual freezing of the spin system on cooling and the formation of droplets of antiferromagnetically coupled spins which thermally equilibrate during the waiting time and are only slightly influenced by changes of small magnetic fields. The spin order within the droplets is in a more stable condition than the rest of the spin glass matrix and thus needs a higher temperature for a spin reversion in standard ZFC measurements. Thus at the waiting temperature a smaller magnetization is measured compared to the one observed in investigations without an interrupt in the cooling process. Although this empirical picture explains to a certain degree the observed memory effects, it lacks in describing why most of the droplet formation is already finished in a time interval of several minutes (figure 5.23).

The aging dynamics was studied in past extensively both experimentally and theoretically and papers discussed in the following are certainly only a very restricted excerpt with the aim to show that the description is still under discussion. The group at the University of Uppsala investigated or take part on investigations of archetypical spin glasses (first paper in 1986 [21], present one in 2010 [22]), super spin glasses [23, 24] and small particles [25]. Quite similar results as shown in figure 5.23 are given in [22, 26] for conventional spin glasses, indicating that the antiferromagnetic order in the present samples is not the essential driving mechanism for the observed memory and rejuvenation. By introducing a strong separation of time scales governing the dynamics at different length scales (which are determined by the temperature of the sample) Bouchaud *et al.* [27] tried to reconcile droplet description (in which the dominant excitations are coherent fluctuations on length scale $l$, and where the dynamics is

governed by thermal activation over barriers of height determined by a combination of *l* and the free-energy e.g. [28] and references herein) and hierarchical description (in which it is assumed that the large number of independent metastable states composing

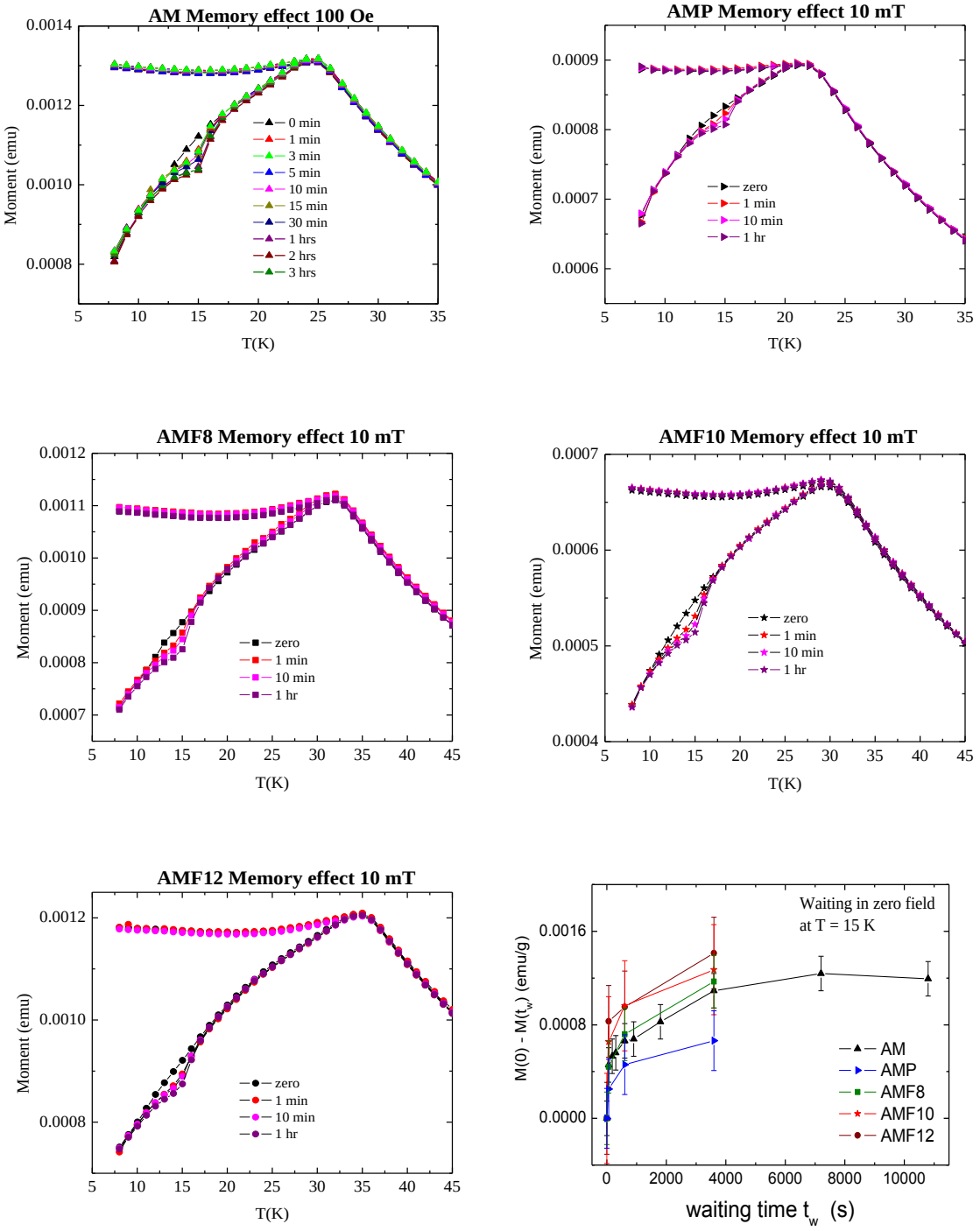


**Figure 5.23: Temperature dependence of magnetization of sample AM, AMP, AMF8, AMF10, and AMF12 recorded after the mentioned different waiting times in zero external fields at 15 K in ZFC worm-ups at 10 mT, which started at 8 K. Right hand bottom: Dependence of the difference between magnetization measured in 10 mT after zero waiting time M(0) and after a distinct waiting time $M(t_w)$ at 15 K on waiting time for sample AM, AMP, AMF8, AMF10, and AMF12. Lines are only connections of measuring points.**

spin glass state are organized in a hierarchical manner and wandering in the landscape formed by these states describes the dynamics e.g. [29] and references herein). Inherent in the model are vanishing free-energy barrier heights at $T_f$. The growing coherence length of an aging spin glass (predicted in the droplet model) gets in this computation broader validity in the sense that larger length scales needs longer time to evolve. Idealizing in neglecting the presence of an energy barrier distribution, for a given waiting time $t_{w1}$ at a certain temperature $T_1$ (below $T_f$) the aging dynamics is dominated by a characteristic length $l_1$. Larger length scales are frozen and smaller length scales are allowed to equilibrate. After a temperature reduction to $T_2$, because of the proposed strong separation of time scales, it is possible to freeze out the dynamics with $l_1$ (which will therefore keep the memory of the stay at $T_1$) and to select the one typical for $T_2$ with length scale $l_2$ which was equilibrated at $T_1$. The states have to appear according to their Boltzmann weights. In going from $T_1$ to $T_2$ these weights are changed and the system has to evolve towards a new state, even if the landscape of free-energy is not changed significantly (rejuvenation). The two main problems of this model are the independence of cooling rate and the restriction to a temperature dependent free-energy landscape (caused by the influence of the frozen larger length scale after temperature steps) which excludes simple two level descriptions. The first is in contradiction to the results of [30] and [31] as well as to the results shown in figure 5.24 agrees, however, with results of [32]. As discussed above, experimental situation does not allow a more precise contribution to this debate. Viddal and Roshko [33] argued against the second problem by showing that aging and memory are not restricted to collective freezing but are also observable in systems exhibiting irreversibility, hysteresis and progressive blocking during cooling. The correlated regimes may interact with each other, but relax independently over their own energy barrier. The model they proposed contains a free-energy landscape decomposed in an ensemble of one dimensional fragments, each with a double-well free-energy profile in a two state configuration. The numerical simulations of the temperature and time dependence of the magnetization for a system prepared under zero field cooled conditions including waiting times resembles the ones obtained for spin glasses completely and thus the ones shown in figure 5.23, too. A two level jump model was successfully used by [34] two describe the dynamics observed in high field Mössbauer and μSR experiments (which have much shorter characteristic time scales as the above discussed magnetization measurements) on classical spin glasses above their respective freezing temperatures. Lee and Young ([35] and references cited herein) were able to show that analogous to three-dimensional Ising spin glasses with short range interactions also vector spin glasses in three dimensions exhibit a phase transition at finite temperature. Based on this result (and using the value reported for $T_f$) Berthier and Young investigated the aging dynamics [36] and influence of temperature cycles [31] in three dimensional Heisenberg spin glasses for conditions which are similar to the experimental ones without external fields and were able to give a widely consistent explanation of aging, memory and rejuvanation. In their Monte Carlo calculation they used the Edwards-Anderson hamiltonian, a cubic lattice of $60^3$ sites and periodic boundary conditions. Since the system studied was large enough to overcome finite size effects (possibility of random walk of the overall spin direction

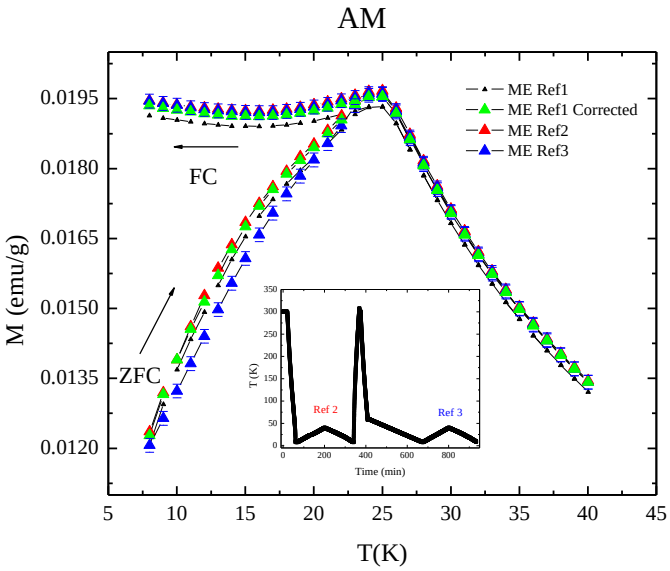


**Figure 5.24: Dependence of the magnetization on cooling rate for sample AM. Inset: Cooling rate and measuring time for runs ME Ref2 and ME Ref3.**

during the simulation without energy-cost), it was possible to show that, after a quench in temperature (from $T$ infinity) into the glassy state ($T < T_f$) and afterwards staying for a certain waiting time $t_w$ at constant $T$, physical quantities like susceptibility keep evolving with time as the system tries to reach equilibrium. The basic entity investigated for this conclusion was the correlation $C(r,t_w)$ of the relative orientation of two spins at distance $r$ and time $t_w$ to each other. At a given $T$ the decay of $C(r,t_w)$ with $r$ gets slower at large $t_w$, indicating the growth with time of a dynamical correlation or coherence length $l(T,t_w)$, which by itself strongly depends on $T$. For short distances $r$ compared to $l$ the spins were found to be in local equilibrium. Thus only the system as whole is not equilibrated and it is this increase in $l$ for large waiting times ("old" samples) which leads to a growth with time of a random (because of the quenched disorder characterising the spin glass phase) ordering (aging of the sample). They assumed that equilibration proceeds by activation over barriers of heights which are a function of $l$ and were able to show that for this Heisenberg spin glass, if it is quenched in a first step to $T_1 < T_f$ and kept there for a time $t_1$, the decay of the ac-susceptibility at the lower temperature $T_2$ is not a continuation of the decay at $T_1$ for the time interval $t_1 < t_w < t_1 + t_2$. The system forgot that it is "old", and seems to be "rejuvenated" by the temperature step. If the system temperature is changed after $t_w > t_1+t_2$ in a further step back to $T_1$ it behaves (after a short transient) as if the step to $T_2$ has not occurred. The system has kept a "memory" of the first aging step. Both effects, rejuvenation (although not observed to appear fully) and memory, are indications that changing the temperature leads only to modest changes in length scale but huge changes in time scale. Excitations of size $l_1$ are frozen at $T_2$. Dynamics at this temperature is due to excitations of smaller length scale $l_2$, which were already equilibrated at $T_1$ and aging is much less active at building spatial correlations. Finally it should be mentioned that in these investigations influences on the dynamics are observed caused by both cooling rate below and starting

conditions above $T_f$. Starting the quench to low temperature from above approximately $12.5 \cdot T_f$ has no influence on the dynamics. This is close to the observation of [34] who found dynamics up to temperatures approximately $10 \cdot T_f$.

To summarize this excerpt, within the constraint of the present experimental conditions (only dc-magnetization measurements could be performed, which always need the application of an external field) it seems that the concept of a coherence length which strongly depend on temperature and waiting time is able to describe the dynamics observed in the investigated samples.

## 5.5 References


[1] PPMS VSM Manual.

[2] J. Dolinsek, J. Slanovec, Z. Jaglicic, M. Heggen, S. Balanetskyy, M. Feuerbacher and K. Urban *Phys. Rev. B* **77** (2008), 064430 (18pp).

[3] M.A. Chernikov, A. Bernasconi, C. Beeli, A. Schilling and H. R. Ott *Phys. Rev. B* **48** (1986), 3058-3065.

[4] Z.M. Stadnik 1999 *Physical Properties of Quasicrystals* (Springer, New York).

[5] K. Fukamichi, T. Goto, T. Masumoto, T. Sakakibara, M. Oguchi and S. Todo *J. Phys. F: Met. Phys.* **17 (**1987), 743-752.

[6] K. Fukamichi and T. Goto *Sci. Rep. RITU, A* **36 (**1991), 143-157.

[7] J.J. Hauser, H.S. Chen and J.V. Waszczak *Phys. Rev. B* **33** (1986), 3577-3580.

[8] J.C. Lasjaunias, A. Sulpice, N. Keller, J.J. Prejean and M. de Boissieu *Phys. Rev. B* **52** (1995), 886-893.

[9] M. Krajci, J. Hafner and M. Mihalkovic *Phys. Rev. B* **55** (1997), 843 (13pp).

[10] J. Hafner, M. Krajci, *Phys. Rev. B* **57** (1998), 2849 (12pp).

[11] K. Hiraga, M. Kaneko, Y. Matsuo and S. Hashimoto *Phil. mag. B* **67** (1993), 193-205.

[12] J.R.L. de Almeida and D.J. Thouless *J. Phys. A: Math. Gen.* **11** (1978), 983-990.

[13] K.H. Fisher and J.A. Hertz 1986 *Spin Glasses* (Cambridge University Press, Cambridge).

[14] J. Slanovec, Z. Jagličic, M. Jagodić, M. Heggen, M. Feuerbacher, S. Balanetskyy and J. Dolinšek *Acta Physica Polonica A* **113** (2008), 19-22.

[15] M. Satoh, Y. Hattori, N. Kataoka, K. Fukamichi and T. Goto *Mat. Sci. and Eng. A***181-182 (**1994), 801-804.

[16] Y. Hattori, K. Fukamichi, H. Chikama, H. _Aruga-Katori and T. Goto *J. Phys.: Cond. Matter.* **6 (**1994), 10129-10140.

[17] M. Godinho, Cl. Berger, J.C. Lasjaunias, K. Hasselbach and O. Bethoux *Phys. Rev. B* **52** (1995), 808-811.

[18] J.J. Hauser, H.S. Chen and J.V. Waszczak *Phys. Rev. B* **33** (1986), 3577-3580.

[19] K. Ali, M. Reissner, M. Feuerbacher and W. Steiner *J. Phys. Conf. Series* **200** (2010), 032002 (4pp).

[20] J. Souletie *J. Physique* **41** (1983), 1095-1116.

[21] L. Lundgreen, P. Svendlindh, P. Nordblad and O. Beckman *Phys. Rev. Letters* **51** (1983), 911-914.

[22] R. Mathieu, M. Hudl, and P. Nordblad *J.Phys. Conf. Series* **200** (2010), 032042 (4pp).

[23] S. Sahoo, O. Petracic and W. Kleemann *Phys. Rev. B* **67** (2003), 214422 (4pp).

[24] S. Sahoo, O. Petracic, W. Kleemann, P. Nordblad, S. Cardoso and P.P. Freitas *J. of Mag. and Mag. Mater.* **272–276** (2004), 1316–1318.

[25] P. Nordblad *J. Phys. D: Appl. Phys.* **41** (2008), 134011 (4pp).

[26] R. Mathieu, P. Jönsson, D.N.H. Nam and P. Nordblad *Phys. Rev. B* **63** (2001), 092401(4pp).

[27] J.P. Bouchaud, V. Dupuis, J. Hammann and E. Vincent *Phys. Rev. B* **65** (2001), 024439 (11pp).

[28] J.O. Andersson, J. Mattsson and P. Svedlindh *Phys. Rev. B* **46** (1992), 8297-8304.
[29] L.F. Cugliandolo and J. Kurchan *Phys. Rev. B* **60** (1999), 922-930.
[30] G.F. Rodriguez, G.G. Kenning and R. Orbach *Phys. Rev. Lett.* **91** (2003), 037203 (4pp).
[31] L. Berthier and A.P. Young *Phys. Rev. B* **71** (2005), 214429 (14pp).
[32] D. Parker, F. Ladieu, J. Hammann and E. Vincent *Phys. Rev. B* **74** (2006), 184432 (9pp).
[33] C.A. Viddal and R.M. Roshko *Phys. Rev. B* **73** (2006), 172416 (4pp). C.A. Viddal and R.M. Roshko *J. Phys.: Condens. Matter* **17** (2005), 3343–3354. R.M. Roshko and C.A. Viddal *Physica B* **372** (2006) 68–71.
[34] J. Bogner, M. Reissner, W. Steiner, M.T.F Telling and R. Cywinski, *J. Magn. Magn. Mat.* **226** (2001), 1319-1320.
[35] L.W. Lee, A.P. Young *Phys. Rev. Letters* **90** (2003), 227203 (4pp).
[36] L. Berthier and A.P. Young *Phys. Rev. B* **69** (2004), 184423 (14pp).

# 6. Hyperfine interactions

## 6.1 Theoretical Background

For a nucleus embedded in a solid matrix a certain probability exists to emit a γ-quantum without recoil and without exiting a phonon in going from the first exited state to the ground state. The probability for this process is determined by the Lamb-Mössbauer factor. The equivalent probability exists for the same nucleus to absorb this γ-quantum in going from the ground to first exited state. Assuming that emission is independent for each nucleus it gets possible to detect γ-radiation with an energy uncertainty corresponding to the lifetime of the exited state of the respective nucleus. This is called recoilless gamma ray emission and absorption, now referred to as the "Mössbauer Effect". Energy shifts can be obtained by using a Doppler motion between source (where the emitting nuclei are placed) and absorber (where the absorbing nuclei are placed)

$$\hbar\omega = \hbar\omega_0 \left(1 - \frac{v}{c}\right) \tag{6.1}$$

($\hbar\omega_0$ energy difference between exited and ground state of the respective nucleus, $v$ velocity of the source, and $c$ velocity of light) [1]. For the present investigations transmission geometry was used. In this geometry the Doppler modulated γ-ray passes through the absorber and the counting rate behind the absorber is detected. In using the proper electronics and driving unit for the Doppler motion the velocity scans can be accumulated (Mössbauer spectra are recorded) and a so called line (minimum in counting rate) appears, the shape of which can be calculated by computer programs. The position is obtained from calibration measurements of the Doppler velocity.

The energies of the nuclear levels (in the present experiments $^{57}$Fe, ground state $I_g = 1/2$, exited state $I_a = 3/2$ ) are modified by their environment. This leads to shifts of the measured line position or the appearance of new lines in the spectra. The positions of these lines are proportional to the energy difference of the nuclear levels, and the line *intensities* are related to the angle between the gamma-ray and the nuclear spin moment. If the source material and the external conditions (temperature, external field) are kept constant information about the absorber material can be gained [1].

In expanding the potential build up by both the electrons of the atom which contains the above discussed nucleus and all electrons of the atoms of the environment which forms the solid matrix one ends up with two contributions to the electrostatic exchange energy: the isomer shift and the quadrupole interaction.

The isomer shift *IS* arises from the monopole (Coulomb) exchange interaction of the electron charge density at the nucleus and the non-zero volume of the nucleus. In the experiment this contribution is present from the source and the absorber and cannot be separated. Thus the line position is given by

$$IS = \frac{c}{\hbar\omega_0}\frac{2\pi}{3} Ze^2 \, \Delta < r^2 > [|\psi_S(0)|^2 - |\psi_A(0)|^2 ] \tag{6.2}$$

(with $Z$ atomic number, $e$ charge, $\Delta< r^2 >$ mean difference in nuclear radii between excited and ground state, $\psi$ electron wave function at the nucleus, $S$ source, and $A$ absorber) [1]. Since only $s$ electrons have a non-vanishing probability for presence at the nucleus, *IS* gives the difference in $s$ electron density between the source and the absorber. As the shift cannot be measured directly it is quoted relative to a known absorber (for the present experiments relative to the source $^{57}$Co**Rh**).
Generally, *IS* is superposed by the second order Doppler shift *SOD* which takes into account atomic vibrations caused by the temperature of the sample. The sum of the two terms is called center shift *CS*.

$$CS = IS + SOD \tag{6.3}$$

Assuming that in first approximation the phonon spectrum can be described by the Debye model, the temperature dependence of *SOD* can be related to the Debye temperature $\theta_D$ by

$$< SOD(T) > = -\frac{3k_B T}{2mc}\left(\frac{3\theta_D}{8T} + 3\left(\frac{T}{\theta_D}\right)^3 \int_0^{\theta_D/T} \frac{x^3}{e^x - 1} dx\right) \tag{6.4}$$

($m$ mass of the $^{57}$Fe nucleus, $k_B$ Boltzmann constant, and $x = \hbar\omega / kT$). In figure 6.8 the obtained values for the Debye temperature and the results following from the fits according to equation (6.4) are shown.
The second term of the above mentioned expansion of the potential takes into account charge distribution from electrons with zero probability of presence at nucleus For asymmetric electric fields generated by these charges the electric field gradient (EFG) tensor can be transformed to its principal axis. Nuclei with angular momentum quantum number $I > 1/2$ have a non-vanishing nuclear quadrupole moment. Exchange interaction between this moment and the EFG removes degeneracy leading to a splitting of the state and thus to the appearance of two lines with energy difference called quadrupole splitting *QS*. Introducing for EFG an asymmetry parameter defined as

$$\eta = \frac{V_{xx} - V_{yy}}{V_{zz}} \tag{6.5}$$

one gets the Hamiltonian which has to be solved for exited and ground state

$$\mathcal{H}_Q = \frac{eQ}{\hbar^2\, 4I(2I-1)}\left[3I_z^2 - I^2 + \frac{1}{2}\eta(I_+^2 + I_-^2)\right] \tag{6.6}$$

($Q$ nuclear quadrupole moment, $I$ angular momentum, in the bracket angular momentum operators).
In the case of an isotope with $I_a = 3/2$, such as $^{57}$Fe, this state is split into two substates $m_I = \pm 1/2$ and $m_I = \pm 3/2$. This is shown in figure 6.1, giving a two line spectrum or "doublet" [2].

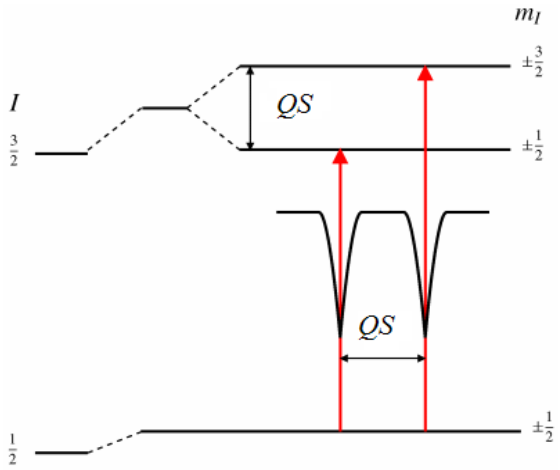


**Figure 6.1: Quadrupole splitting for a 3/2 to 1/2 transition. The magnitude $QS = 2\frac{eQV_{zz}}{4}$, $(\eta = 0)$ is shown. The spectrum for a powdered absorber is sketched [2].**

In the presence of a magnetic field the nuclear spin moment experiences a dipolar interaction with the magnetic field (Zeeman splitting). The total effective magnetic field at the nucleus, $B_{eff}$ is given by

$$\boldsymbol{B}_{eff} = (\boldsymbol{B}_{contact} + \boldsymbol{B}_{orbital} + \boldsymbol{B}_{dipolar}) + \boldsymbol{B}_{applied} \tag{6.7}$$

the first three terms being due to the atom's own partially filled electron shells. $B_{contact}$ is caused by the difference in spin up and down states of the electrons close to the nucleus (Fermi contact term), $B_{orbital}$ is due to the orbital moment of those electrons, and $B_{dipolar}$ is the dipolar field due to the spin of the electrons in the neighbourhood [1]. This magnetic field splits nuclear levels $I_N$ into $(2I_N+1)$ substates (N exited or ground state). The Hamiltonian to be solved for the exited and the ground state is

$$\mathcal{H}_M = -\frac{\mu_N}{\hbar\, I_N}\, \boldsymbol{I}\, \boldsymbol{B}_{eff} \tag{6.8}$$

($\mu_N$ nuclear moment of exited or ground state, respectively). The energy difference between exited and ground state gives the different line positions. The selection rule is determined by the kind of radiation (in case of $^{57}$Fe, magnetic dipolar, resulting in $\Delta m_I$ = 0, ± 1). This gives six different lines for a 3/2 to 1/2 transition neglecting quadrupole interaction. The line spacings being proportional to $B_{eff}$. The spectrum is sketched in figure 6.2.

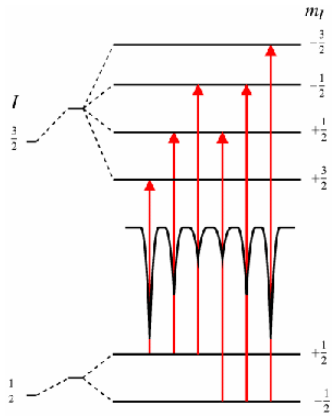

**Figure 6.2: Magnetic splitting of the nuclear energy levels for a field $B_{eff}$ and diminishing quadrupole splitting. The resulting spectrum for a powdered absorber is sketched [2].**

## 6.2 Experimental

All measurements were performed with a standard constant acceleration spectrometer in transmission geometry. The $^{57}$Co**Rh** source was mounted on the driving system and kept at room temperature. All *CS* data are given relative to this source. Calibration of velocity scale was performed with α-Fe foils. Line widths (full width at half maximum, FWHM) of the calibration spectra are typically 0.24 mm/s. For temperature variation between 4.3 K and room temperature a continuous flow cryostat was used in which the sample is kept in He-exchange gas. Temperature stability was ± 0.5 K at temperatures above 77 K and ± 0.2 K below. For the measurements the samples were crashed by hand by means of an agate mortar to a fine powder and afterwards sealed between two teflon foils. For analyses of the spectra a computer code was used by which the full Hamiltonian including electrostatic and magnetic hyperfine interaction is solved [3] and sample thickness is taken into account after [4].

## 6.3 Results

For the two crystalline samples the spectra recorded above the respective freezing temperature (examples are shown in figure 6.3 and 6.4) exhibit asymmetries with respect to line intensity and slope which does not allow an analyses with only one quadrupole split spectrum where the different Fe sites are simply taken into account by allowing line broadening. The same holds for the decagonal sample, although the difference in line intensity at 294 K is less pronounced (figure 6.5). To the best knowledge of the author no Mössbauer investigations on crystalline Taylor phases with Mn content around 25 at% are reported. Well investigated are icosahedral quasicrystals (*i*) with attempts to relate the results to various structure models. In contrast to the present investigations which show rather similar spectra for crystalline and quasicrystalline compounds, for *I*- $Al_6$(MnFe) the recorded spectrum exhibit broad lines and were analyzed by means of two quadrupole doublets with small differences in *CS* and large ones in *QS* pointing the presence of two different sites for the transition metal

atoms. In the crystalline compound only one spectrum was necessary for a proper analysis with values of *CS* and *QS* close to the one with the larger intensity in the quasicrystalline compound [5]. The presence of two kinds of Mn sites with a preferential substitution of Fe on the one which carry no moment was proposed for *I*-$Al_{74}Si_6(MnFe)_{20}$ [6]. This interpretation was heavily discussed and based on investiga-

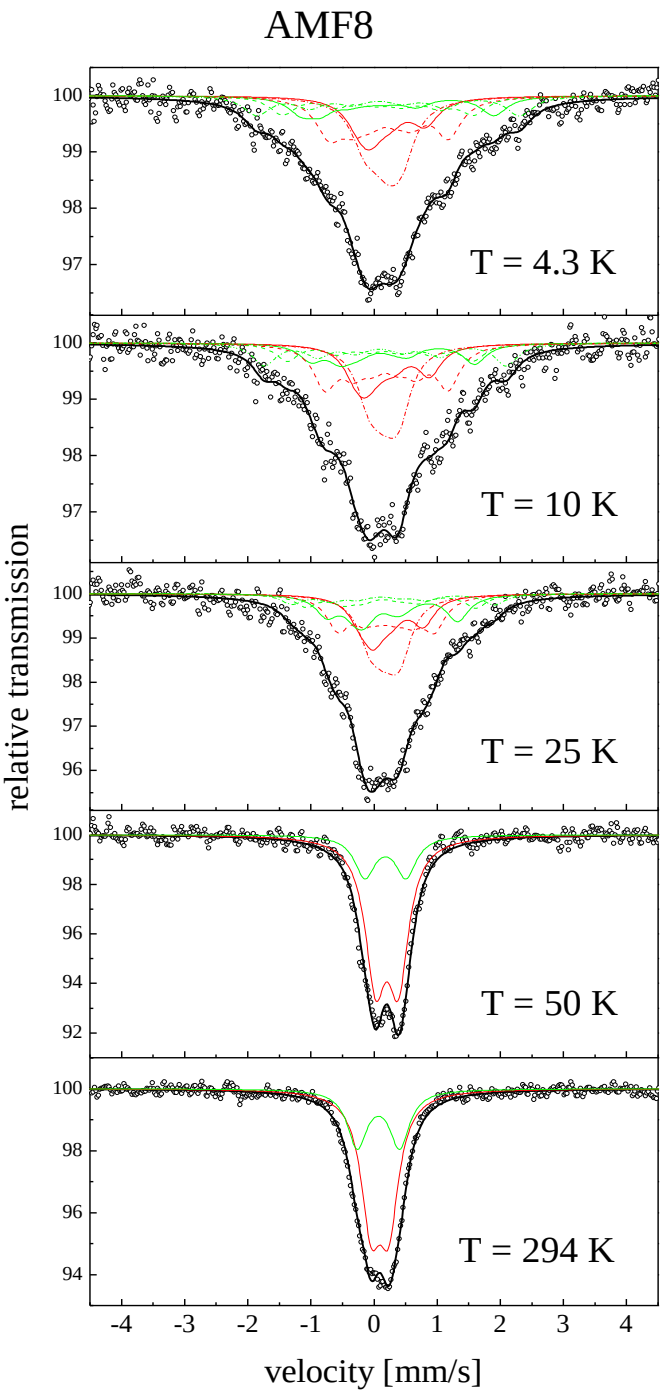


**Figure 6.3: $^{57}$Fe transmission spectra of the crystalline Taylor phase sample AMF8 at different temperatures. The subspectra used in the fit are indicated by red and green, the result of the least-square fit by black.**

tions of I-$Al_{86}Mn_{14}$ ($^{27}$Al and $^{55}$Mn NMR spectroscopy [7], $^{57}$Fe doped samples [8]), I-AlSiMn (isomorphically substituted by 28 at% Fe or by a mixture of 17 at% ($Cr_{0.5}Fe_{0.5}$) [9]), I-$Al_{80}Mn_{14.4}Fe_{5.6}$ [10], and I-AlCuFe alloys it is argued that the spectra are more reliably analyzed by a distribution of quadrupole splitting. To evaluate the distributions correlations between isomer shift and quadrupole splitting were introduced which are physically not *a priori* justified, but argued to be present in a more recent investigation [11]. The distribution of quadrupole splitting resembles a multiplicity of Fe-sites and

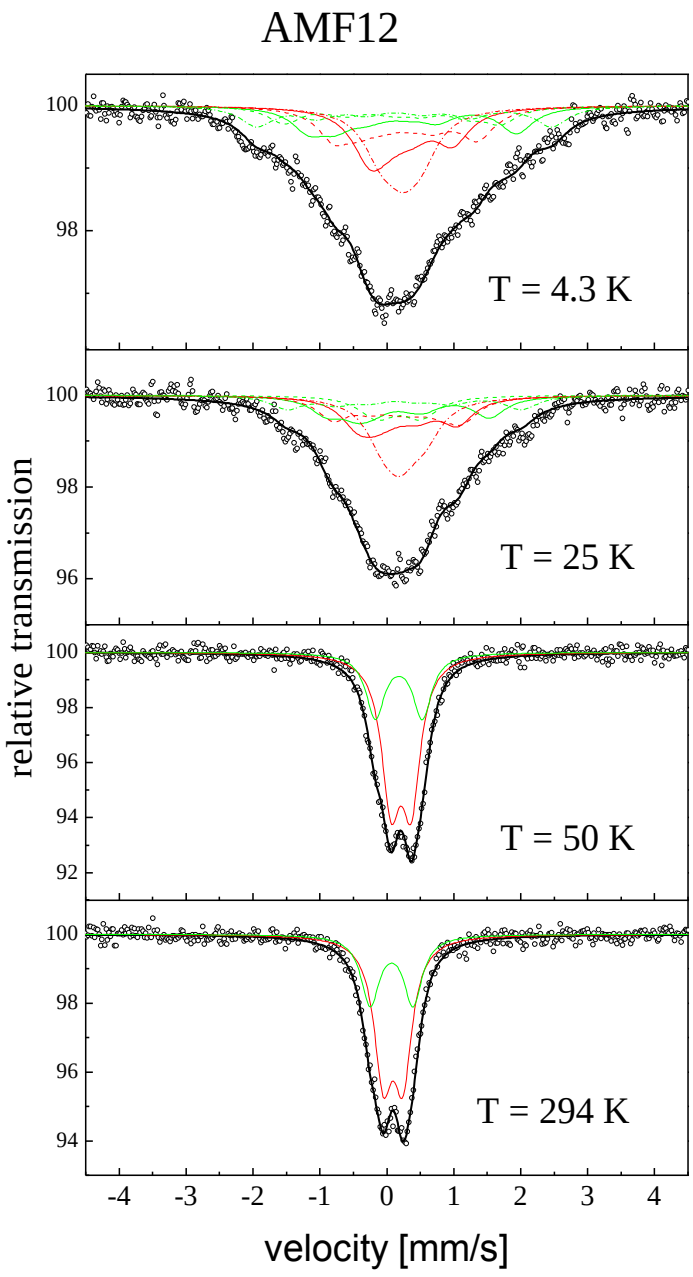


**Figure 6.4: $^{57}$Fe transmission spectra of the crystalline Taylor phase sample AMF12 at different temperatures. The subspectra used in the fit are indicated by red and green, the result of the least-square fit by black.**

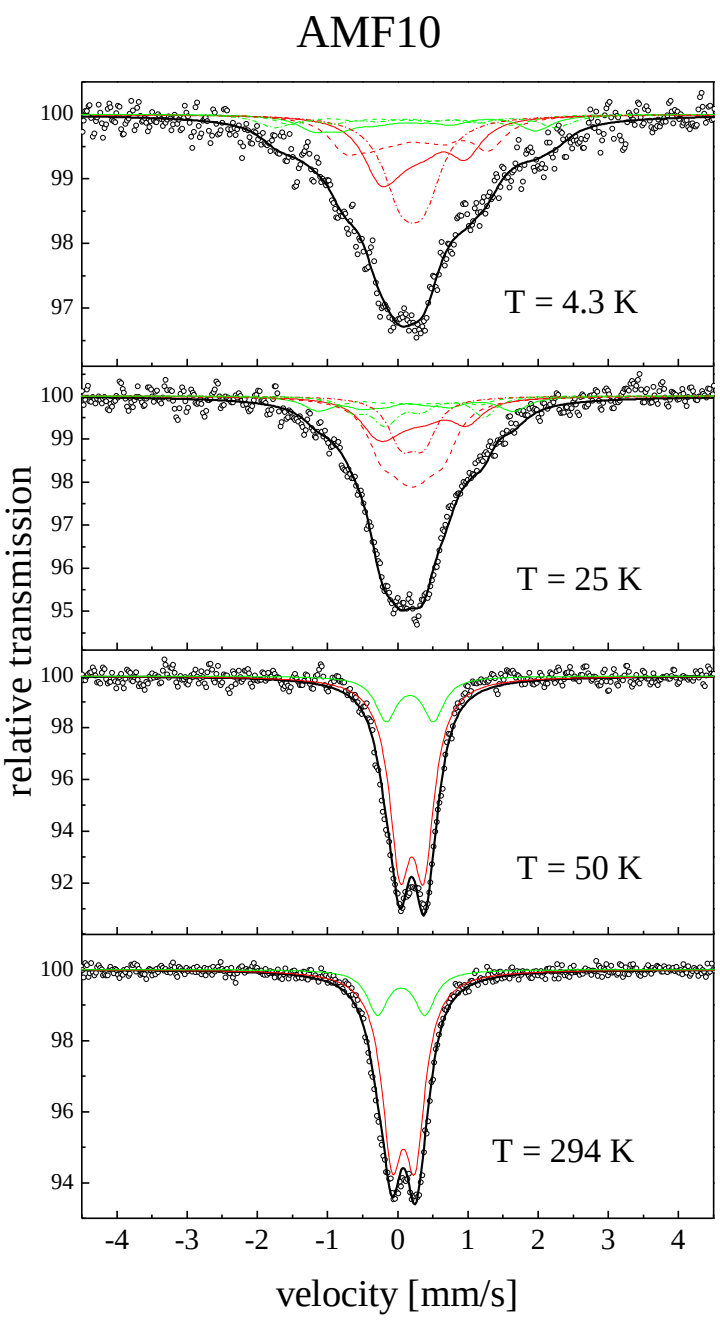


**Figure 6.5: $^{57}$Fe transmission spectra of the quasicrystalline decagonal sample AMF10 at different temperatures. The subspectra used in the fit are indicated by red and green, the result of the least-square fit by black.**

reflects an intrinsic disorder in the icosahedral structure [12-15]. A broad distribution of the value of the local electric field gradient tensor on the Al sites was also concluded from MNR and NQR investigations [16]. On the other hand for $Al_{65}Cu_{20+x}Fe_{15-x}$ systematic variations were found of both *CS* and *QS* for the wide concentration interval $-10 \leq x \leq 10$, whereas changes among the three structurally different states icosahedral, crystalline, and amorphous remain small [17]. These results are contrasted by investigations of the influence of mechanical grinding [18]. Not only for the un-milled

sample the spectrum differs from the one reported in [17], huge broadening is obtained after 200 hours grinding. Investigations along the stability boarder for Fe and Cu content of both the icosahedral structure and the rhombohedral 3/2 approximant exhibit only small changes of *CS* and *QS*, but significantly larger ones in crossing from one border to the other at constant concentration [11]. Preferential site occupancy was assumed for I-$Al_{86}Cr_{14-x}Fe_x$, $3 \leq x \leq 14$ [19] and a distribution of quadrupole splitting was used to analyze I-Ti-Mn-Fe-Si compounds [20].

Investigations on decagonal AlMn compounds focus on Al contents around 80 at%. A broad distribution for the electric field gradient and large similarities of the spectra to the icosahedral ones was observed by NMR measurements on $^{55}Mn$ [21]. The Mössbauer results are either analyzed by a superposition of two broadened quadrupole split spectra [22-24] or a quadrupole distribution assuming a linear correlation between quadrupole splitting and isomer shift [10]. Large differences were observed between the overall shape of the spectra of I-$Al_{65}Cu_{20}Fe_{15}$ and decagonal $Al_{65}(Co_{0.96}Fe_{0.04})_{20}Cu_{15}$ [23]. The spectrum of the latter compound is also different from the one of the present investigation (figure 6.5), whereas for decagonal compounds (without Mn, but Al content around 75 at%) $Al_{75}Pd_{15}Fe_{10}$ [25] and $Al_{75}Ni_9Fe_{16}$ [26] the shape of the spectra are similar to the one of AMF10. Since all analyses are based on structural considerations (decorations of Penrose tiling) of the quasicrystal in the following the attempt was made to start with the structural model of the crystalline compound and to transform the thus found fitting routine onto the quasicrystalline sample.

For the crystalline Taylor phase, the distances to the nearest neighbours are calculated for the different sites occupied by Mn using the program package "Crystallographica" Version 1.60a (table 6.1). The radius of the sphere around the source atom was determined by $1.05 \cdot (r(\mathrm{Al}) + r(\mathrm{Mn})) = 0.294$ nm, with $r(\mathrm{Al}) = 0.143$ nm, $r(\mathrm{Mn}) = 0.137$ nm (typical for metallic bonds), and choosing 1.05 as an arbitrary overlap factor. Within this sphere, which can be seen as the first neighbor shell, atoms on Mn1 and Mn7 positions have only Al atoms as nearest neighbours. For all other sites, both Mn and Al are present (table 6.1). It can be assumed that for these two positions, because of the strong Al-*p* Mn-*d* hybridization (see e.g. [27] and discussion herein) the charge density and distribution are different compared to the ones of the other sites for which both atom species are present in the first shell. Assuming (i) that Fe substitutes only Mn and not Al and (ii) that no preferential embedding of Fe on the different lattice sites is present (random distribution) two groups of subspectra with different isomer shift and quadrupole splitting can be expected. According to the occupation numbers given by Hiraga *et al.* [28] (see table 2.1, chapter 2) twelve atoms are on sites surrounded by Al only (four on Mn1 and 8 on Mn7) whereas (rounded) 28 atoms are on the other sites, leading to the (approximate) sample concentration $Al_{75}Mn_{25}$. From this numbers a ratio of 0.3:0.7 should be present for the relative intensities of the subspectra representative for these environments. The Taylor samples of the present investigations ($Al_{69}Mn_{23}Fe_8$ and $Al_{68}Mn_{20}Fe_{12}$) are lower in Al content which may cause (if assumptions (i) and (ii) are still valid) a change in this intensity ratio by approximately 8%. This value is, however, far within the measuring accuracy for alloys not enriched with $^{57}Fe$.

**Table 6.1: Interatomic distances within a sphere of 0.294 nm around the respective source atom for the different sites occupied by Mn in the Taylor phase following the structural refinements of Hiraga *et al.* and taking the thus reported lattice parameters a = 1.483 nm, b = 1.243 nm, c = 1.251 nm [28]. Lattice sites are numbered as in table 2.1, chapter 2. Partial occupation by both atomic species Al and Mn is denoted by "d".**

| source atom | target atom | distance (nm) | | source atom | target atom | distance (nm) |
|---|---|---|---|---|---|---|
| | | | | | | |
| Mn1 | Al14 | 0.238603 | | Mn2 | Al13 | 0.251403 |
| Mn1 | Al14 | 0.238603 | | Mn2 | Al13 | 0.251403 |
| Mn1 | Al15 | 0.238732 | | Mn2 | Al4 | 0.254413 |
| Mn1 | Al15 | 0.238732 | | Mn2 | Mn6d | 0.257768 |
| Mn1 | Al9 | 0.247303 | | Mn2 | Al3 | 0.257796 |
| Mn1 | Al9 | 0.247303 | | Mn2 | Al10 | 0.260290 |
| Mn1 | Al2 | 0.248926 | | Mn2 | Al10 | 0.260290 |
| Mn1 | Al3 | 0.250652 | | Mn2 | Al7 | 0.262867 |
| Mn1 | Al1 | 0.253682 | | Mn2 | Al7 | 0.262867 |
| | | | | Mn2 | Mn5d | 0.274366 |
| | | | | Mn2 | Mn9d | 0.283391 |
| | | | | Mn2 | Mn9d | 0.283391 |
| | | | | | | |
| Mn3 | Al12 | 0.243986 | | Mn4 | Al11 | 0.247714 |
| Mn3 | Al12 | 0.243986 | | Mn4 | Al11 | 0.247714 |
| Mn3 | Al4 | 0.257707 | | Mn4 | Al2 | 0.258897 |
| Mn3 | Al10 | 0.263809 | | Mn4 | Al10 | 0.259610 |
| Mn3 | Al10 | 0.263809 | | Mn4 | Al10 | 0.259610 |
| Mn3 | Mn5d | 0.264504 | | Mn4 | Al1 | 0.262279 |
| Mn3 | Al1 | 0.265066 | | Mn4 | Mn3 | 0.269777 |
| Mn3 | Mn4 | 0.269777 | | Mn4 | Mn6d | 0.270081 |
| Mn3 | Al6 | 0.271041 | | Mn4 | Al8 | 0.271473 |
| Mn3 | Al6 | 0.271041 | | Mn4 | Al8 | 0.271473 |
| Mn3 | Al8 | 0.275604 | | Mn4 | Mn8d | 0.281172 |
| Mn3 | Al8 | 0.275604 | | Mn4 | Mn8d | 0.281172 |
| | | | | | | |
| Mn5d | Al16d | 0.253746 | | Mn6d | Al16d | 0.253325 |
| Mn5d | Al16d | 0.253746 | | Mn6d | Al16d | 0.253325 |
| Mn5d | Al10 | 0.260799 | | Mn6d | Mn2 | 0.257768 |
| Mn5d | Al10 | 0.260799 | | Mn6d | Al10 | 0.258812 |
| Mn5d | Al3 | 0.263139 | | Mn6d | Al10 | 0.258812 |
| Mn5d | Al4 | 0.264460 | | Mn6d | Al2 | 0.260917 |
| Mn5d | Mn3 | 0.264504 | | Mn6d | Al4 | 0.268226 |
| Mn5d | Al6 | 0.273510 | | Mn6d | Mn4 | 0.270081 |
| Mn5d | Al6 | 0.273510 | | Mn6d | Al7 | 0.273662 |
| Mn5d | Mn2 | 0.274366 | | Mn6d | Al7 | 0.273662 |
| Mn5d | Mn9d | 0.276890 | | Mn6d | Mn8d | 0.276905 |
| Mn5d | Mn9d | 0.276890 | | Mn6d | Mn8d | 0.276905 |
| | | | | | | |
| Mn7 | Al5 | 0.239836 | | Mn8d | Al16d | 0.259828 |
| Mn7 | Al12 | 0.249805 | | Mn8d | Al10 | 0.268689 |
| Mn7 | Al15 | 0.249868 | | Mn8d | Al11 | 0.268694 |
| Mn7 | Al14 | 0.250059 | | Mn8d | Al13 | 0.270865 |
| Mn7 | Al13 | 0.251568 | | Mn8d | Mn6d | 0.276905 |
| Mn7 | Al10 | 0.254341 | | Mn8d | Al15 | 0.279499 |
| Mn7 | Al11 | 0.255899 | | Mn8d | Mn4 | 0.281172 |
| Mn7 | Al6 | 0.285222 | | Mn8d | Al2 | 0.282889 |
| Mn7 | Al7 | 0.287665 | | Mn8d | Al7 | 0.290775 |
| Mn7 | Al8 | 0.288254 | | Mn8d | Al8 | 0.292440 |
| | | | | | | |

| | | | | | | |
|---|---|---|---|---|---|---|
| Mn9d | Al16d | 0.257401 | | Al6d | Al10 | 0.266201 |
| Mn9d | Al11 | 0.270968 | | Al6d | Al12 | 0.270986 |
| Mn9d | Al10 | 0.272616 | | Al6d | Mn3 | 0.271041 |
| Mn9d | Al14 | 0.273886 | | Al6d | Al16d | 0.271631 |
| Mn9d | Al13 | 0.274459 | | Al6d | Mn5d | 0.273510 |
| Mn9d | Mn5d | 0.276890 | | Al6d | Al14 | 0.274686 |
| Mn9d | Al3 | 0.279207 | | Al6d | Al12 | 0.278122 |
| Mn9d | Mn2 | 0.283391 | | Al6d | Al4 | 0.284983 |
| Mn9d | Al7 | 0.285006 | | Al6d | Mn7 | 0.285222 |
| Mn9d | Al6 | 0.289968 | | Al6d | Al8 | 0.286737 |
| | | | | Al6d | Mn9d | 0.289968 |

To overcome the problem of correlations between isomer shift and quadrupole splitting and to take into account the asymmetries in the overall spectral shape the analyses for the crystalline samples above $T_f$ were thus performed with a superposition of two subspectra and (to reduce the number of free parameters) the constraint of equal line widths. (The physical reason for the use of two subspectra should not be confused with the one introduced to fit icosahedral or decagonal quasicrystals.) For a single measurement the fit is certainly not unique, however, gains on reliability if the results exhibit smooth dependence on temperature and Fe content. The ratio of the relative area of the subspectra scatters around 75:25 (figure 6.6) and is in fair agreement with the

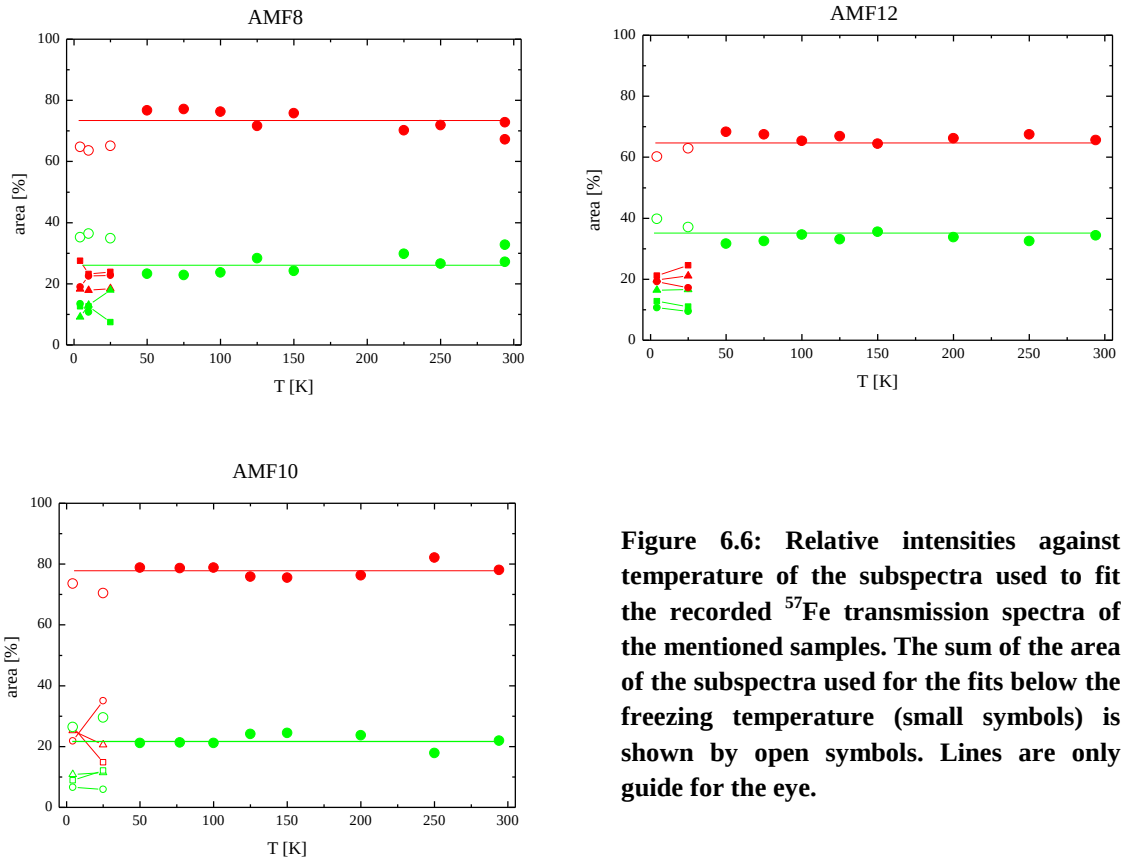


**Figure 6.6: Relative intensities against temperature of the subspectra used to fit the recorded $^{57}$Fe transmission spectra of the mentioned samples. The sum of the area of the subspectra used for the fits below the freezing temperature (small symbols) is shown by open symbols. Lines are only guide for the eye.**

ratio estimated from the above discussed subdivision according to the occupation of the first shell with Al. The line width is only approximately 50% larger than the one

obtained in the α-Fe calibration spectra (figure 6.7). In spite of the constraint of similar line widths for the subspectra, in the fittings the dominant part for this parameter is the spectrum with the large area. Thus this increase reflects that charge density and distribution are not very different on the $^{57}$Fe nucleus embedded in the individual environments which are collected within this subspectrum although the number of Mn atoms in the first neighbor shell differs between two and four (table 6.1). Assuming that assumptions (i) and (ii) are still valid the difference between the (in mean "main" two) environments (Fe on positions which are completely surrounded by Al in the first shell, small spectral area, and Fe on positions with Mn/Al in the neighborhood, large area) in both charge distribution (field gradients given by *QS*, figure 6.7) and charge density (isomer shift given by *CS*, figure 6.8) on the $^{57}$Fe nucleus is resolvable within measuring accuracy. The temperature dependence of the quadrupole splitting was fitted to $QS(T) = QS_0 - bT^{3/2}$ as observed in many non-cubic compounds [29] and in comparable quasicrystalline materials [30] (figure 6.7). The resulting b values are of order of $10^{-6}$ mm/(sK$^{3/2}$). To make contribution of this size reliable it is, however, absolutely necessary to determine the temperature dependence of the lattice spacings because the usual changes in inter atomic distances with temperature may lead to changes in *QS* which are at least comparable.

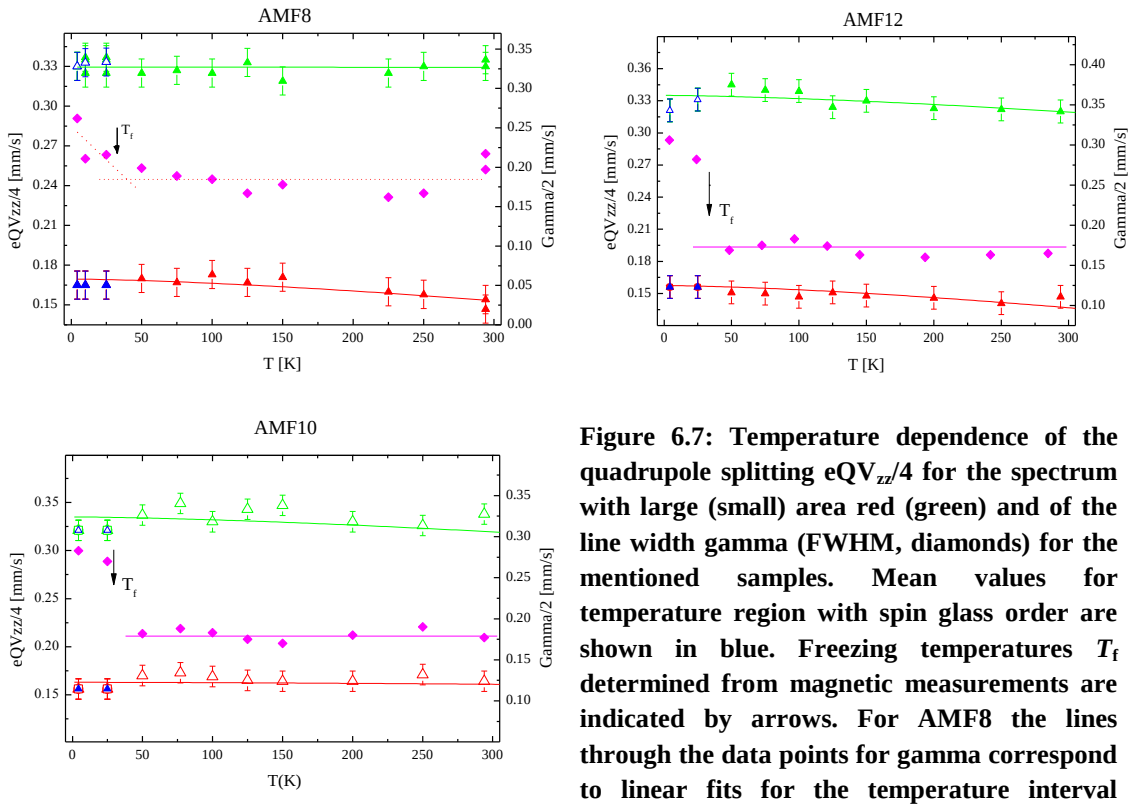


**Figure 6.7: Temperature dependence of the quadrupole splitting $eQV_{zz}/4$ for the spectrum with large (small) area red (green) and of the line width gamma (FWHM, diamonds) for the mentioned samples. Mean values for temperature region with spin glass order are shown in blue. Freezing temperatures $T_f$ determined from magnetic measurements are indicated by arrows. For AMF8 the lines through the data points for gamma correspond to linear fits for the temperature interval below and above $T_f$, respectively. The lines through the data for the quadrupole splitting correspond to fits according to a $T^{3/2}$ dependence.**

For both subspectra both *QS* and CS does not change significantly with Fe content and with structure (figure 6.7, 6.8). This is in line with the results reported in literature. Only slightly smaller value for *QS*, but comparable values for *CS* are obtained for T - $Al_{78}Mn_{15.5}Fe_{6.5}$ [22]. For the icosahedral compounds at room temperature *CS* scatters around 0.22 mm/s (relative to α-Fe) and *QS* values are slightly smaller (around 0.35 mm/s) [11, 23, 31] than the ones found in the present investigations, indicating, as proposed earlier, a higher degree of order for these compounds. Most interesting is, however, the small difference of the weighted mean of these quantities (to get rid of the different fitting procedures) with those evaluated for rhombohedral and decagonal AlCuFe [11,23], decagonal AlNiFe [26], and AlPdFe [25]. Neglecting in first approximation the influence of volume on the isomer shift (proper corrections are at present not possible because lack of lattice spacing data), this points to charge density on the $^{57}$Fe atoms in these compounds mostly determined by Al-(*s*,*p*) and Fe-*d* hybridization and not by the type of transition metal atom in the neighbourhood. This may also explain the small differences in *CS* obtained for the two subspectra representing the main environments, completely and partly surrounded by Al. Because

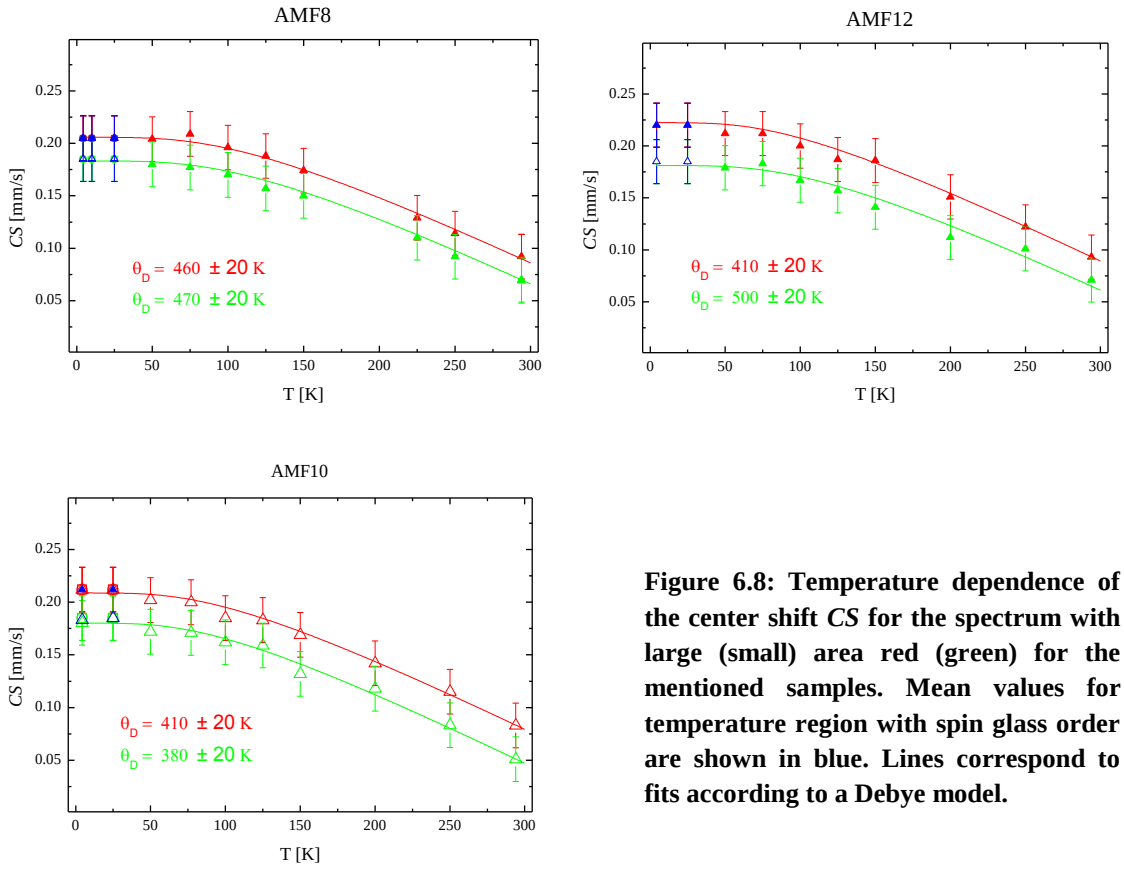


**Figure 6.8: Temperature dependence of the center shift *CS* for the spectrum with large (small) area red (green) for the mentioned samples. Mean values for temperature region with spin glass order are shown in blue. Lines correspond to fits according to a Debye model.**

of the quadrupole distributions used in the analyses of the spectra comparison of mean values are only possible. All arguments concerning the analyses of broadened, structure-less quadrupole split Mössbauer spectra given in literature are certainly applicable, too. To remind, however, again, the advantage of the present analysis was the possibility to start with crystalline compounds and to transform the fitting routine developed for these samples onto the decagonal compound assuming that local surrounding of approximant

and quasicrystal are very similar. Within this analysis one ends up with charge distributions (local field gradients) quite different for the two surroundings. The value of *QS* is larger for Fe completely surrounded by Al. To speculate on differences caused by the local arrangement of neighbour atoms is highly questionable in this complicated structure. Also questionable, but perhaps more reliable, may be the assumption that Al-(*s,p*) and Fe-*d* hybridization dominates the charge distribution and is "less distorted" (in the sense of keeping a high value) for $^{57}$Fe probe atoms completely surrounded by Al (the picture of hybridization needs at least some periodicity). Additional near neighbour transition metal atoms will thus disturb (locally) the hybridization giving rise to smaller asymmetries in the charge distribution around the $^{57}$Fe nucleus.

The Debye temperatures (derived from the temperature dependence of *CS* using the Debye model, see chapter 6.1) are for the two groups of Fe sites within measuring accuracy the same for crystalline AMF8, different for AMF12, and exhibit no clear concentration dependence (figure 6.8). For the decagonal sample the value for $\theta_D$ obtained for the subspectrum with large area is roughly the same as the one of the crystalline samples pointing to a rather similar stiffness for the Fe bonds. The value for the other group (in the present fitting assumption Fe on those Mn sites which are completely surrounded by Al in the first neighbour shell) is, however, smaller compared to the one of the crystalline compounds. $\theta_D$ = 331 K was found for $^{57}$Fe in α-Fe [32]. In rapidly quenched Al-0.02 at% Fe $\theta_D$ = 240 K [33] and from a $^{57}$Co**Al** source experiment $\theta_D$ = 210 K are reported [34]. Thus one would expect that $\theta_D$ varies considerably for the two subspectra. This is not observed in AMF8. The low $\theta_D$ values of Fe doped Al are, however, contrasted by the one obtained for pure Al from elastic constant and velocity of sound data ($\theta_D$ = 462 K [35]). From γ-ray and neutron diffractometry $\theta_D$ = 476 K was estimated for a crystalline $Al_{80.5}Fe_{19.5}$ alloy [33], and for crystalline $Al_6Fe$, and $Al_{13}Fe_4$ $\theta_D$ = 469 K, and 495 K, respectively, are derived from *CS*(T) data [36]. Higher values are reported for I-$Al6_{3.5}Cu_{24}Fe_{12.5}$, $\theta_D$ = 539 K (using standard Mössbauer spectroscopy and fitting with a quadrupole distribution), and I-$Al_{62}Cu_{25.5}Fe_{12.5}$, $\theta_D$ = 580 K (using quasi-elastic Mössbauer spectroscopy by synchrotron radiation). From specific heat and elastic constants values of 536 K and 548 K are derived [37] for $Al_{61.4}Cu_{25.4}Fe_{13.2}$ which is very similar in concentration. In comparison from specific heat measurements $\theta_D$ = 377 K and 343 K were evaluated for annealed and as cast I-$Al_{69}Cu_{20}Fe_{15}$, respectively. Differences of this order of magnitude are known for these two measurement methods. Stadnik and Zhang [24] derived for decagonal $Al_{65}Co_{15}Cu_{19.9}Fe_{0.1}$ $\theta_D$ = 546 K and mentioned the significant differences in reported values for $\theta_D$ in literature. Including the data obtained from specific heat measurements for decagonal $Al_{65}Cu_{20}Co_{15}$ ($\theta_D$ = 596 K [38]) and $Al_{70}Ni_{15}Co_{15}$ ($\theta_D$ = 589 K [39]) lattice stiffness is larger for these constituents (irrespective of the structure) than the one of the presently investigated Al-Mn-Fe.

Below the freezing temperature the recorded spectra exhibit magnetic hyperfine exchange interaction (figure 6.3-6.5). In the analyses each subspectrum from the high-temperature fits is further subdivided into 3 spectra with increased line width to simulate a hyperfine field distribution. A further subdivision does not lead to a better

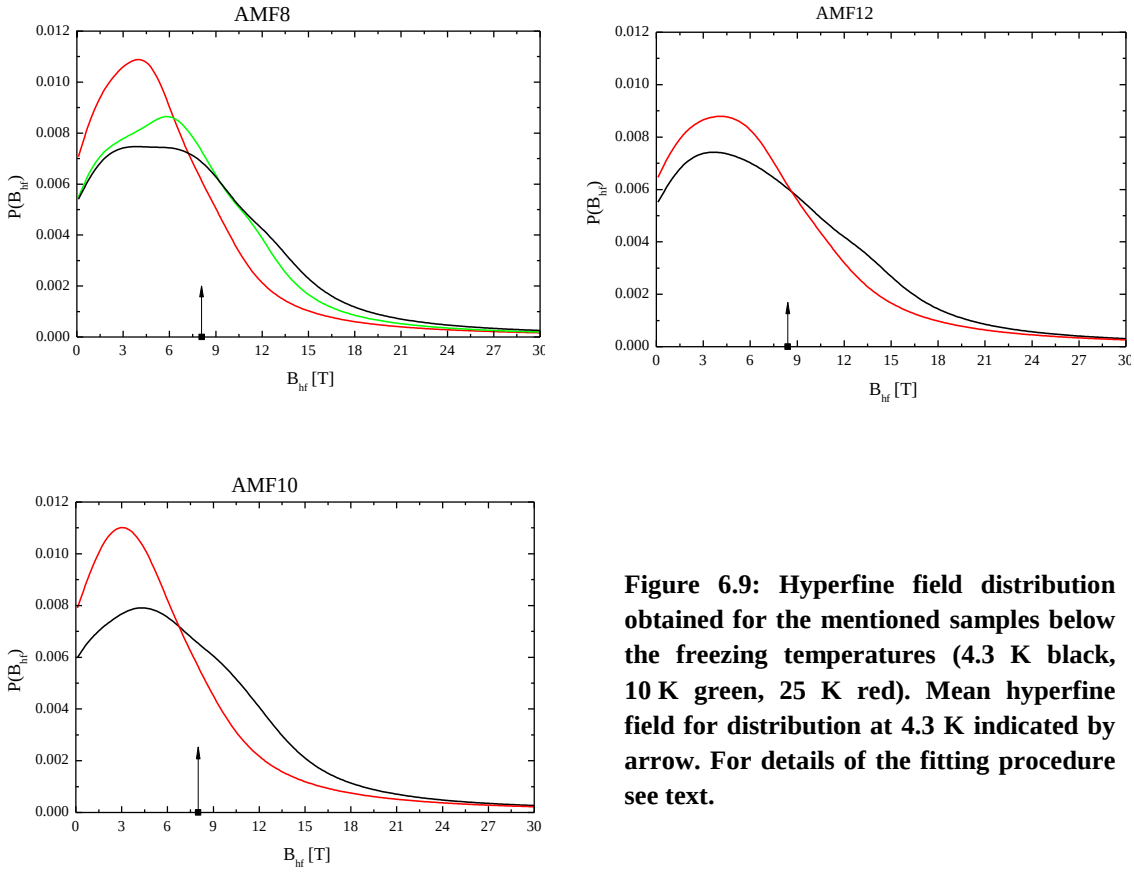


**Figure 6.9: Hyperfine field distribution obtained for the mentioned samples below the freezing temperatures (4.3 K black, 10 K green, 25 K red). Mean hyperfine field for distribution at 4.3 K indicated by arrow. For details of the fitting procedure see text.**

agreement between fitting result and measurement. The sum of the relative area of these 3 subspectra is in fair agreement with the one obtained from the high-temperature fits (figure 6.6). Center shift and quadrupole splitting scatter within each group only within measuring accuracy around the weighted mean (figure 6.7, 6.8). The hyperfine field distribution was derived by folding Lorentzians positioned at the derived discrete hyperfine field values with widths two times the measured FWHM of the respective spectrum (figure 6.9). As usual for spin glasses the width gets broader with decreasing temperature. The mean hyperfine field determined from centre of gravity of the hyperfine field distribution increases with Fe content for the crystalline samples (8.1 T and 8.4 T for AMF8 and AMF12 at 4.3 K, respectively) and amounts 8.0 T at the same temperature for decagonal AMF10. The same trend is observable for $\mu_{eff}$/TM (figure 5.6, chapter 5). The value for AMF10 is also smaller. One has to keep in mind that the Al content for the samples is slightly different (69, 68, and 71 at% for AMF8, AMF12, and AFM10, respectively). The agreement, however, can be seen as a support for both fitting assumptions (i) and (ii). From the present experiments it is not possible to conclude on the value of the Fe moment since the hyperfine field at the nucleus must be seen as the sum of two contributions with (usually) opposite sign, the core and the valence part and only the first one is proportional to the moment. No characteristic changes for both the magnetic and the electrostatic hyperfine interaction for the decagonal sample are present compared to the crystalline ones.

In summary the Mössbauer investigations point to a very small dependence of the derived hyperfine parameters on Fe content in the crystalline samples. It seems that the occupation of the first neighbour shell with the available atom species is dominant and charge density and distribution on the $^{57}Fe$ probe atom are only slightly influenced by changes of the Fe content whereas for the crystalline compounds the mean hyperfine field increases with increasing Fe content. These results support further the similarities between decagonal compound and the approximant $Al_3Mn$.

## 6.4 References


[1] P. Gütlich, R. Link and A. Trautwein 1978 *Mössbauer Spectroscopy and Transition Metal Chemistry* (Springer, New York).

[2] http://www.rsc.org/Membership/Networking/InterestGroups/MossbauerSpect/part2.Asp May (2010).

[3] W. Kündig *Nuclear Instruments and Methods* **48** (1967), 219-228.

[4] S. Mørup and E. Both *Nuclear Instruments and Methods* **124** (1975), 445- 448.

[5] L.Z. Swartzendruber, D. Shechtman, L. Bendersky and J.W. Cahn *Phys. Rev. B* **32** (1985), 1383-1385.

[6] M. Eibschütz, M.E. Lines, H.S. Chen, J.V. Waszczak, G. Papaefthymiou and R.B. Frankel *J. App. Phys.* **63** No. 8 (1988), 4063-4065. M. Eibschütz, M.E. Lines, H.S. Chen, J.V. Waszczak, G. Papaefthymiou and R.B. Frankel *Phys. Rev. Lett.* **59** (1987), 2443-2446.

[7] W.W. Warren. Jr., H.S. Chen and J.J. Hauser *Phys. Rev. B* **32** (1985), 7614-7616.

[8] M. Eibschutz, H.S. Chen and J.J. Hauser *Phys. Rev. Lett.* **56** (1986), 169-172.

[9] G. Le Caer, R.A. Brand and J.M. Dubois *Phil. Mag. Lett.* **56** (1987) 143-151.

[10] R.A. Brand, G. Le Caer and J.M. Dubois *J. Phys. Cond. Matter* **2** (1990), 6413-6431.

[11] R.A. Brand, J. Pelloth and Y. Calvayrac *J. Phys. Cond. Matter* **6** (1994), 11189-11209. R.A. Brand, J. Pelloth, F. Hippert and Y. Calvayrac *J. Phys. Cond. Matter* **11** (1999), 7523-7543.

[12] Z.M. Stadnik, G. Stroink, H. Ma and G. Williams *Phys. Rev. B* **39** (1989), 9797-9805. Z.M. Stadnik and G. Stroink *Phys. Rev. B* **38** (1988), 10447-10453.

[13] J. Teillet and B. Bouchet-Fabre *Hyperfine Interactions* **55** (1990), 1077-1082.

[14] J.Y. Ping, D.G. Rancourt and Z.M. Stadnik *Hyperfine Interactions* **69** (1991), 493-496.

[15] N. Kataoka, A.P. Tsai, A. Inoue, T. Masumoto and Y. Nakamura *Japanese J. App. Phys.* **27** (1988), L1125-L1127.

[16] A. Shastri, F. Borsa, D.R. Torgeson, J.E. Shield and I.A. Gold *Phys. Rev. B* **50** (1994), 15651-15667. Shastri, F. Borsa, D.R. Torgeson, J.E. Shield and I.A. Gold *Phys. Rev. B* **50** (1994), 4224-4227.

[17] C.L. Chien and M. Lu *Phys. Rev. B* **45** (1992), 12793-12796. M. Lu and C.L. Chien *Hyperfine Interactions* **71** (1992), 1525-1530.

[18] S. Nasu, M. Miglierini, K.N. Ishihara and P.H. Shingu *J. Physical Society of Japan* **61** (1992), 3766-3772.

[19] R.A. Dunlap, D.W. Lawther and D.J. Lloyd *Phys. Rev. B* **38** (1988), 3649-3652.

[20] G.J. Long, F. Grandjean, X. Zhang, P.C. Gibbons and K.F. Kelton *J. Non Cryst. Solids* **153-154** (1993), 58-62.

[21] W.W. Warren, H.S. Chen and G.P. Espinosa *Phys. Rev. B* **34** (1986), 4902-4905.

[22] B. Koopmans, P.J. Schurer, Van der Woude and P. Bronsveld *Phys. Rev. B* **35** (1987), 3005-3008.

[23] M. Eibschütz, M.E. Lines, H.S. Chen and F.A. Thiel *Phys. Rev. B* **46** (1992), 491-494.

[24] Z.M. Stadnik and G. Zhang *J. Phys. Cond. Matter* **17** (2005), 6599-6608.
[25] D.W. Lawther and R.A. Dunlap *J. Non Crystalline Solids* **153-154** (1993), 49-52.
[26] R.A. Dunlap *Phys. Mag. B* **67** (1993), 69-75.
[27] J. Hafner and M. Krajci *Phys. Rev. B* **57** (1998), 2849 (12pp).
[28] K. Hiraga, M. Kaneko, Y. Matsuo and S. Hashimoto, *Phil. Mag. B* **67** (1993), 193-205.
[29] E.N. Kaufmann and R.J. Vianden, *Rev. Mod. Phys*. **51** (1979), 161 - 214.
[30] R.A. Brand, J. Voss and Y. Calvayrac *Hyperfine Interactions* **126** (2000), 277-285.
[31] M. Miglierini and S. Nasu *Materials Transactions JIM* **14** (1993), 178-187.
[32] P. Debruner and R.J. Morrison, *Rev. Mod. Phys*. **4** (1964) 63.
[33] H. Ichinose, K. Sassa, Y. Ishida and M. Kato *Phys. Mag. B* **36** Issue 6 (1977), 1367-1374.
[34] S. Sorensen and G. Trumpy *Phys. Rev. B* **7** (1973), 1791-1797.
[35] R.C.G. Killean and E.J. Lisher *J. Phys. C: Solid State Phys.* **8** (1975), 3510-3520. R.C.G. Killean and E.J. Lisher *J. Phys. F: Metal Phys.* **5** (1975), 1170-1112.
[36] S.D. Forder, J.S. Brooks and P.V. Evans *Scripta Materialia* **35** No. 10 (1996), 1167-1173. S.D. Forder, J.S. Brooks, A. Reeder and P.V. Evans *Hyperfine Interactions* **116** (1998), 209-214.
[37] C.A. Swenson, T.A. Lograsso, A.R. Ross and N.E. Anderson *Phys. Rev. B* **66** (2002), 184206 (11pp).
[38] K. Edagawa, M.A. Chernikov, A.D. Bianchi, E. Felder, U. Gubler and H.R. Ott *Phys. Rev. Lett.* **77** (1996), 1071-1074.
[39] A.D. Bianchi, F. Bommeli, E. Felder, M. Kenzelmann, M.A. Chernikov, L. Degiorgi, H.R. Ott and K. Edagawa *Phys. Rev. B* **58** (1998), 3046-3056.

# 7. Summary

Magnetic and Mössbauer investigations were performed on the orthorhombic Taylor phases, T-$Al_3Mn$ (space group *Pnma*) and the decagonal compound $Al_{71}Mn_{19}Fe_{10}$. Parts of the results were already published in [1].

The homogeneity range of Taylor phase in the binary Al-Mn system is enlarged in ternary system Al-Mn-Pd and even more in Al-Mn-Fe. Hiraga *et al*. [2], Pavlyuk *et al*. [3], and Klein *et al*. [4] determined the atomic coordinates. All authors reported (i) very similar values for the positions of the respective sites and (ii) that most of the 156 sites are occupied only by either aluminum or manganese. Exceptions are, according to Hiraga *et al.* four Mn sites, where mixed occupancy is present with some aluminum, and one Al site on which some Mn is embedded. With the exclusion of the last mentioned Al site this is confirmed by Pavlyuk *et al.* only the sites are named different. This holds also for Klein *et al*., but they proposed a different filling and assumed that all of the Pd is embedded on one single Al site. Balanetskyy *et al.* [5] concluded that this assumption is too crude for a correct description of the structure. Performing an atomic count and calculating from this the Mn/Al occupation Hiraga *et al*. ends up in their structural model with $Al_{2.94}Mn$. Adding the Pd content to Mn, Klein *et al*. gets $Al_{2.83}Mn$, (an Al content below the stoichiometric one) whereas Pavlyuk *et al*. obtained $Al_{3.348}Mn$. The Al concentration of this structural model is above the stoichiometric one. We used therefore the structural model proposed by Hiraga *et al.* for the considerations concerning the number of Mössbauer spectra used in the analysis. The 156 atoms are spread over ten layers perpendicular to the *b* direction in the unit cell. Most of the atoms are located at the vertices of small and large pentagons and at the centre of large pentagons. The samples investigated in this thesis are $Al_{75}Mn_{25}$, $Al_{75}Mn_{20}Pd_5$, $Al_{69}Mn_{23}Fe_8$ and $Al_{68}Mn_{20}Fe_{12}$. They are abbreviated as AM, AMP, AMF8 and AMF12 respectively. Preparation and structural investigations were performed by Feuerbacher [6]. For the Fe containing alloys it seems to be reasonable that only the occupation numbers of the sites on which both atomic species are embedded are simultaneously changed (by 0.919 and 0.906 for AMF8 and AMF12, respectively) to take into account the varying Al content and that the occupation of the other sites remains unchanged. The decagonal sample on which we did our measurements was abbreviated as AMF10. Preparation and structural characterization was again done by [6]. The periodicity along the decagonal axis is approximately 1.2 nm according to which quasi periodic puckered layers and planar ones stacked on each other are present. In both the quasicrystalline and the crystalline phase a strong tendency for the formation of pentagonal and decagonal clusters is found. Taking into account the Mössbauer results, it is highly probable that in the decagonal compound too Fe substitutes only Mn.

From dc-magnetic measurements negative Curie-Weiss temperatures $\theta_c$ were obtained for the un-substituted and the Pd containing sample, indicating a predominant antiferromagnetic coupling between Mn atoms carrying a moment. $\theta_c$ increases with increasing Fe content and get positive for AMF12, pointing to a strong contribution of Fe to the magnetic exchange interaction. In agreement with literature for alloys with Al content around 70 at% e.g. [7] we assumed that Pd carry no moment and take this into

account in the calculations of $\mu_{eff}$. In contrast Fe was assumed to carry a moment. As first approximation the content of Mn and Fe was added and a mean $\mu_{eff}$ per transition metal atom was calculated. In agreement with [8] an increase of this moment is observed with increase of Fe. For the decagonal compounds lower $\mu_{eff}$ values compared to the samples with T-phase were obtained.

For all samples irreversibility appear between ZFC and FC measurements below approximately 30 K. Both, the rounding of the peak in the ZFC curves and the shift to lower temperature with increasing field indicate spin glass behaviour. The exponent of ~ 0.1 in the fit of the field dependence of the freezing temperature does neither fit to Ising [9, 10] nor vector spin glasses [10]. In general, $T_f$ decreases with substitution of nonmagnetic Pd, whereas it increases with Fe substitution. The samples showing the Taylor phase have slightly higher $T_f$ values than the compounds forming as decagonal quasicrystals.

The time dependence of the ZFC magnetization exhibits below $T_f$ for all samples within the chosen time interval a logarithmic behaviour allowing the determination of the creep rate *S* which can be normalized to the magnetization at the starting time. A strong temperature dependence and a maximum appearing at approximately $T_f/4$ for 0.5 T and at much lower values for 2.0 T was observed for *S*. Thus the mean effective activation energy *E*, which is related to *S* [11], increases for all external fields with increasing temperature. Since both the barriers which evolve with decreasing temperature should decrease and the time dependence of the magnetization should become stronger with increasing *T*, this result is understandable if *E* is interpreted as the centre of gravity of a broad energy distribution. For a given temperature, part of the relaxations on the low energy side of the distribution function does not contribute to the time dependence of the magnetization, because they are already thermally equilibrated within the experimental time scale. This can be expressed by introducing a cut-off energy which shifts to higher values for higher temperatures, shifting also the centre of gravity to higher energies. Increase of the applied field reduces the effective barrier height, leading to smaller *E* values. An interpretation of the time dependence within the classical droplet model allows an interpretation of *E* in terms of magnetic cluster sizes. In that sense the magnetic entities rotating in the external field are larger in the Fe-substituted than in the Pd- and the un-substituted sample, which is not unexpected as Fe increases magnetic coupling. Despite of the similarity of the structural building blocks of T-phase and decagonal quasicrystal the intrinsic energy landscape is different. The barriers are higher in the T-phase, although the over-all symmetry is lower in the decagonal phase.

One stop protocols for the waiting times at zero external field during cooling were used to gain information on the dynamics below $T_f$. After a second temperature step downwards, rejuvenation is observed, that means after the step the system behaves as if it had been quenched from above $T_f$ without any interrupt. Similar results were obtained for $Al_{73}Mn_{27}$, $Al_{73}Mn_{23}Pd_4$ and D $Al_{73}Mn_{21}Fe_6$ by Dolinsek *et al.* [8], samples prepared under the same conditions but having slightly different Al content. The behavior indicates that non-equilibrium states are passed through by varying the temperature very similar to those reported for conventional spin glasses [12]. The evolution with time of the susceptibility towards equilibrium was investigated in three dimensional Heisenberg spin glasses by Monte Carlo simulations [13]. These calculations show that for the spin

system the dynamical coherence length $l$, which depends strongly on $T$, is in local equilibrium for short distances compared to $l$. The system as whole is, however, not equilibrated. For large waiting times ("old" samples) $l$ increases. This leads to a growth with time of a random (because of the quenched disorder in the spin glass phase) ordering ("aging" of the sample). Assuming that equilibration proceeds by activation over barriers of heights which are a function of $l$ it could be shown in the calculations that the system forgot that it is "old", it seems to be "rejuvenated" by a stepwise cooling from $T_1$ to $T_2$. If the system temperature is changed in a further step back to $T_1$ it behaves as if the step to $T_2$ has not occurred. The system has kept a "memory" of the first aging step. Within the constraint of the present experimental conditions (only dc-magnetization measurements could be performed) it seems that the concept of barrier height dependence on coherence length which by itself strongly depends on temperature and waiting time is able to describe the dynamics observed in the investigated samples.

For the two crystalline samples the $^{57}$Fe Mössbauer spectra recorded above the respective freezing temperature exhibit asymmetries with respect to line intensity and slope which does not allow an analysis with only one quadrupole split spectrum where the different Fe sites are simply taken into account by allowing line broadening. The same holds for the decagonal sample, although the difference in line intensity at 294 K is less pronounced. Investigations on Fe containing decagonal AlMn compounds focus on Al contents around 80 at%. The Mössbauer results are either analyzed by a superposition of two broadened quadrupole split spectra [14, 15, 16] or a quadrupole distribution assuming a linear correlation between quadrupole splitting and isomer shift [17]. Since all analyses are based on structural considerations (decorations of Penrose tiling) of the quasicrystal the attempt was made to start with the structural model of the crystalline compound and to transform the thus found fitting routine onto the quasicrystalline sample. For the crystalline Taylor phase, the distances to the nearest neighbours are calculated for the different sites occupied by Mn. Within a sphere of 0.294 nm, which can be seen as the first neighbor shell, two Mn-atoms have only Al atoms as nearest neighbours. For all other Mn-sites, both Mn and Al are present. It can be assumed that for these two positions, because of the strong Al-*p* Mn-*d* hybridization (see e.g. [18]) the charge density and distribution are different compared to the ones of the other sites for which both atom species are present in the first shell. Assuming (i) that Fe substitutes only Mn and not Al and (ii) that no preferential embedding of Fe on the different lattice sites is present (random distribution) two groups of subspectra with different isomer shift and quadrupole splitting can be expected. According to the occupation numbers given by Hiraga *et al.* [2] a ratio of 0.3:0.7 should be present for the relative intensities of the subspectra representative for these environments. The analyses for the crystalline samples above $T_f$ were thus performed with a superposition of two subspectra and (to reduce the number of free parameters) the constraint of equal line widths. The obtained ratio of the relative area of the subspectra scatters around 0.25:0.75. The line width is only approximately 50% larger than the one obtained in the α-Fe calibration spectra indicating that charge density and distribution are not very different on the $^{57}$Fe nucleus embedded in the individual environments which are collected within a subspectrum. For each subspectrum both *QS* and *CS* does not change significantly with Fe content and with structure. This is in line with the results for

quasicrystalline compounds reported in literature. Most interesting is, however, the small difference of the weighted mean of these quantities (to get rid of the different fitting procedures) with those evaluated for rhombohedral and decagonal AlCuFe [15, 19], and decagonal AlNiFe [20] and AlPdFe [21]. Neglecting in first approximation the influence of volume on the isomer shift, this points to charge density on the $^{57}$Fe nucleus in these compounds mostly determined by Al-(*s*,*p*) and Fe-*d* hybridization and not by the type of transition metal atom in the neighbourhood. This may also explain the small differences in *CS* obtained for the two subspectra representing the main environments, completely and partly surrounded by Al.

The Debye temperatures (derived from the temperature dependence of *CS* using the Debye model) are for the two groups of Fe sites within measuring accuracy the same for crystalline AMF8, different for AMF12, and exhibit no clear concentration dependence. For the decagonal sample the value for $\theta_D$ obtained for the subspectrum with large area is roughly the same as the one of the crystalline samples pointing to a rather similar stiffness for the Fe bonds. The value for the other group (in the present fitting assumption Fe on those Mn sites which are completely surrounded by Al in the first neighbor shell) is, however, smaller compared to the one of the crystalline compounds.

Below the freezing temperature the recorded spectra exhibit magnetic hyperfine exchange interaction. In the analyses each subspectrum from the high-temperature fits is further subdivided into 3 spectra with increased line width to simulate a hyperfine field distribution. The sum of the relative area of these 3 subspectra is in fair agreement with the one obtained from the high-temperature fits. *CS* and *QS* scatter within each group only within measuring accuracy around the weighted mean. The hyperfine field distribution was derived by folding Lorentzians positioned at the derived discrete hyperfine field values with widths two times the measured FWHM of the respective spectrum. As usual for spin glasses the width gets broader with decreasing temperature. The mean hyperfine field determined from centre of gravity of the hyperfine field distribution increases with Fe content for the crystalline samples (8.1 T and 8.4 T for AMF8 and AMF12 at 4.3 K, respectively) and amounts 8.0 T at the same temperature for decagonal AMF10. The same trend is observable for $\mu_{eff}$/TM. The value for AMF10 is also smaller. One has to keep in mind that the Al content for the samples is slightly different (69, 68, and 71 at% for AMF8, AMF12, and AFM10, respectively). The agreement, however, can be seen as a support for both fitting assumptions (i) and (ii). From the present experiments it is not possible to conclude on the value of the Fe moment since the hyperfine field at the nucleus must be seen as the sum of two contributions with (usually) opposite sign, the core and the valence part and only the first one is proportional to the moment.

No characteristic changes for both the magnetic and the electrostatic hyperfine interaction for the decagonal sample are present compared to the crystalline ones. The Mössbauer investigations point to a very small dependence of the derived hyperfine parameters on Fe content in the crystalline samples. It seems that the occupation of the first neighbour shell with the available atom species is dominant for both the decagonal quasicrystal and the crystalline $Al_3$(Mn,Fe) compounds.

## 7.1 References


[1] K. Ali, M. Reissner, M. Feuerbacher and W. Steiner *J. Phys. Conf. Series* **200** (2010), 032002 (4pp). K. Ali, M. Reissner, M. Feuerbacher and W. Steiner *Int. Conf. Application of Mössbauer Effect 2009*, Wien, poster. K. Ali, M. Reissner, M. Feuerbacher and W. Steiner *Int. Conf. Solid Compoundsof Transition Elements 2010*, Annecy, Conference proceedings.

[2] K. Hiraga, M. Kaneko, Y. Matsuo and S. Hashimoto *Phil. Mag. B*, **67** (1993), 193-205.

[3] V.V. Pavlyuk, T.I. Yanson and O.I. Bodak, *Acta Cryst. C* **51** (1995), 792-794.

[4] H. Klein, M. Boudard, M. Audier, M. De Boissieu, H. Vincent, L. Beraha and M. Duneau, *Phil. Mag. Lett.* **75** (1997), 197-208.

[5] S. Balanetskyy, G. Meisterernst, M. Heggen and M. Feuerbacher *Intermetallics* **16** (2008), 71-87.

[6] M. Feuerbacher private communication.

[7] Z.M. Stadnik 1999 *Physical Properties of Quasicrystals* (Springer)

[8] J. Dolinsek, J. Slanovec, Z. Jaglicic, M. Heggen, S. Balanetskyy, M. Feuerbacher and K. Urban *Phys. Rev. B* **77** (2008), 064430 (18pp)

[9] J.R.L. de Almeida and D.J. Thouless, *J. Phys. A: Math. Gen.* **11** (1978), 983-990

[10] K.H. Fisher and J.A. Hertz, 1986 *Spin Glasses* (Cambridge: Cambridge University Press)

[11] J. Souletie, *J. Physique* **41** (1983), 1095-1116

[12] R. Mathieu, P. Jönsson, D.N.H. Nam and P. Nordblad *Phys Rev. B* **63** (2001), 092401 (4pp). R. Mathieu, M. Hudl, and P. Nordblad *Journal of Physics: Conference Series* **200** (2010), 032042 (4pp).

[13] L. Berthier and A.P. Young *Phys. Rev. B* **71** (2005), 214429 (14pp). L. Berthier and A.P. Young *Phys. Rev. B* **69** (2004), 184423 (14pp).

[14] B. Koopmans, P.J. Schurer, Van der Woude and P. Bronsveld *Phys. Rev. B* **35** (1987), 3005-3008.

[15] M. Eibschütz, M.E. Lines, H.S. Chen and F.A. Thiel *Phys. Rev. B* **46** (1992), 491-494

[16] M. Stadnik and G. Zhang *J. Phys. Cond. Matter* **17** (2005), 6599-6608.

[17] R.A. Brand, G.Le Caer and J.M. Dubois *J. Phys. Cond. Matter* **2** (1990), 6413-6431.

[18] Hafner J, Krajci M Phys. Rev. B **57** (1998), 2849 (12pp)

[19] R.A. Brand, J. Pelloth and Y. Calvayrac *J. Phys. Cond. Matter* **6** (1994), 11189-11209. R.A. Brand, J. Pelloth, F. Hippert and Y. Calvayrac *J. Phys. Cond. Matter* **11** (1999), 7523-7543.

[20] R.A. Dunlap *Phys. Mag. B* **67** (1993), 69-75.

[21] D.W. Lawther and R.A. Dunlap *J. Non Crystalline Solids* **153-154** (1993), 49-52.